THE DESIGN AND DEFORMATION MECHANISM OF DEFECT-BASED MICROSTRUCTURE WITHIN MAGNESIUM

by

Yushun Liu

A thesis submitted to the Faculty of Graduate Studies of the

The University of Manitoba

in partial fulfillment of the requirements of the degree of

Doctor of Philosophy

Department of Mechanical Engineering

University of Manitoba

Winnipeg, Manitoba, Canada

Abstract

As the lightest structural metal, Magnesium (Mg) has been considered a promising candidate for automobiles and aerospace applications, however, its high mechanical anisotropy and poor ductility severely limit its wide applications. This thesis targets exploiting novel defect structures, i.e., grain boundaries and dislocations, and their deformation mechanisms, using transmission electron microscopy (TEM) and in-situ techniques, to advance the mechanical properties of Mg.

Aiming at developing effective preparation of nano-crystalline samples containing excessive grain boundaries for TEM characterization, a wedge mechanical polishing approach was adopted and successfully produced nano-crystalline with a size of ~100nm. This synthesizing approach can be applied to other Mg alloys and other metals as a simple and fast nano-crystalline preparation.

To further explore deformation mechanisms that require tracking grains re-orientation in real-time, new in-situ setting, integrating nano-indentation tests with hollow-cone dark-field (HCDF) imaging, has been proposed and successfully obtained the rotation of grains/slip planes in real-time, together with morphological observation. Results show that significant grain rotation along with dislocation activity occurs during the indentation, and a possible cooperative deformation mode between them has been experimentally demonstrated for the first time.

Apart from grain boundaries, a novel dislocation structure consisting of periodically spaced <c>-screw dislocations was investigated using pure Mg as the model system to demonstrate its availability in different alloy systems. Results show that simple hot-compression has successfully introduced desired dislocation structures. Its formation mechanism and potential deformation mechanisms were discussed based on dislocation interactions.

To summarize, this thesis explores the possibility of optimizing defect structures to improve the mechanical performance of Mg and its alloys. Our findings provide new insights into synthesizing methods, characterization techniques, and understanding the deformation mechanisms of Mg.

Dedication

To my family for their endless love and support.

Acknowledgment

I would like to address my deepest gratitude to the many who have helped me during the four years of my Ph.D. study, I could not have accomplished this thesis without their help.

Foremost, I want to give my sincere gratitude to my advisor, professor Guo-zhen Zhu, for her helpful support and patient guidance. Under Dr. Zhu's supervision, I've learned a lot from technical details like TEM operation, image simulation to the principle of effective experimental designing, etc. Apart from being a knowledgeable professor who guides me through my Ph.D. project, Dr. Zhu is also a warm-hearted friend who has always been kind in supporting me, offering help whenever possible, giving chances for group activity, and making our group feel like home to me. I truly appreciate all the guidance and help Dr. Zhu has offered.

I would like to give thank specifically to my committee members, Dr. Derek Oliver and Dr. Chuang Deng, for giving me valuable guidance and suggestions on my research project.

My appreciation also goes to my group members and friends, Moein Imani Foumani, Zhina Razaghi, Forough Abbasi Shahir, Farhang Parsa, Syed Taha Khursheed, Minghui Ling, Dr. Wangwang Kuang, Dr. Ping zhou, Lulu Guo, Xinyuan Song, etc. for their kind help and support. I'm also thankful to Dr. Jian Wang and Dr. Dongyue Xie from the University of Nebraska-Lincoln for their help in data analysis and the enlightening discussions with them.

A large portion of my Ph.D. time was spent at Manitoba Institutes for Materials (MIM) where most microscopes I used are hosted. Thus I would also like to express my gratitude to Dr. Abdul Khan, Dr. Ravinder Sidhu, and Jolly Hipolito who work as technicians in MIM. Whenever I encountered some technical difficulty or needed any experimental advice, they were always enthusiastic in helping me solve the problems.

Finally, thank my mother Jizhen Yang without whom none of this would be possible, and all my family members for their never-ending love and support. It is your love that keeps me going.

Contents

Contents

Contents

List of Figures:

List of Figures

Nomenclature

Mg	Magnesium
Al	Aluminum
Y	Yttrium
Er	Erbium
Zn	Zinc
Cu	Copper
Mn	Manganese
HCDF	Hollow-cone dark-field
BF	Bright-field
DF	Dark-field
TEM	Transmission electron microscopy
SEM	Scanning electron microscopy
EBSD	Electron backscatter diffraction
TKD	Transmission Kikuchi diffraction
EDS	Energy dispersive spectrum
HRTEM	High-resolution transmission electron microscopy
GBs	Grain boundaries
TBs	Twin boundaries
RE	Rare-earth

UTS	Ultimate tensile strength
HCP	Hexagonal close-packed
CRSS	Critical resolved shear stress
MD	Molecular dynamics
SPD	Severe plastic deformation
HPT	High-pressure torsion
ECAP	Equal channel angular pressing
SNC	Surface nano-crystallization
LEDS	Low-energy dislocation structure
IPF	Inversed pole figure
DRX	Dynamic recrystallization
SMAT	Surface mechanical attrition treatment
LSP	Laser shot peening
USSP	Ultra-sonic shot peening
SMRT	Surface mechanical rolling treatment
CBED	Convergent beam electron diffraction
ASBs	Adiabatic shear bands
SAED	Selected-area electron diffraction
FFT	Fast Fourier transformed
IFFT	Inverse fast Fourier transformed

Nomenclature

DTTF	Discrete fast Fourier transformation
STEM	Scanning transmission electron microscopy
HAADF	High angle annular dark-field
FIB	Focused ion beam

Chapter 1 Introduction

1.1 Background and Motivations

The ever-demanding problem of global warming and skyrocketing oil prices keeps pushing the search for alternative environmental-friendly structural materials, using lightweight materials is considered a key solution to this problem. First isolated by Humphry Davy in 1808, magnesium is the lighted among all structural metallic materials. With a density of 1.74 g/cm^3, one quarter that of steel (7.85 g/cm^3) and two third that of aluminum (Al) (2.7 g/cm^3), combined with adequate strength and good castability, it is no wonder that magnesium and its alloys have been attracting increasing interests in many weight-sensitive industries like automobile and aerospace [1-4] as a candidate for substituting conventional structural materials like steel and aluminum. For example, a review article conducted by Kulekci [5] points out that 22-70% weight reduction can be achieved for automobiles by substituting with components made of Mg alloys. And weight reduction of 22.5 kilograms renders approximately a 1% increase in fuel efficiency [6]. Not only promising, weight reduction is also a feasible approach, as stated by studies of the Massachusetts Institute of Technology: modern automobiles can still achieve 35% weight reduction at a reasonable cost, leading to 10%~20% less fuel consumption [7]. Thus it is not hard to conceive by replacing components previously made of steel or aluminum with magnesium, there is a great opportunity for reducing fuel consumption dramatically thus alleviating the long-standing issue of global warming.

The long-standing issue that limits the wide applications of magnesium is its comparatively low strength and more importantly, poor ductility. Such poor mechanical properties roots in anisotropic responses inheriting in their hexagonal close-packed (HCP) lattice. In detail, basal slips are the main deformation carriers at room temperature but only contribute to deformation parallel to the basal plane. The non-basal slips, including prismatic and pyramidal slips, offer additional

deformation modes needed for homogeneous deformation and more importantly can accommodate plastic deformation vertical to the basal plane. However, their much higher friction force (two orders of magnitude greater compared to the ones for basal slips at room temperature) leads to limited activation during room temperature deformation. As a result, twinning is commonly activated in Mg to help accommodate plastic deformation, resulting in a strong basal texture and worse formability. The current emphasis for advancing magnesium is to improve its deformability while increasing strength through tuning the relative activities of basal slip, non-basal slip, and twinning.

In hope of developing high-performance magnesium alloys promising of substituting conventional structural materials and in the process addressing the energy problems, the main motivation of this research is to study efficient yet cost-effective ways that can simultaneously improve both strength and ductility of Mg alloys.

1.2 Objectives

The current study targets the design of new high-performance Mg at a reasonable cost. Alloying (particularly with rare-earth (RE) elements) shows promise in improving both strength and ductility, however, the addition of expensive RE elements needs to be avoided or at least minimized to be cost-effective. Without changing their chemical compositions, defect engineering is capable of further improving both strength and ductility and therefore becomes the focus of current research. Advancing Mg alloys through both engineering their grain boundaries (nano-crystalline materials) and dislocations (a novel dislocation structure) have been explored. The objectives are summarized as follows:

1. To design and manufacture nano-crystalline Mg using mechanical processing;

2. To overcome the current experimental limitation and investigate the deformation mechanisms of nano-crystalline Mg;

3. To tailor and produce a novel strengthening dislocation structure using pure Mg as the model system.

1.3 Organization of the thesis

In this thesis, we explore the possibility of tuning grain boundaries and dislocations in Mg, in hope of optimizing the microstructure needed in the fabrication of high-performance Mg alloy at a reasonable cost. Detailed characterization has been carried out to study both the origin of the produced nano- and micro-structures, as well as possible impact on the mechanical performance, providing a new understanding of the further structural optimization of Mg via defect-engineering.

A brief literature review is presented in Chapter 2.

Detailed experimental designs, particularly a new experimental setting for in-situ nano-indentation, for the current study are elaborated in Chapter 3.

In Chapter 4, we report the formation of nano-crystalline Mg via a routinely processing approach: mechanical polishing. We carefully tuned the polishing parameters and therefore controlled the structure of Mg samples. Our approach offers a fast, easy yet cost-effective way to prepare nano-crystalline TEM samples out of coarse-grained alloys with a good success rate. Results show that this technique applies to a wide range of Mg alloys and other metals.

With the invention of quick sample preparation described in Chapter 4, we further explored the deformation mechanism of nano-crystalline Mg using in-situ TEM nano-indentation in Chapter 5. Targeting the characterization difficulties of providing only either morphological or crystallographic information during deformation, HCDF was for the first time used to track the re-orientation of grain/slip planes in nano-crystalline in real-time, so that a combination of morphological and crystallographic information can be obtained at the same time. Based on the experimental results, we were able to provide the first experimental evidence of cooperative deformation modes between grain rotation and dislocation activities.

In Chapter 6, we switch to another defect commonly used for strengthening, namely, dislocations. A novel dislocation structure comprised of <c>-screw dislocation arrays was studied. Uniaxial hot-compression in pure Mg successfully introduced such dislocation structure which had only been reported in Mg alloys, proving its independence from the presence of alloy elements. Possible formation mechanisms and potential strengthening of such dislocation structures have also been discussed.

Finally, in Chapter 7, we summarize the key results and findings of this thesis. Possible future works have also been envisioned for both nano-crystalline and the dislocation structure found in the current study.

Chapter 2 Literature Review

Apart from those widely used commercialized Mg alloy systems alloyed with zinc (Zn), aluminum (Al), and manganese (Mn), etc. [8], the addition of RE elements like gadolinium (Gd), Yttrium (Y), and Erbium (Er), have led to the discovery of new high-performance alloy systems [9, 10]. However, even though increasing RE alloying concentration has proven effective to manufacture Mg alloys with high strength, the extremely high price of RE elements makes the mass production of alloys with high RE concentration practically impossible. Fortunately, there is an alternative strengthening approach that does not require altering the chemical composition of materials. Such an approach, which is defined as defect-engineering, exploits the fact that the strength of crystalline materials increases by altering crystallographic defects like point defects (vacancy, interstitial), line defects (dislocations), and planar defects (grain boundaries (GBs), twin boundaries (TBs)). Such strengthening occurs because these defects can serve as inhibitors to the movement of dislocations which is the major plastic deformation carrier during the deformation of crystalline materials, making the deformation process harder. Unlike alloying, defect-engineering does not require adding external composition, providing an effective yet flexible way to tune the properties of materials. This chapter will discuss the deformation modes of Mg and their current challenges, followed by the discussion of how defects change mechanical properties. After that, a discussion of how to synthesize target defects is included.

2.1 Deformation Modes of Mg and Current Challenges

Although showing great potential, Mg and its alloys are suffering from several problems which heavily hinder their wider industrial applications. The limited strength of pure Mg (~90 MPa ultimate tensile strength (UTS) [8]) makes substituting conventional structural materials with Mg virtually impossible in many cases. Even with alloying, commercial Mg alloys like AZ31, AZ61, and AZ91 widely used in industrials only possess UTS ~120 MPa, which can be even lower if subjected to a corrosive environment [11]. In sharp contrast, Al alloys, which are also accepted as

a lightweight substitute for steel, can achieve UTS over 500 MPa [12], comparable to some low-carbon steel [13]. Thus in many applications, using Mg alloys as an alternative to achieve weight reduction is not accepted, simply due to insufficient strength. Another problem haunting Mg and its alloy is their high mechanical anisotropy, resulting in texture and crack formation during deformation, leading to premature failure and low ductility compared to steel and aluminum. As a result, the formability of Mg is poor at room temperature, pure Mg tends to fracture around 10% single-pass thickness reduction during cold rolling, while pure Al can easily achieve 90% reduction without problems [14].

To further broaden the application of Mg and its alloys, it is of essence to improve their rather low strength and ductility. The main origin of such poor mechanical performance of Mg and its alloy lies within its crystal structure, different from conventional structural materials like steel and Al which have cubic crystal structure, the HCP crystal structure (c/a ratio ~1.623) of Mg has lower symmetry, making mechanical responses along different directions significantly different (mechanical anisotropy). Four main slip modes exist in Mg as shown in Figure 2.1 (a): basal <a>, non-basal (prismatic) <a> and two types of pyramidal <c+a> slip [15]. Under room temperature deformation, the basal <a> slip operating on the (0001) basal plane is the easiest and dominating slip system, with a critical resolved shear stress (CRSS) of only ~0.5 MPa [16]. Although <a> slip can operate on non-basal prismatic $\{10\bar{1}0\}$ planes, its much higher CRSS (~45-60 MPa) value [17] makes it less active under room temperature deformation. Consequently, the dominating easy-gliding basal <a> slip makes the deformation of Mg and its alloy along basal planes very easy, causing their relatively low strength and strong mechanical anisotropy. Additionally, basal <a> slip alone can only provide three independent slip systems which are insufficient for homogeneous deformation of polycrystalline materials according to the well-known von Mises–Taylor criterion, which states at least five independent slip systems are required. Thus extra deformation modes like twinning have to be introduced, two types of twinning ($\{10\bar{1}2\}<10\bar{1}1>$ tension twinning and

{10$\bar{1}$1}<10$\bar{1}$2> compression twinning) exist in Mg [15] as shown in Figure 2.1 (b), and are commonly found in Mg and its alloys deformed at room or lower temperature. Twinning not only fills in the lack of independent slip systems, it also accommodates deformation along the <c> axis which is not possible for basal slip. It is worth mentioning that the type of twinning being activated during deformation is highly dependent on the type of stress applied along the <c>-axis, naturally, a preferable twinning mode is expected to take place dominantly during loading, potentially leading to strong mechanical anisotropy [18].

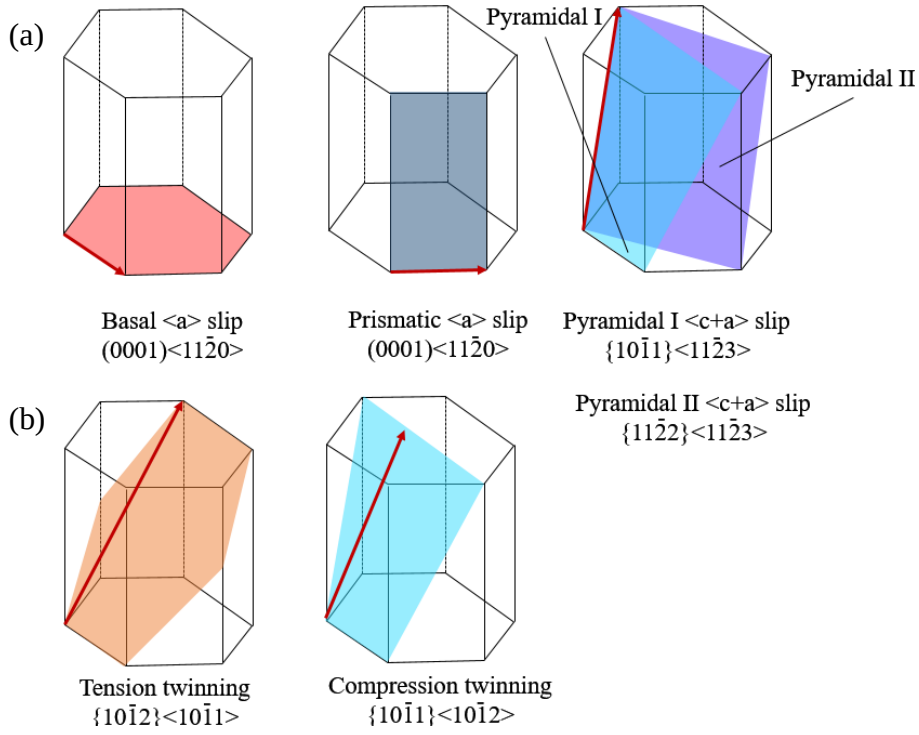

Figure 2.1 Major deformation modes for Mg. (a) four slip systems in Mg and (b) two twinning systems.

Pyramidal <c+a> slip can also be activated under certain conditions, like under elevated temperature, adding alloying elements or refined grain size, etc. [19-21] Similar to twinning, pyramidal <c+a> slips can provide extra slip systems and accommodate strain along <c> axis, thus significantly improving the plasticity of Mg. In fact, the activation of pyramidal <c+a> dislocation is considered one key factor controlling the ductility of Mg and its alloys [21-25]. It is found that the CRSS of <c+a> dislocations is roughly 100 times that of basal <a> slip in pure Mg [20]. Not

only hard to initiate under room temperature, molecular dynamics (MD) simulation has also suggested a basal-dissociation process of <c+a> dislocations which renders them completely immobile [26], such dissociation has been experimentally demonstrated in many Mg alloys with RE additions [27, 28]. The extremely high CRSS and immobile basal-dissociation transition of pyramidal <c+a> dislocations together have severely limited the number of available independent slip systems for Mg deformed under room temperature, resulting in its poor ductility.

2.2 Solutions to the Problems

2.2.1 Alloying

To address these long-standing issues, numerous past studies have been conducted trying to improve the mechanical performance of Mg alloys. The most commonly used and often effective method is perhaps alloying, Al and Zn, both of which are rather inexpensive and highly soluble in Mg, were first considered the preferable alloying elements for Mg. Early researchers in the 20th century have successfully developed several commercial Mg alloy systems, like Mg-Al-Zn based AZ series and Mg-Al-Mn based AM series [8]. These alloys possess a good combination of decent strength (e.g. ~160 MPa for casted AZ91D [8]), ductility (~ 15% elongation for many casting alloys [8]), cost-efficiency, and good castability, thus are widely used in real-life applications. However, their relatively low strength compared to conventional structural materials and poor mechanical performance at elevated temperatures [29] fails to meet the increasing demand for high-performance Mg alloys, leading to the development of new alloy systems, among which the Mg-RE alloy systems show the most promise. For instance, significant enhancement of creep resistance of Mg at 550K is obtained by Y alloying [9], and the introduction of Er is reported to increase the UTS of alloy to 285 MPa while still retaining a good elongation as high as 16% [10]. The outstanding strengthening effects of RE elements are generally attributed to solution-hardening, grain refining strengthening, precipitation hardening, and dispersion strengthening [30], while the

enhanced ductility is believed to be associated with texture modification whose underlying mechanism remains still debatable, despite numerous studies devoted to this topic [31].

Although the efficiency of RE elements in improving alloy performance has been undoubtedly demonstrated by many past researches, certain problems with RE alloying gradually emerge as the pursuit for higher performance Mg alloys goes on. Compromised ductility, for the starter, has been frequently reported in Mg-RE alloys with a high concentration of RE elements [32-35]. These alloys generally possess very high strength, some can reach UTS as high as over 500 MPa, comparable to some Al counterparts, but at the price of very limited elongation of below 10%, in some extreme cases of only around 2% [35, 36]. Other problems are more economical, simply because RE elements are too expensive to be added in large amounts if one is aimed at real-life industrial manufacturing. The extremely poor recyclability of RE elements also takes its toll on the already poor cost-efficiency of Mg-RE alloys. As can be in Figure 2.2, in sharp comparison to conventional alloying elements like Al, Cu, and Fe with fairly high recycling rates of over 50%, most RE elements used in Mg-RE alloys have negligible recycling rates below 1%, making the alloying even more expensive [37]. In fact, with the addition of only 1 wt.% RE elements, the cost for high-temperature Ni-based superalloys can almost double [38]. More importantly, strengthening alloys by RE elements is gradually reaching its limit as researchers keep adding more of them into the system. Naturally, it is only reasonable to seek alternative or collective ways to better improve alloy performance.

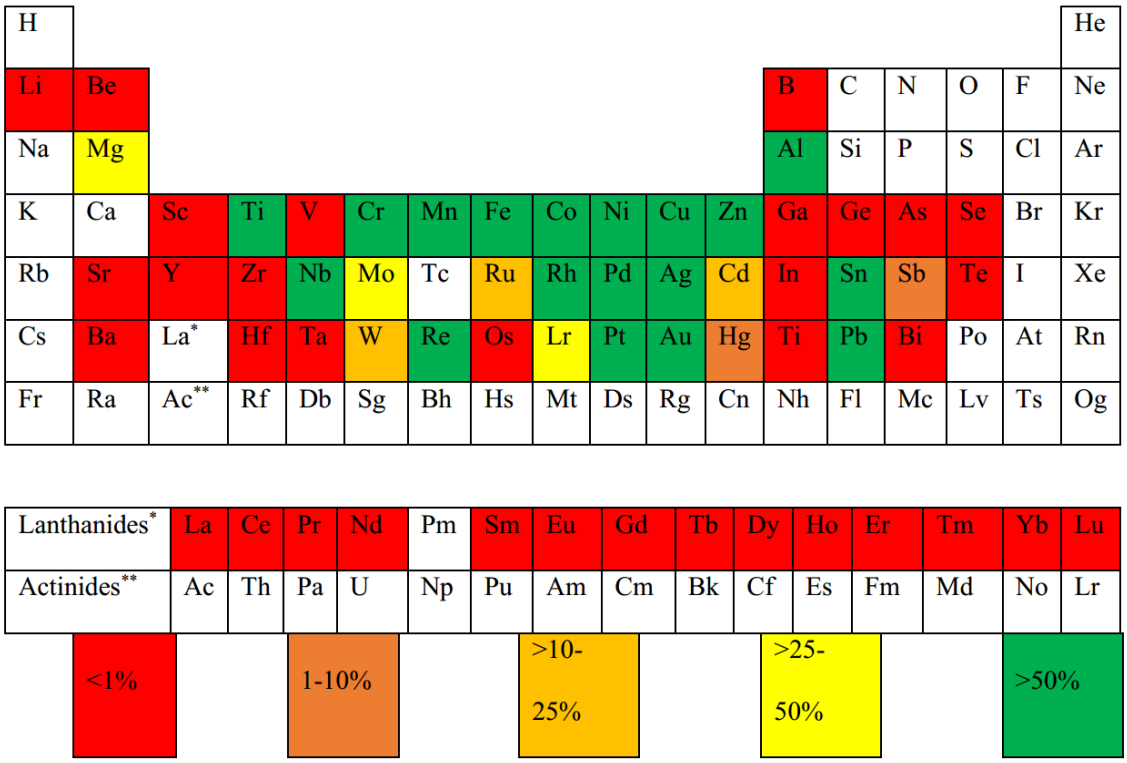

Figure 2.2 Periodical table color-coded based on global estimates of end-of-life recycling rates. Unshaded elements indicate lack of data, adopted from ref. [37].

2.2.2 Defect Engineering

Defect strengthening has been considered one promising alternative strengthening method to alloying. The essential idea of defect strengthening actually has been around for a long time, probably dating back to the very beginning of using metallic tools, when people found metals became harder after being repeatedly hit. But trying to precisely control these defects to our advantage (or say "defect engineering") has just become more interested in the past decades. Thanks to the advancement of characterization techniques like atom-resolved electron microscope [39] and simulation methods as a result of ever more simulation power owing to the constant rapid evolution of the semiconductor industry [40], the once invisible underlying deformation processes are now becoming increasingly accessible to researchers down to even atomic scales via both experiments and simulations, enabling fine control over these defects to achieve such "engineering".

Two major defect strengthening mediums, grain boundaries as a typical planer defect and dislocations as a typical line defect, are mostly used and thus chosen in this study.

2.2.2.1 Strengthening through planar defects (Grain boundaries or Twin boundaries)

Planar defects like GBs and TBs, which are commonly found in most metallic materials, can serve as effective strengtheners by acting as walls hindering the movement of dislocations. Such strengthening effect can be described empirically by the well-known Hall-Petch equation shown in Equation 2.1 [41, 42], predicting increased strength with decreased grain sizes.

$$\sigma_y = \sigma_0 + k_y d^{-0.5}$$

Equation 2.1 Hall-Petch equation, where σ_y is the yield stress, σ_0 is a material constant for starting stress for dislocation movement, k_y is the strengthening coefficient, and d is the grain size

Apart from GBs, coherent TBs can also act as strengtheners. Although it is worth mentioning that the strengthening of TBs follows the same equations but usually has a higher *k* value (stronger strengthening effect) [43]. Many research have been done and succeeded in strengthening using TBs [44-47], for example, nano-twinned Ni-based alloys with exceptional cryogenic mechanical properties were synthesized by Ding et al. [48] and extremely strong nano-twinned copper (Cu) with UTS over 1000 MPa was synthesized by Lu et al. using pulsed electrodeposition [47]. Though the deposition nature of such process makes the fabrication of large bulk components less efficient, this method is usually only used for fabricating films, coating, and nanostructures [49-51].

Similar to work-hardening, reducing grain size not only benefits from improved strength, it can also change the ductility of materials simultaneously. Two reasons are believed to cause the improved ductility of fine-grained Mg. Firstly, the activity of more non-basal slip systems (non-basal <a> and/or pyramidal <c+a> dislocations) becomes enhanced as the grain size goes down, providing the ability to accommodate strain along the <c> axis and extra slip systems needed for the homogeneous deformation, resulting in much more homogenous deformation without cracking [52, 53]. Secondly, as mentioned earlier, <c+a> dislocations tend to dissociate into immobile

configuration under room temperature deformation, however, such undesirable transition can be suppressed in fine-grained materials, as <c+a> dislocation would have a higher chance of traveling through the whole grain before the dissociation process happens, thus actively contributing to the plastic deformation [26].

The deformation mechanism of nano-crystalline materials has been attracting researchers' attention due to their distinct mechanical properties (e.g. extremely high strength) compared to their coarse-grained counterparts [47]. However, once the grain size goes beyond a certain threshold, usually ~10nm depending on the specific materials, it has been found that further reduction of the grain size abnormally leads to the softening of materials [47, 54-56]. The transition from dislocation-dominated deformation in coarse grains bigger than 1μm to GBs-related deformation in nano-crystalline (e.g., grain boundary sliding, grain boundary migration, and grain rotation, etc.) is believed to be responsible for the observed softening.

2.2.2.2 Strengthening through line defects (dislocations)

Dislocations, being the major plastic deformation carriers, can also act as effective strengtheners by dislocation tangling and multiplication, creating obstacles to hinder/trap the following dislocations, such process is generally called work hardening [57], and it plays important role in the manufacturing of many metallic materials. Apart from strengthening, the work hardening capacity is also believed positively related to alloys' ductility [58-60]. According to the Considére criterion for necking as presented in Equation 2.2, tensile plastic instability (necking) takes place when there is an insufficient work hardening rate, resulting in premature failure and limited ductility of materials [61, 62]. It is also worth mentioning that lack of work hardening capacity is also believed to be one possible culprit responsible for the extremely limited ductility found in many nano-crystalline materials [63, 64]. Research on gradient materials conducted by Fang et al. [64] also shows that it is possible to address the ductility problem of nano-crystalline by introducing more work hardening capacity. Thus enhancing the interactions between dislocations, namely enhancing

the work hardening capacity, can be an effective way to simultaneously improve both the strength and ductility of Mg alloys.

$$(\frac{\partial\sigma}{\partial\varepsilon})\leq\sigma$$

Equation 2.2 Considére criterion for necking [63].

Though thoroughly studied in cubic materials [57], the work hardening of Mg is much less well understood due to its HCP crystal structure and consequently much more complicated deformation modes. So far, only a few studies exist for the work hardening of Mg alloys, most of them focus on indirect factors like texture, grain size, and alloy elements, etc. that might affect work hardening. However, studies on dislocation structure itself in Mg, which is directly responsible for the work hardening behaviors, still remain rather uncharted. Theoretical calculations predict the effects of dislocation on work hardening vary with its type and specific configurations [65, 66], which is supported by different work hardening stages observed in cubic materials subjected to the fatigue process [67-71]. The early stage hardening in fatigued cubic materials is characterized by low energy dislocation structures (LEDS) like tilt wall, dislocation dipole, 'Taylor lattice' which is originally proposed by Taylor [72] and later revised by Neumann [69], featuring periodically arranged arrays of straight edge dislocations with opposite signs as shown in Figure 2.3. Unlike the high work hardening rate caused by dislocation forest in stage II, the work hardening rate from these LEDS in stage differs due to the "screening" effect between opposite-signed dislocations in LEDS like the "Taylor" lattice [73]. Such properties make these LEDS potentially useful in terms of tuning the work hardening behavior of materials. Unfortunately, even though some theoretical calculations suggest that such LEDS should be more favorable in hexagonal materials where planar slips dominate [73], the experimental evidence of such LEDS in Mg remains largely sparse.

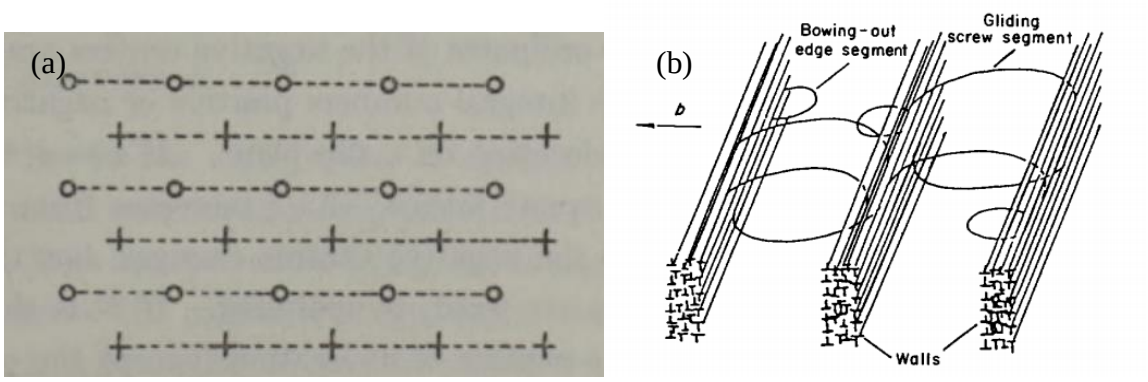

Figure 2.3 Illustration of Taylor lattice. (a) Original model proposed by Taylor [72]; and (b) revised model based on experimental results in fatigued cubic materials [69].

In addition to its configuration, the type of dislocations involved during interactions also plays an important role in strengthening the materials. For instance, the strengthening effect of basal-basal interaction is far weaker compared to that of basal-prismatic or that of basal-pyramidal. Thus both configuration and type of dislocations should be taken into consideration if one is to engineer dislocations to yield maximized strengthening [65].

It is worth mentioning that the formation of the "Taylor" lattice usually requires prevailing planar slip that usually involves cyclic loading [73, 74], making the manufacturing of such dislocation structure inconvenient. And unfortunately, the existence of 'Taylor' lattice is rarely reported in hexagonal materials like Mg. Recently, a novel LEDS, similar to the "Taylor" lattice, in the form of <c>-screw dislocation arrays decorated with Gd has been reported in Mg-Gd binary alloys, and is promising to serve as an effective strengthener, but a detailed study is still needed for a better understanding of such novel dislocation structures [75].

2.3 Manipulation of Grain Boundaries

How to modify the properties of metals has always been a key interest to metallurgists and materials scientists, apart from alloying, grain refining (introducing more GBs) is another commonly used strengthening strategy. Guided by the Hall-Petch equation [41, 42], the strength of nano-crystalline materials can be one order of magnitude higher compared to their coarse-grained counterparts [76], as a result of high density of GBs. Since the pioneering review article by Glieter [76] on 1989,

increasing interests have been drawn to nano-crystalline materials in the past decades [77], and significant progress has been made trying to solve issues associated with nano-crystalline materials. For example, the interfaces in nano-crystalline materials are usually under a high energy state, making the materials very unstable against heating and tend to coarsen easily. Thus how to stabilize these interfaces, which essentially give the materials their supreme mechanical properties, is one of the most important issues that need to be addressed for nano-crystalline materials. To solve this problem, different kinds of low-energy interfaces have been studied and yielded improved stability, including TBs, low-angle GBs, and interphase boundaries [77].

The biggest attraction of nano-crystalline materials is probably their extremely high strength, which can be ~5 times that of their coarse-grained counterparts [47]. The strength-ductility tread-off holds for most strengthening approaches, however, grain refining is capable of avoiding such trade-off. For example, superplasticity has been reported in various materials with reduced grain sizes when deformed at a relatively low strain rate [78]. The underlying mechanism for such superior plasticity is attributed to extensive activation of grain-boundaries accommodated deformation processes like grain boundary sliding and grain rotation, which becomes increasingly active as the grain size decreases. Additionally, it is believed that a reduction in grain size can also alleviate the strong mechanical anisotropy caused by its HCP crystal structure [79]. Coarse-grained HCP materials manufactured by deformation like rolling usually exhibit strong basal texture, causing strong mechanical anisotropy [80]. Many grain refining processes like severe plastic deformation (SPD) are reported to be able to change such texture, leading to improved isotropy through more activation of different slip systems [81-84]. Another possible factor contributing to the improved mechanical anisotropy of nano-crystalline materials is the reduced activation of twinning as grain sizes reduce [79, 85], as dominating activation of a single twinning system can cause strong anisotropy in HCP materials [18, 86]. With so much potential for tailoring mechanical properties, it is no wonder that

nano-crystalline materials have attracted so much interest from numerous researchers in the past decades.

While several researches on nano-crystalline materials exist, finding an effective yet simple approach to synthesize the nano-crystalline materials used for the study is always the first challenge. Existing grain refining methods can be generally divided into two categories: bottom-up (e.g. additive manufacturing, also known as 3D printing [47, 87, 88], adding of grain refiner [89-93], and special manufacturing process [94-96], etc.) and top-down (e.g. deformation-induced grain refining [97]). Despite having been attracting great interest and showing great potential, 3D printing is currently suffering from issues like porosities, inhomogeneity, high cost, etc., limiting its application to only small-scale production [98]. The extent of refining is also limited to micron level for most 3D printing due to the high local temperature often involved in their manufacturing processes [99]. Another bottom-up approach is by adding either inoculation particles [100, 101] or grain refining elements like aluminum, calcium, silicon, zirconium, etc., [90-93] However, the grain refining is too usually limited to micron level and hard to obtain real nano-crystalline, the same holds true for some other processing-related approaches like increasing cooling rate, providing agitation [90].

To manufacture true nano-grained (submicron) materials, plastic deformation might be one of the easiest approaches. It's been a long time since people use plastic deformation as a convenient and effective grain refining method, small grains form during plastic deformation by rearrangement of dislocations to form GBs/sub-GBs [102] and following dynamic recrystallization induced by the heat caused by deformation [103]. The primary principle behind this approach is fairly simple, the heavier you apply the plastic deformation, the finer the grains you get. However, using traditional deformation methods like rolling on HCP materials like Mg usually results in cracking and fracturing when a large amount of plastic deformation is applied, limiting the amount of grain refining that could be achieved. Fortunately, in the past few decades, numerous SPD techniques

that are capable of overcoming such drawbacks have been invented, including high-pressure torsion (HPT) [104], equal channel angular pressing (ECAP) [105], surface nano crystallization (SNC) [106], etc., paving the pathway to sub-micron nano-grains down to below 10 nm [106, 107]. Illustration of two commonly used SPD techniques (HPT and ECAP) is shown in Figure 2.4.

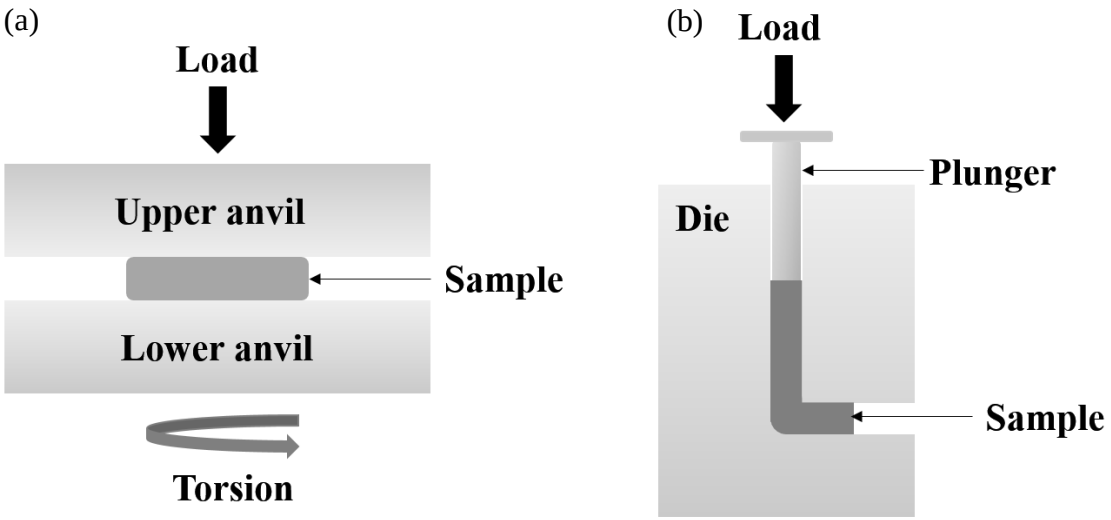

Figure 2.4 Illustration of some SPD techniques. (a) HPT and (b) ECAP.

As one of the approaches that is capable of synthesizing true nano-grained materials [106, 107], SPD has been widely applied as an effective approach to synthesize nano-crystalline materials [108-113]. However, despite their excellent ability in refining grains, most SPD methods (e.g. HPT [104] and ECAP [105] which are the most common two) suffer from issues like dedicated equipment, high cost, and complicated manufacturing process [114], making them less accessible to numerous researchers interested in nano-crystalline. SNC, as a special SPD targeting the material surface, is much easier to implement as only the surface of the materials is nano-crystallized, equipment like a simple high-speed rolling head, which is much more accessible compared to what are used for HPT and ECAP, can effectively produce well-defined nano-crystalline surface layers with grain size ~ a few hundred nanometers [115, 116]. Additionally, due to its surface treatment nature, the amount of strain due to SNC gradually reduces as the distances from the surface increase,

thus naturally producing gradient structures whose grain sizes are proportional to the distance to the treated surface. Such gradient structures are reported to have much higher ductility compared to the pure nano-crystalline materials which generally suffer from extremely limited ductility, while still maintaining excellent strength compared to their coarse-grained counterparts [45, 64, 117], offering the possibility for addressing the long-standing ductility problem of nano-crystalline materials. Thus SNC provides a simple yet effective way to manufacture nano-crystalline materials, improving the strength and ductility simultaneously.

Another issue that exists for almost all existing nano-crystalline synthesizing methods is the difficulty in the preparation of TEM thin film samples. Due to the extremely small size of the microstructure of nano-crystalline materials, TEM observation, which can offer high spatial resolution down to atomic scale, is usually necessary for detailed characterization. The schematic illustration of a conventional modern TEM is shown in Figure 2.5. Much like optical microscopes working under transmission mode but replaced light with electrons and optical lens with magnetic lens, TEM benefits from the much shorter wavelength of electrons and thus has much higher resolution even with large imperfection in the current magnetic lens like aberration. More importantly, the spacing between atoms falls into the same scale as that of the high-speed electrons, enabling the acquisition of diffraction patterns which offers valuable crystallographic information. And by simply changing the strength of the intermediate lens as illustrated in Figure 2.5, one can easily switch between diffraction and image mode in TEM, such trait makes TEM a powerful tool capable of simultaneously obtaining both morphological and crystallographic information over very localized area, which is not possible for any other characterization techniques.

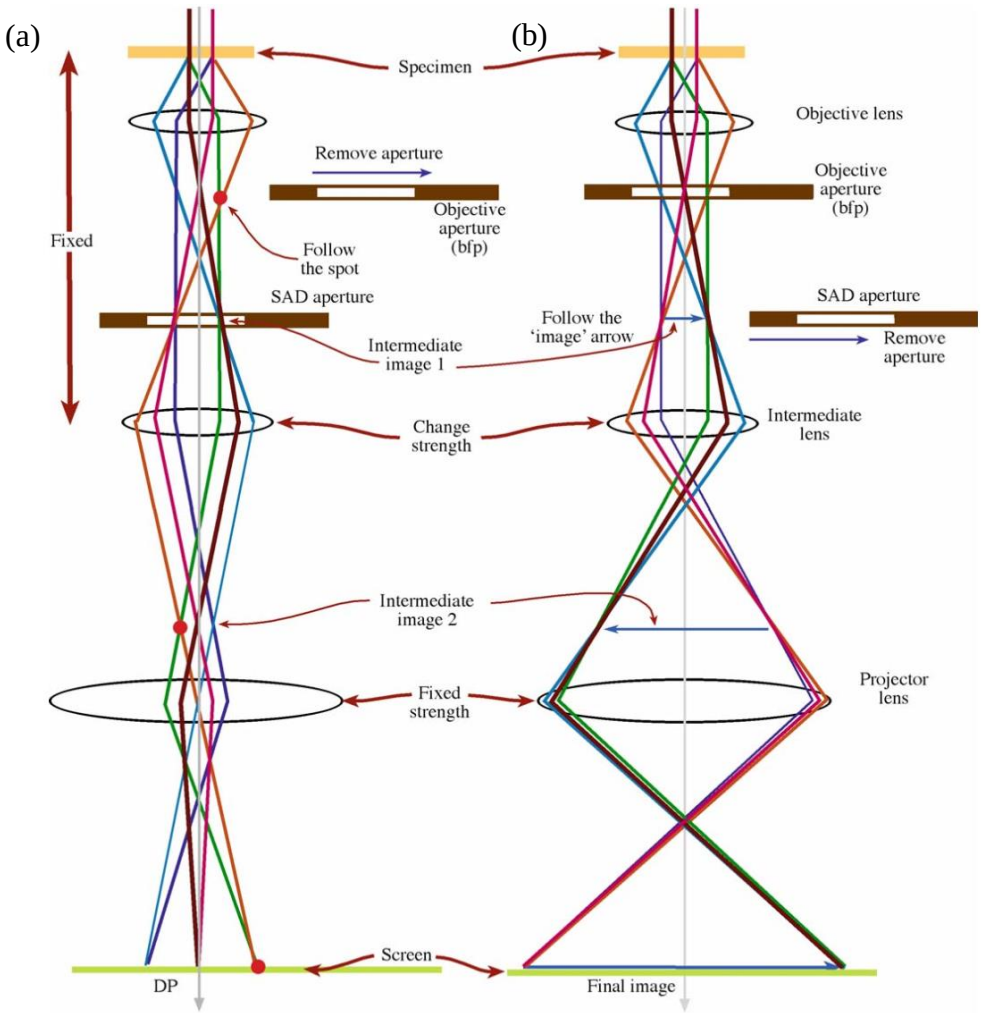

Figure 2.5 Two basic operation modes of modern TEM. (a) Diffraction mode and (b) image mode [138].

Naturally, it is necessary to prepare thin film samples out of the nano-crystalline material. Existing approaches generally use a two-step approach where synthesizing nano-crystalline and preparation of TEM sample are done separately. Methods like twin-jet polishing, ion-milling and focused-ion beam (FIB), etc. are used to thin the bulk nano-crystalline samples into electron transparency that is needed for following TEM inspection. Apart from extra time and cost (especially the case if a large number of samples need to be prepared using FIB), these sample preparation processes are also known to introduce artifacts or cause sample damage, for example, hydrides can form due to the twin-jet polishing, while ion-milling and FIB can easily cause sample damage and artifacts due to the constant bombarding on samples [118, 119]. If a versatile single-step approach exists that

can synthesize nano-crystalline and make it electron transparent at the same time, it would be of great help to researchers interested in studying nano-crystalline materials.

The above-mentioned SNC phenomenon offers a potential solution to this problem, consider bulk samples being carefully mechanical polished, the plastic deformation process caused by the polishing is known to cause mechanically influence layers [115, 120], thus theoretically if adequate polishing parameters are used, nano-crystalline layers can form because of the polishing process. In the meantime, the mechanical polishing process keeps removing materials, making the samples thinner. Therefore, one may wonder, under certain experimental designs, if it is possible to produce nano-crystalline materials while thinning them to electron transparency simultaneously so that they can be directly used for TEM observation.

Benefiting most from the strengthening effect of grain-refining yet suffering less from softening [47, 54] and limited ductility [121, 122] of extremely fine grains, materials with intermediate grain size (10 nm <d< 1 μm) are probably the most promising one in terms of the practical application of nano-crystalline materials. As the grain size decreases, while the once dominating full dislocations become less active, additional grain boundaries related deformation modes like grain boundary sliding, grain boundary migration, grain rotation, etc. gradually become actively contributing to the deformation process, causing many unique mechanical responses of nano-crystalline materials, e.g., “softening” of extremely fine nano-crystalline materials. However, despite of many research dedicated to this topic, the detailed deformation mechanism for nano-crystalline with intermediate grain size is still debatable, for example, grain boundary sliding has been considered to contribute significantly to plastic deformation in materials with an average grain size of ~90 nm [123], while extensive dislocation activity has also been found in nano-crystalline as small as ~10 nm [124]. This complexity arises possibly because all the above-mentioned deformation mechanisms may contribute to deformation, additionally, the potential coupling between deformation mechanisms can make the process even more elusive. Despite a few

simulation results suggesting the possible coupling between dislocation slips and grain rotation [125-128], where grain rotation is believed to reduce the flow stress needed for deformation. The actual experimental results supporting such theory are largely absent, possibly due to the difficulty in tracking both the grain rotation and dislocation activity dynamically during deformation. Thus it is important to get further understanding of the deformation mechanism, especially the potential coupling effect, of nano-crystalline materials with intermediate grain size.

2.4 Challenges in characterizing dynamic processes in real-time

Grain rotation becomes more active in nano-crystalline materials, however, certain challenges exist in the corresponding orientation characterization. Conventionally, fully quantified grain orientation data can be extracted using either Kikuchi lines based methods like electron backscatter diffraction (EBSD) in scanning electron microscopy (SEM), transmission Kikuchi diffraction (TKD) in SEM, or a number of diffraction spot-based methods in TEM [129-134]. All these techniques require sampling over a relatively large area in reciprocal space for each pixel in one image, while being fully quantified, it is a time-consuming process that can take hours to complete one single mapping even with the most advanced detectors. Consequently, it is challenging to use these techniques to keep track of the orientation change during dynamic processes like plastic deformation. A few alternatives have been proposed to bypass the problem, for example, high-resolution TEM (HRTEM) fringe images which give the orientation of the crystal in real-time have been successfully used to track the change in mis-orientation between adjacent grains, as demonstrated by Ke et al. [135], the first experimental evidence of grain rotation of nano-crystalline using HRTEM imaging.

However, serious limitation exists for such atomic image-based approach: first is the small viewing area which usually only includes a few grains, making the analysis of the possible coupled deformation between a large number of grains virtually impossible; another problem is that

HRTEM images only form when grains are under certain orientation, once the grain rotates away, one essentially loses track of its orientation change whatsoever.

Another commonly used technique is dark-field (DF) imaging. Instead of sampling over the whole reciprocal space, electrons from only a small selected area determined by the objective aperture are collected, offering the possibility for real-time characterizing. While not able to provide fully quantified orientation information as in the case of EBSD etc., such image-based approach still offers orientation information. Taking advantage of Bragg's law of diffraction, areas showing bright contrast in DF images have their plane used for imaging nearly parallel to the viewing direction, which means any change in the contrast corresponds to the change in grain orientation. Such approaches have been proven effective in characterizing the grain rotation of nano-crystalline materials [136, 137]. Unfortunately, the conventional DF imaging used only a fraction of the diffraction rings, which means only a very small portion of grains in contrast are actually being tracked. Valuable information contained in other part of the diffraction rings, which is large compared to the selected portion, is simply discarded and inaccessible to further analysis, bringing up the problem that coupling effects between multiple grains can be harder to observe as much fewer grains show high contrast under conventional DF imaging. Another problem is that DF imaging fails to recognize orientation change around the diffraction rings, that is to say, when the diffracted spots shift to other part of the same diffraction ring, despite the fact that the planes are still essentially edge-on, conventional DF imaging essentially treats such scenario as rotating away from the diffraction conditions. Such drawbacks make conventional DF imaging less ideal for characterizing nano-crystalline materials. Consequently, a modified version called HCDF has been proposed, which enables the whole diffraction ring(s) to be used for imaging by beam tilting and rotating [138]. However, unlike conventional DF, past research using HCDF is mostly limited to things like capturing the morphology (real space information), measuring the grain size, tracking

grain growth, or imaging dislocations [139-141]. Researches trying to extract valuable orientation information (reciprocal space information) from the HCDF images remain largely absent.

2.5 Manipulation of Dislocations

Being the most common plastic deformation carrier in metallic materials, dislocations play important roles in the deformation process and have been used extensively as a strengthening method in various alloy systems. There are generally two types of dislocation strengthening mechanisms in literature based on the dislocation density. The most common one is the forest strengthening (work-hardening) which is mostly found in the deformation of coarse-grained materials with a high pre-existing dislocation density. The gliding dislocations in these cases are hindered or trapped by a high density of dislocations, causing the multiplication of dislocations which further increases the dislocation density and interaction between dislocations and consequently leads to improved strength [142, 143]. However, if the pre-existing dislocation density is considerably small or dislocations are easy to be annihilated at interfaces, like in the case of nano-crystalline, the multiplication of dislocation is severely limited and the force required to generate new dislocation sources, which is generally very high, becomes the major limiting factor during deformation, leading to the transition to another strengthening mechanism called source-limited strengthening [144, 145].

In the current study, we focus on the possibility of idealizing the dislocation configuration in hope of maximizing the forest strengthening effect. The dislocation density plays a key role in such strengthening process, while introducing extra dislocations by plastic deformation has been proved to be an effective strengthening method and is widely used in real-life manufacturing, one may wonder how the nature of dislocations (type, distribution, configuration, etc.) involved in the forest strengthening process can influence the strengthening process. To minimize the strain energy, dislocations tend to re-arrange themselves into LEDS [73, 146], examples being dislocation dipoles,

muti-poles, and the “Taylor lattices” [147-149], along with structures like dislocation walls and cells which define almost dislocation-free volumes separated by dense dislocation boundaries.

Theoretical calculations predict that the effect of work hardening is not solely controlled by dislocation density, factors like the type and specific configuration of dislocations can also be influential [65, 66], which has been verified experimentally by the well-established work hardening stages observed in cubic materials subjected to fatigue process [67-71]. For example, due to the “screening” effect between oppositely signed dislocations, the work hardening behaviors caused by LEDS differ significantly from that of random dislocation forest. Such unique trait makes LEDS potential for tuning the work hardening of crystalline materials and thus improving their mechanical performance.

The work hardening of Mg is much less well-understood compared to cubic materials. Most successful works utilizing dislocations to strengthen Mg and its alloys focus on either dislocation density or dislocation type, rather than its configuration like in the case of LEDS. The study on dislocation structures in Mg is largely limited to dislocation networks (e.g., dislocations at tilt/twist grain boundaries [75, 150] or dislocation networks caused by tangling of dislocations [151]) or random forest dislocations [143]. Limited studies exist in Mg on long-range periodical structures like the “Taylor lattice”, with only few reports claiming the existence of small-scale periodical structures like dislocation dipoles/multi-poles [152].

Recently, periodical LEDS similar to the “Taylor lattice” has been reported in hot-extruded Mg alloys, in the form of ordered <c>-screw dislocation arrays segregated with Gd [153]. Such structure is promising in terms of improving both the strength and ductility of Mg due to its unique configuration. However, whether such structure exists without the aid of any solute elements still remains elusive, as solute elements are known to reduce dislocation core energy leading to improved dislocation stability [154]. More importantly, planar slip, which is essential to the formation of many ordered dislocation structures including the “Taylor lattice”, can be promoted

through the addition of solute elements [73, 155]. Thus it is essential to decouple the possible effects of solute elements from the formation of such dislocation structure if one is to better utilize it for strengthening. It should be noted since we are essentially observing the projection of samples, Moiré fringes which originate from overlapping grains may produce images similar that of ordered structure like in the case of periodical dislocation array. This is not less problematic in ref. [153] since the segregation of Gd makes the presence of dislocations clearly visible. However, it can be tricky if one was to differentiate them in pure metal where no indicators like solute atoms are available.

Chapter 3 Experimental: Challenges and solutions

3.1 Initial Microstructure

3.1.1 Mg-Gd binary alloys

The initial materials used to synthesize the nano-grains was a Mg-Gd (2.0 wt.%) ingot shown in Figure 3.1 (a), and was wire-cut into cylinders with dimensions Φ10 mm*20 mm (±0.02 mm) by strategies illustrated in Figure 3.1 (b). Gd was chosen in hope to stabilize the nano-crystalline, because RE elements like Gd are known to segregate into GBs and thus stabilizing them. A solution treatment at 500 ^{o}C for 8 hours was conducted on all cylinders. While most samples used in the current study were made out of the solid-solution treated samples, in order to investigate the possible effect of different initial microstructure on the nano-crystalline TEM sample preparation, additional hot-compression at 400 ^{o}C until fracture were conducted on some cylinder samples using five different deformation rates of 0.5 mm/min, 5 mm/min, 20 mm/min and 200 mm/min. All samples were immediately water quenched following the hot compression. To facilitate further TEM sample preparation, thin slices with a thickness of ~1 mm were wire-cut from cylinder samples as illustrated in Figure 3.1 (c), from which small near rectangular TEM samples with size ~3 mm*2 mm* 1mm were cut for further mechanical polishing to make wedge TEM samples.

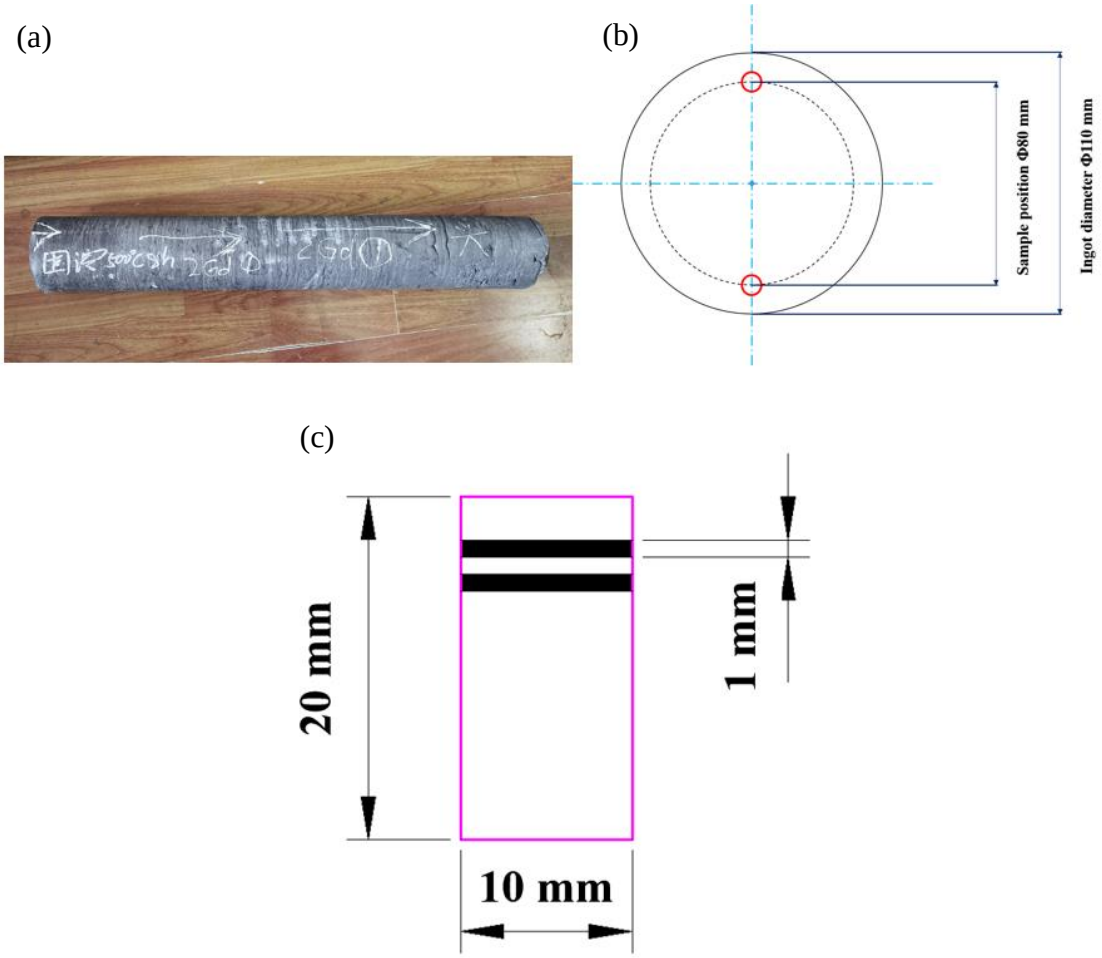

Figure 3.1 Illustration of the raw materials used for synthesizing nano-crystalline. (a) Raw material Mg-Gd (2.0 wt.%) binary alloy ingot; (b) schematic illustration of how cylinder samples were cut from the raw ingot, dashed circle indicates where cylinders (marked by the red bold circle) were cut; (c) schematic illustration of how thin slices for further TEM samples preparation were cut from cylinders.

A typical EBSD inversed pole figure (IPF) of solid-solution treated samples is shown in Figure 3.2(a), coarse-grained microstructure with grain size over a few hundred microns can be clearly identified.

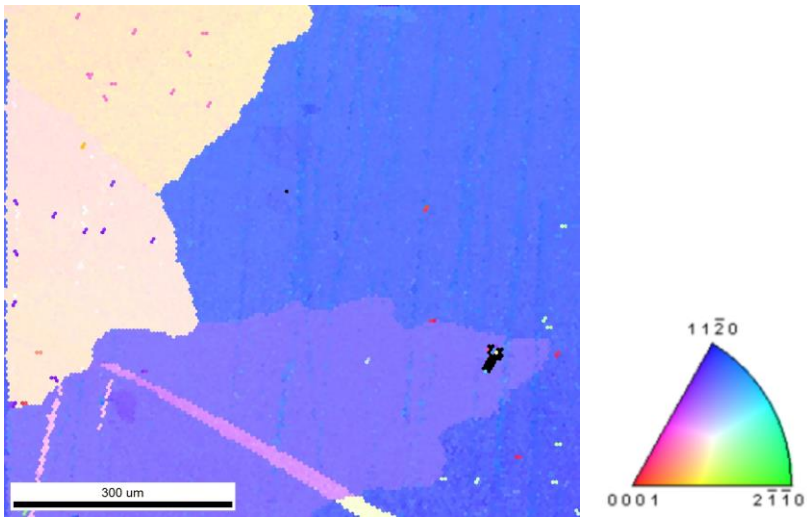

Figure 3.2 Typical IPF of solid-solution treated samples, showing coarse-grained microstructure.

As can be seen in the bright-field (BF) image shown in Figure 3.3 (a), the TEM micrograph gives consistent results with the EBSD data, showing big grains with no grain boundaries being captured in any observable area under TEM which is reasonable considering the big grain sizes. Though having underwent high-temperature solid-solution treatment, there are still dislocations remaining inside the sample, which lies dominantly on the basal planes as marked by the red circle. These dislocations are likely of basal <a> type considering their configuration parallel to the basal planes, but recent reports have shown the possibility of basal dissociation of <c+a> dislocations, causing them to be essentially sessile [26, 156, 157]. To identify the type of these dislocations, tilting experiments have been conducted to analyze the visibility of dislocations under different two-beam conditions. When a specific g vector is used to form the DF image under two-beam conditions, only dislocations with dot product $g*b \neq 0$ (b is the Burgers' vector of the dislocations) show contrast and are visible in the image [138]. Thus with a few combinations of g vectors, the Burgers' vector b of the dislocations can be determined unambiguously. As can be seen in the DF imaging shown in Figure 3.3 (b), dislocations inside the red circles are visible under $g=(01\bar{1}0)$, which means <c>-dislocations are not possible as the product will be zero. Still both <a> and <c+a> dislocations can show contrast under such beam condition, thus additional DF imaging using g=(0002) has been

done as can be seen in Figure 3.3 (c). From this figure, it can be clearly seen that those dislocations showing contrast previously under g=(01$\bar{1}$0) are now completely invisible, leaving only <a> dislocations to be the only possibility, which is reasonable considering the dominating role of basal slip for Mg.

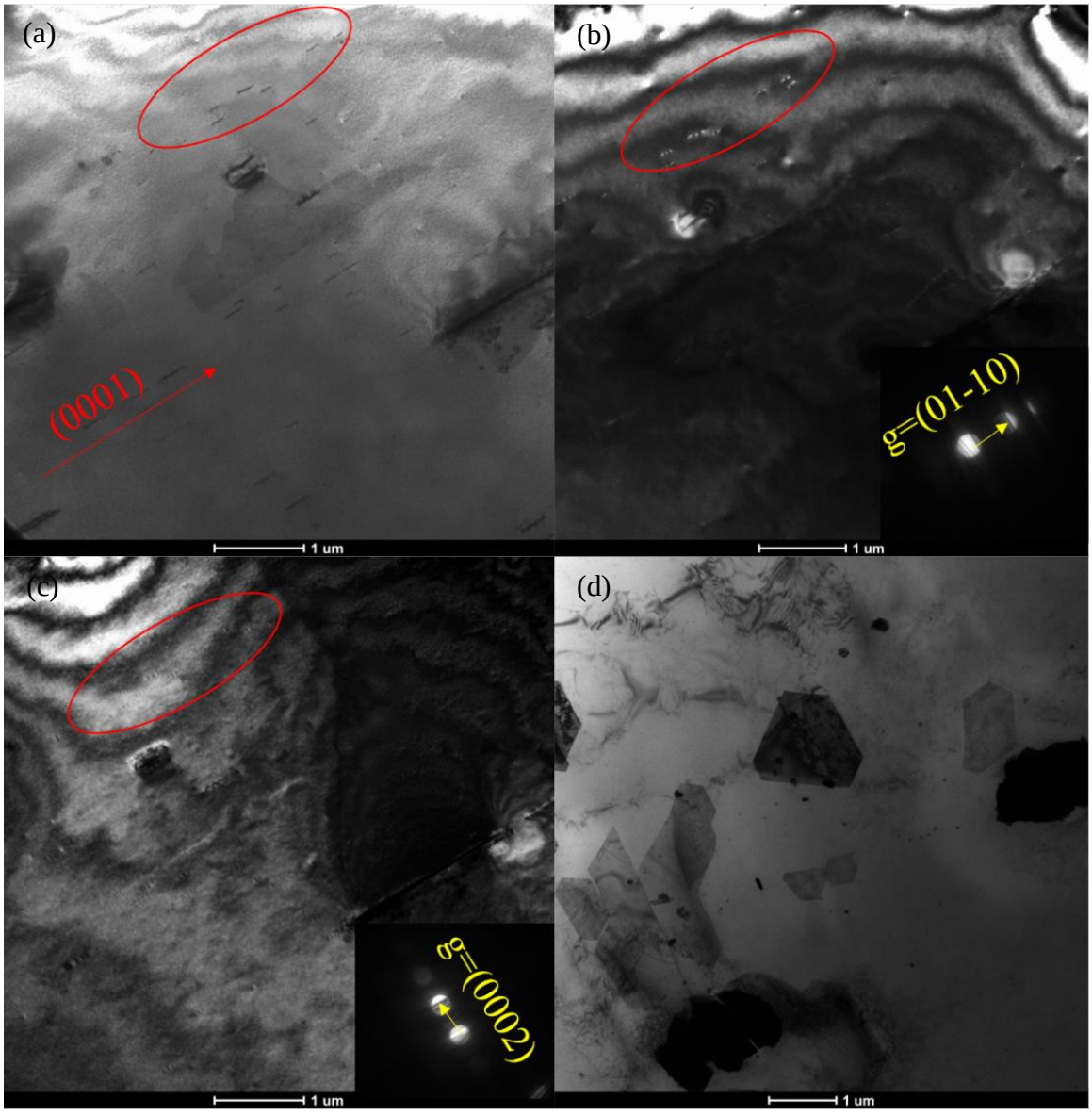

Figure 3.3 TEM characterization on the microstructure of the Mg-Gd (2 wt. %) alloys. (a) BF image showing the typical microstructure of the solid-solution treated samples prepared by conventional twin-jet polishing, dislocations lying on the basal planes can be seen as marked by the red circle; DF images taken under two-beam conditions using (b) g=(01$\bar{1}$0) and (c) g=(0002); (d) precipitates with regular shape found in the sample, the viewing direction is [11$\bar{2}$3].

Apart from dislocations, precipitates with regular shapes have also been identified in some areas. Viewed along [$11\bar{2}3$], as can be seen in Figure 3.4 (d), the sizes of these precipitates are relatively large, usually ~ 1 micron. Corresponding energy dispersive spectrum (EDS) mappings shown in Figure 3.4 (a) clearly indicate that these particles are enriched of Gd. While they seem to be particles viewed along [$11\bar{2}3$] as shown in Figure 3.4 (b), once viewed along the <a>-axis ([$11\bar{2}0$]), all these precipitates become thin plates lying perpendicular to the basal planes. This means instead of particles, these precipitates are actually thin plates lying along the <c>-axis. Past research on Mg-RE alloys has shown Gd in Mg precipitates by the following order $\beta'' \rightarrow \beta' \rightarrow \beta_1 \rightarrow \beta$, taking morphology, orientation, and precipitate sizes into account, only the equilibrium β phase matches the record in the current case [158].

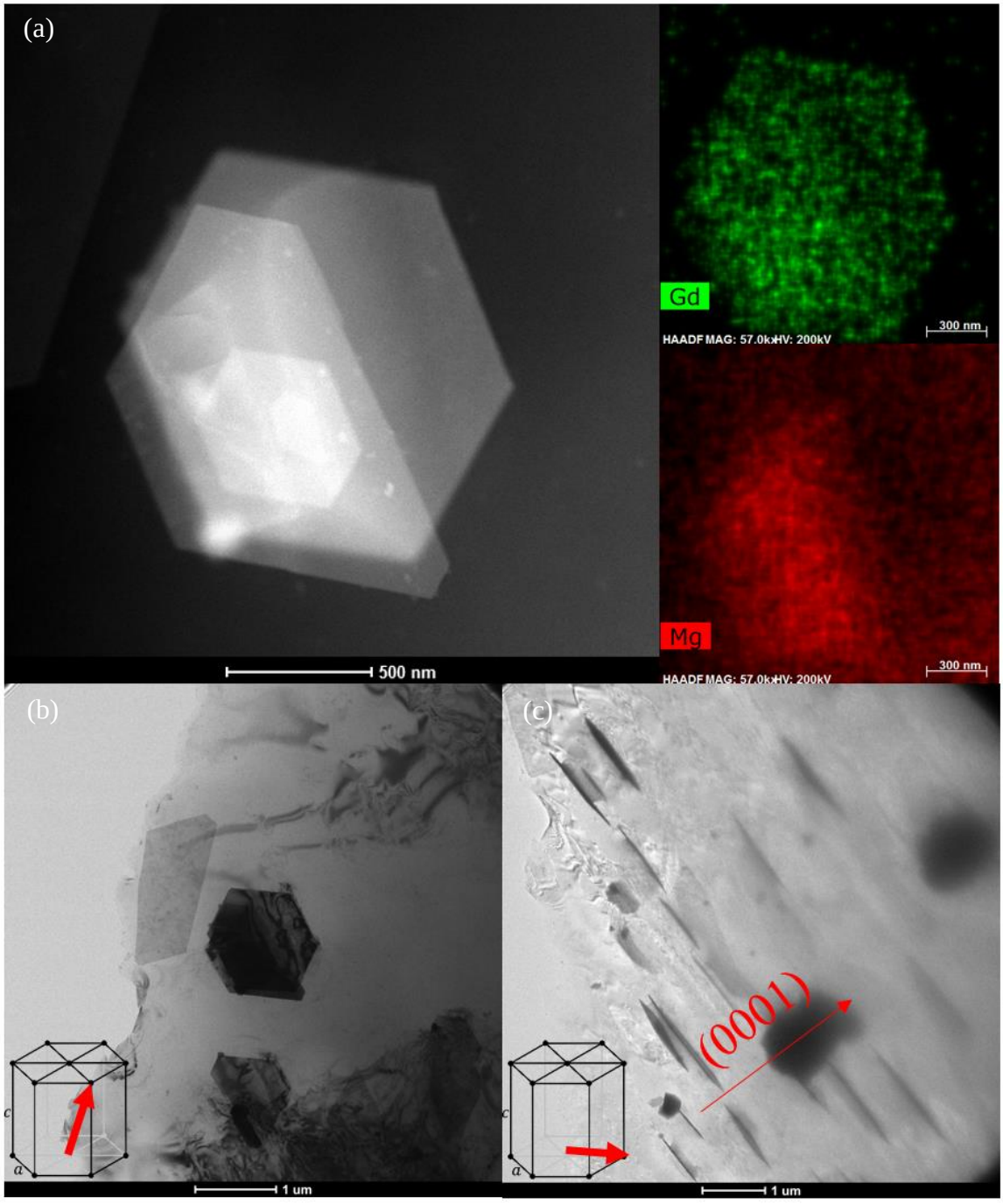

Figure 3.4 TEM characterization on the precipitates found in the Mg-Gd (2 wt. %) alloys. (a) high-angle annular dark-filed (HAADF) image and corresponding EDS mapping on one of the precipitates; morphology of precipitates viewed along (b) [11$\bar{2}$3] and (c) [11$\bar{2}$0].

3.1.2 Hot-extruded Pure Mg

The raw materials used to synthesize the desired dislocation structures was a hot-extruded Mg plate with 99.99% purity, the as-received plate possesses a strong basal plate commonly found in Mg subjected to similar hot deformation.

A large number of dislocations have been introduced by the hot-extrusion process, as can be seen in the TEM-BF micrograph of the as-received plate shown in Figure 3.5, but detailed TEM examination reveals no evidence of the periodical dislocation structures which we seek to introduce using the following hot-compression.

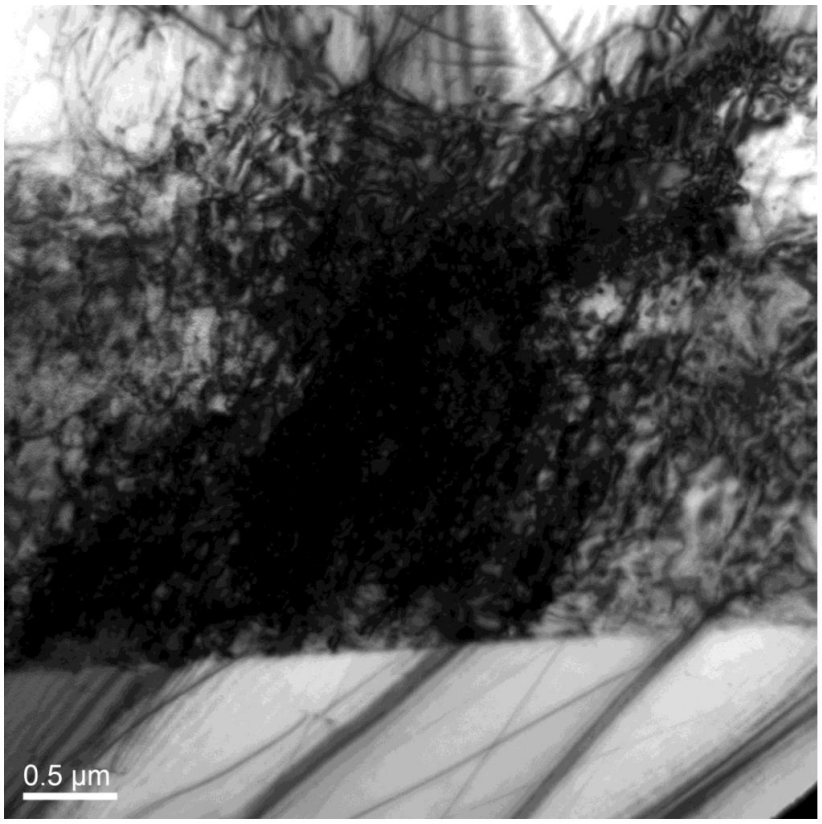

Figure 3.5 Microstructure of the initial hot-extruded samples. The complex black contrast in the figure indicates a high density of pre-existing dislocations.

3.2 Experimental Design for Tailoring Grain Boundaries via Simple Mechanical Polishing

3.2.1 Experimental Design: Sample Preparation Using Simple Mechanical Polishing

The idea of preparing TEM samples using direct mechanical polishing dates back to the mid-90s when the Tripod polisher was introduced [159], the idea is to apply a tilting angle during polishing so that areas at the tip of the wedge sample can be thin enough to be electron transparency. In most studies, the wedge angles are set to be relatively small (usually $<1^{o}$) [159, 160]. Later in 2001, a variation using a high tilting angle to produce wedge samples was proposed by Li et al. [161], the high polishing angle makes the tip more robust thus freeing the polishing process of constant monitoring of sample thickness, making the polishing easier and less likely to damage the tip. Preparing wedge TEM samples by mechanical polishing has many advantages compared to conventional TEM preparation methods (e.g., ion milling, twin-jet polishing, etc.), for example, large observable area, ability to selectively thin certain areas of interest, applicable to most materials, etc.[159] Despite of its flexibility, most of such wedge polishing techniques are used to prepare TEM samples of non-metal materials, while for metallic materials, polishing is almost always done using either twin-jet polishing, ion milling, or FIB, possibly due to the fact that highly standardized preparation procedures exist in abundant literature. In the following sections, it will be shown that using a similar mechanical polishing approach to what was used by Li et al. [161], nano-crystalline TEM wedge samples can be prepared quickly without the aid of any additional polishing process like ion milling.

A precise polishing system Multiprep^{TM} manufactured by Allied Tech^{TM} was used for the preparation of nano-crystalline TEM wedge samples. The TEM sample preparation consists of polishing on both upper and lower surfaces of samples, a tilting angle of 4^{o} was applied during the second surface polishing to produce the wedge necessary for TEM observation. Crystalbond^{TM} was used to attach the sample to the polishing mount shown in Figure 3.6 (a) for the first surface

polishing, while for the second surface polishing, superglue was used to enhance the adhesion which can be removed later by soaking in an acetone bath. A water-free, alcohol-based lubricant was used throughout the polishing process, to improve the polishing quality and reduce possible oxidation during the polishing [159]. Sandpapers (Diamond lapping film of 6 μm, 3 μm, 1 μm, and 0.5 μm) were used sequentially, and a minimum polishing thickness of 20 μm was set for each step to avoid any large scratches left by previous polishing. The polishing rate was set to 20 rpm except for the final polishing of 5 rpm (the slowest one available in the current machine) to minimize the possibility of fracture and damage to the wedge tip.

3.2.1.1 Polishing the First Surface

Before any polishing, alignment of the polishing machine is required to make sure the rotation platen where sandpapers are attached remains essentially flat, no tilting angle is applied during this step. After the parallel polishing condition is secured, the near rectangular sample is first attached to the polishing mount using Crystalbond™ as shown in Figure 3.6 (b). Note the sample is extending out of the edge of the polishing mount a little to allow abrasion and the sample edge should be as parallel as possible to the edge of the polishing mount as recommended by ref. [159]. The applied glue needs to be evenly smeared to the mount to avoid any tilting of the samples during polishing. Then the polishing mount is attached to a cam-lock adapter shown in Figure 3.6 (c).

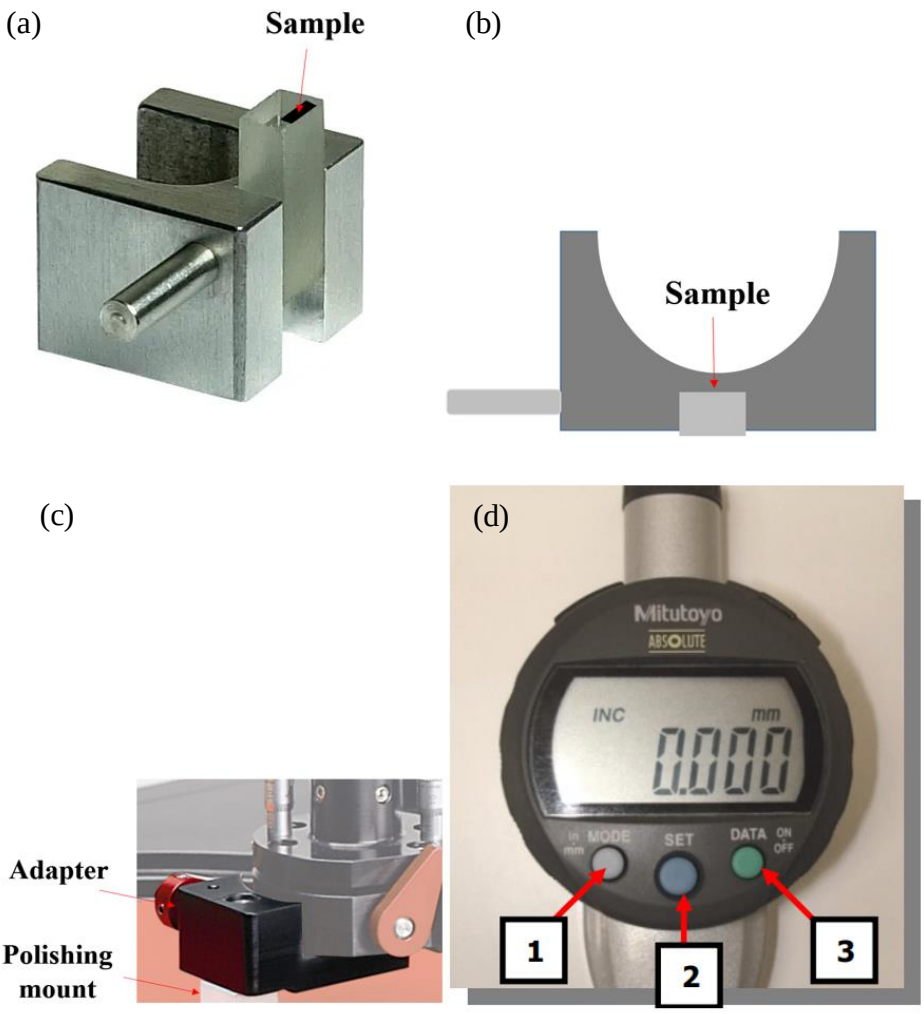

Figure 3.6 Illustration of the sample mounting process and polishing on the first surface. (a) The stage used to mount the samples; (b) top-view schematic illustration of sample mounting during the first surface polishing; (c) adapter to which the polishing mount is attached; (d) digital indicator used to measure the relative thickness reduction during polishing.

Mechanical polishing is then applied using a set of sandpapers with a particle size of 6 μm, 3 μm, 1 μm, and 0.5 μm. Starting from the coarsest one (6 μm), the polishing rate is held constant at 20 rpm, and lubricant is constantly added throughout the polishing process. It should be noted that polishing produces visible debris on the sandpaper and should be cleaned constantly. Though it is hard to measure the exact thickness of the sample, the relative thickness reduction can be monitored by a digital indicator attached to the polishing machine as shown in Figure 3.6 (d), by simply comparing two values taken before and after polishing. The first polishing is only aimed to remove

any large scratches or defects on the surface, thus the only requirement is to keep a minimum polishing thickness of 20 μm for each polishing pass. Once the first surface is free of visible large scratches, a heating stage is used to melt the Crystalbond™ and detach the sample from the mount. To minimize possible oxidation, heating should stop as soon as the sample can be detached. It should also be noted that should any Crystalbond™ become attached to the polished surface, soaking in an acetone bath should be performed to completely dissolve the glue to improve the further polishing quality. Henceforth, any manipulation of the sample is recommended using a vacuum tweezer, as the small sample size makes it easy to mishandle using conventional tweezers, causing possible damage to the sample. The Crystalbond™ remained on the polishing mount needs to be removed completely, a parallel polishing on 6 μm sandpaper for one minute can effectively clean all the remaining glue in most cases.

3.2.1.2 Polishing the Second Surface and Introducing the Wedge

For polishing on the second surface, the sample needs to be glued using superglue in the same manner as the first surface shown in Figure 3.6 (b), note that the polished first surface needs to face the sample mount. Crystalbond™ is not recommended during the second polishing, because the sample tends to detach from the mount as the thickness reduces. A polishing using sandpaper series of 6 μm, 3 μm, 1 μm, and 0.5 μm, similar to the first surface polishing, is done first before introducing the wedge, to get rid of anything attached to the surface and ensure a relatively flat and scratch-free surface.

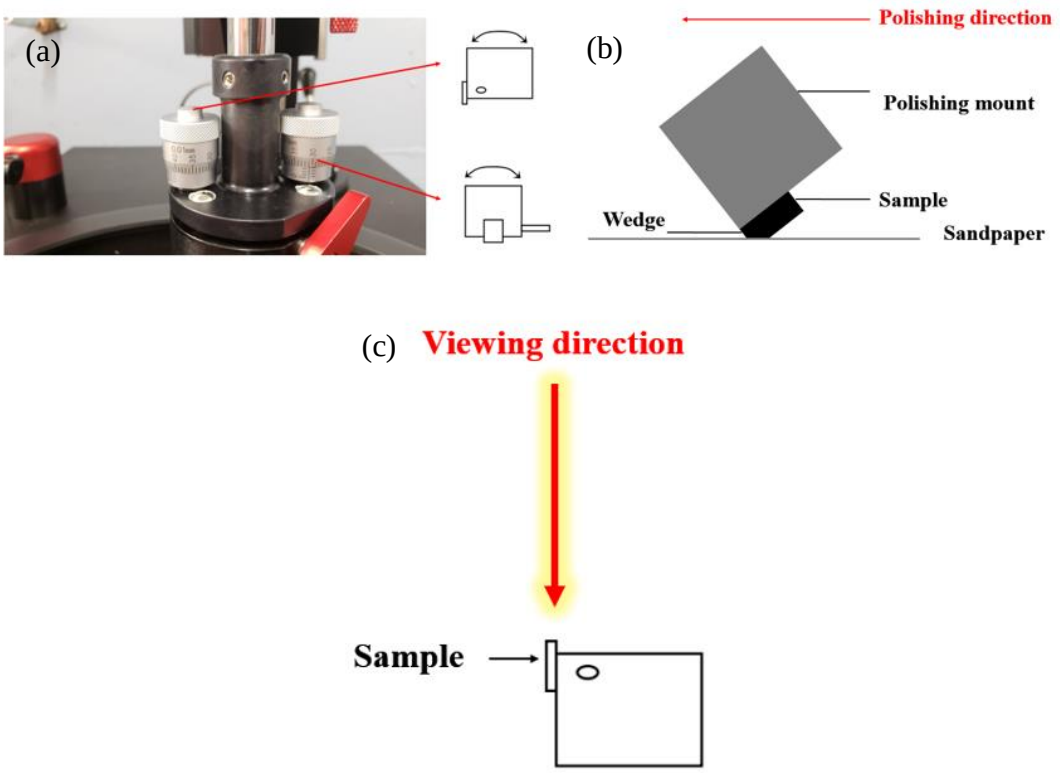

Figure 3.7 Illustration of the second surface polishing. (a) Angular adjustments knobs, the left one is for front and back (axial) adjustment, the right one is for left and right (radial) adjustment, in the current case, only the left one is needed for the polishing of wedge sample; (b) side view illustration of how the wedge is introduced; (c) cross-section viewing using an optical microscope to monitor the remaining thickness.

To introduce the wedge needed for TEM observation, one of the angular adjustment knobs of the polishing machine shown in Figure 3.7 (a) is needed. These two knobs provide both radial and axial adjustments, but only axial adjustment is required for the preparation of wedge samples. Thus the right knob is held constant while the left one is set so that the sample is tilted 4^{o} along the axial direction. Once the tilting angle is set, the polishing process shown in Figure 3.7 (b) can be conducted to produce the wedge sample. It is important to note that the polishing direction (indicated by the red arrow in Figure 3.7 (b)) should always be facing the wedge, otherwise the wedge can be easily damaged due to the polishing process.

The tilted polishing also uses the same sandpaper series (6 μm, 3 μm, 1 μm, and 0.5 μm) to gradually reduce the thickness of samples, avoiding any large scratches. Although precise thickness

measurement is not essential to the current polishing technique, it is a good practice to keep track of the remaining thickness during wedge sample preparation. An optical microscope can be very helpful, a cross-section observation as shown in Figure 3.7 (c) is recommended to keep monitoring the remaining thickness of the wedge sample.

In the preparation of wedge TEM samples of non-metal materials, the completion of the polishing is usually determined by the presence of interference fringes coming from a very thin edge as shown in Figure 3.8 (a) [159]. However, in the current case of Mg alloys, it is usually hard to see these fringes even when the edge is formed or on samples that have been checked as good under TEM, possibly due to the limited magnification of the optical microscope used in the current study. Alternatively, another simpler criterion has been created to mark the completion of the polishing process. As illustrated in Figure 3.8 (b), due to the geometrical set-up of the polishing, a "blank" area indicated by the red line appears between the sample tip and the polishing mount edge once the wedge is formed, therefore such "blank" area can be used as an indicator to the formation of the wedge, as demonstrated by the experimental image shown in Figure 3.8 (c). As pointed out by Li et al. [161], the tolerance of such polishing technique is high due to the material removal pattern shown in Figure 3.8 (d). When the wedge is formed, even if one continues polishing, the sample essentially recedes laterally, keeping the thin tip part at all times. However, in practice it is recommended to stop polishing quickly after the "blank" area is observed, to reduce the change of potential damage to the tip due to further polishing.

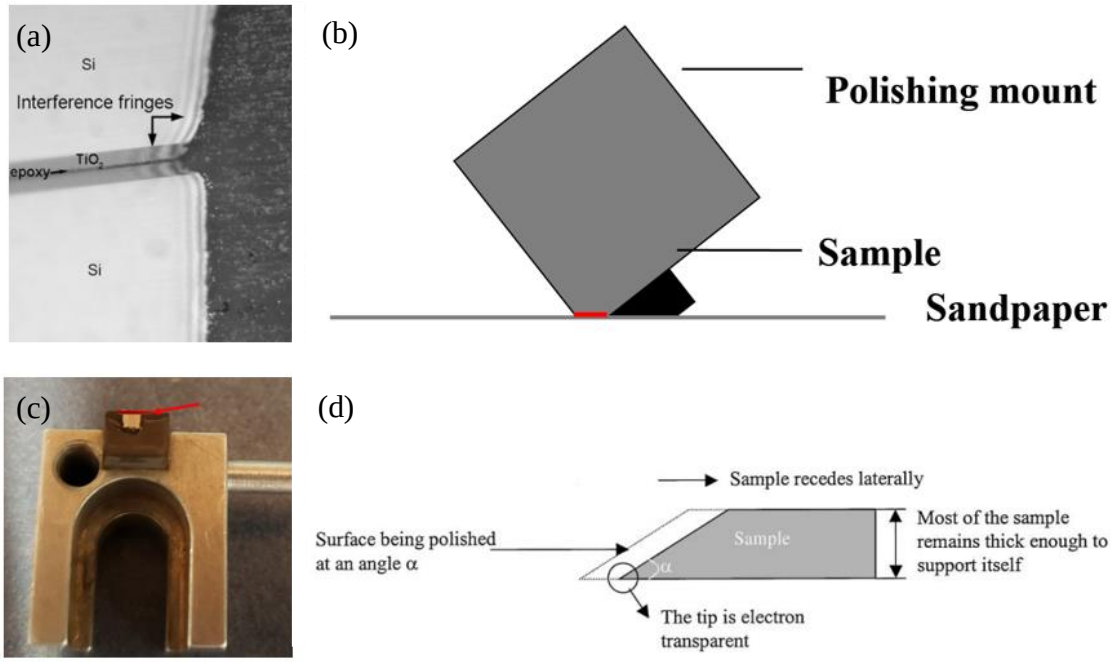

Figure 3.8 Detailed polishing and sample removing set-up. (a) Interference fringes near the prepared wedge in the TiO_2/Si sample, which can be used as a sign for the completion of the wedge, adopted from ref. [159]; (b) illustration of when the wedge is formed, note the "blank" area (marked by the red line) between the wedge and the edge of the polishing mount; (c) an experimental image showing the "blank" area once the wedge is formed; (d) schematic of high angle wedge polishing, adopted from ref. [161].

Once the polishing completes, the wedge sample needs to be soaked in acetone to dissolve the superglue used for mounting. Due to the extremely small size of the sample, collecting it from the beaker can prove challenging and risks damaging the tip. Thus a filter paper rolled into a conical shape is put into the beaker to collect the sample once it is detached from the polishing mount, as illustrated in Figure 3.9 (a). Using the filter paper approach, transferring the sample from the beaker involves simply unfolding the paper and waiting for it to dry up.

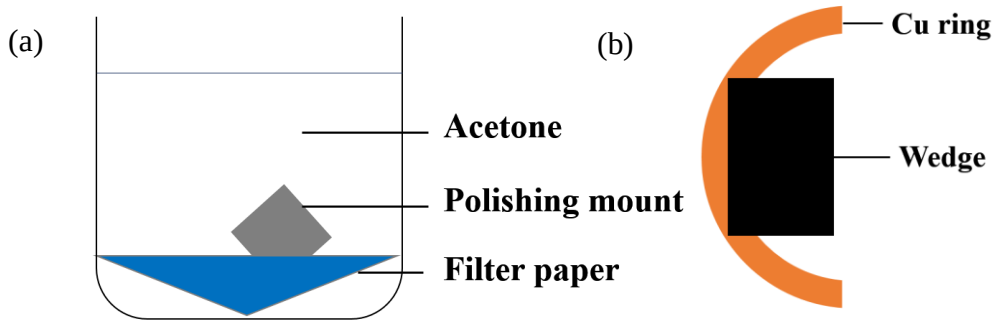

Figure 3.9 Sample collecting and mounting of the prepared wedge samples. (a) Collecting detached sample in acetone using folded filter paper; (b) illustration of how the prepared wedge sample is glued onto the half Cu ring for further TEM observation.

To make the wedge sample compatible with the TEM holder, an additional fixture needs to be attached to the wedge sample. Φ3 copper ring with a central hole is cut into half, epoxy glue is then used to mount the prepared wedge sample to the half ring as illustrated in Figure 3.9 (b). The mounted sample is stored in a vacuum chamber to prevent oxidation and wait for the epoxy glue to solidify. Once the glue is fully solidified, the wedge sample is now ready to be directly used for TEM observation.

3.2.2 Experimental Design for Studying the Deformation Mechanisms of Intermediate-sized Nano-crystalline

Mg-Gd (2 wt.%) wedge TEM samples prepared using the direct mechanical polishing approach described above are used in the current study. Prior to any TEM observation, plasma-cleaning using argon for 5 min was conducted to clean the sample of possible contamination.

The in-situ TEM nano-indentation tests were conducted on a Hysitron PI95 picoindenter equipped with a Berkovich tip, under load-control mode with a loading rate of 0.1 uN/s. The holder and tip used in the current study are shown in Figure 3.10 (a, b). The as-prepared wedge TEM samples are directly attached to the sample mount using superglue which will then be mounted to the holder for further indentation test. An illustration of the sample mounting is shown in Figure 3.10 (c), note that the flat surface should be facing the mount to reduce any tilting of the sample, care should be

taken during mounting to avoid any superglue contamination on the wedge tip. It is also worth mentioning that the original mount thickness marked as red "t" in Figure 3.10 (c) is too thick for the TEM stage to bring the wedge samples into focus, thus the thickness has been reduced using manual polishing until the sample can be correctly focused. It is practically difficult to judge how far the thickness is from the acceptable value in TEM, so a try-and-error approach was used for the thickness reduction polishing. All TEM observation was carried out on an FEI Talos TEM operated at 200 kV.

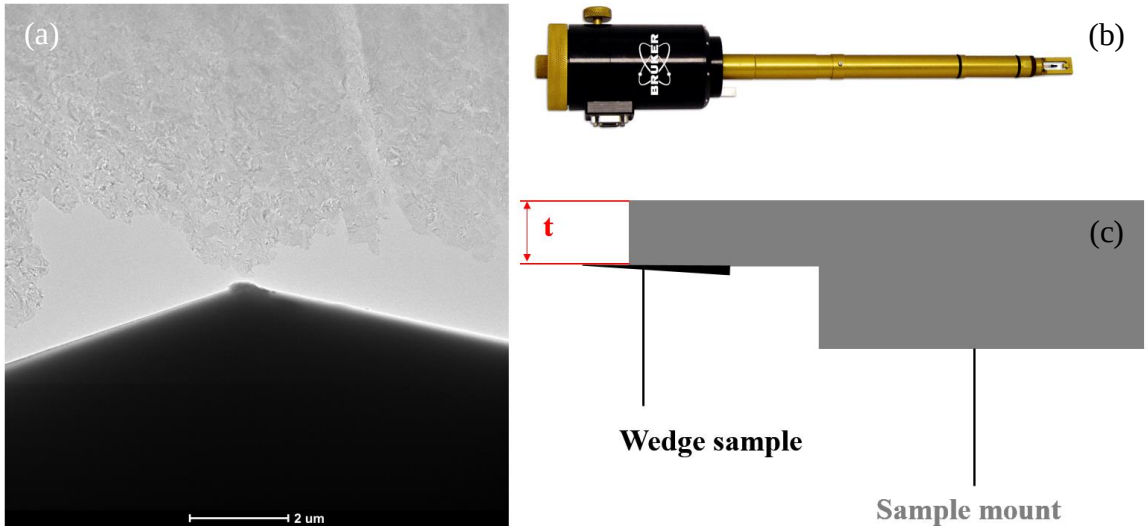

Figure 3.10 Instruments used in current in-situ nano-indentation. (a) A TEM image of the Berkovich indentation tip and (b) the Hysitron PI-95 picoindenter used in the current study; (c) side-view illustration of the sample mounting process.

As mentioned earlier, current characterization techniques all suffer from certain drawbacks in capturing the dynamic deformation process during in-situ TEM mechanical tests, HCDF is proposed for the first to be used to track the grain re-orientation in real-time during in-situ TEM nano-indentation. As a variation to conventional DF imaging, HCDF also selectively uses certain parts of diffraction by the insertion of an objective aperture to form the image. The main difference is that the incident beam is tilted away in HCDF imaging so that the interested diffraction is brought to the center of the optical axis, and by rotating the incident beam around, the whole diffraction ring can be brought into the collecting range of the objective aperture. Thus given that an exposure

time longer than the rotation period is used, the whole diffraction ring essentially contributes to the imaging, in contrast to a very limited portion of the ring contributed to imaging in conventional DF, making the HCDF imaging technique exceptionally powerful in the characterization of nano-crystalline materials. Because HCDF imaging is essentially based on Braggs' law of diffraction the same as conventional DF imaging, all traits belonging to conventional DF imaging like the direct orientation-contrast relationship should still hold, which will be further demonstrated using modified multi-slicing simulation later.

The schematic illustration of HCDF used in the current in-situ nano-indentation test is shown in Figure 3.11 (a). From the figure, it can be perceived that HCDF imaging is analogy to using an annular objective aperture. The speed of the beam rotation is set to 0.1 s for one complete circle, and the exposure time of HCDF is set to 0.2 s, longer exposure time yields a better signal-to-noise ratio thus improving image quality, but at the price of lower frame rates. It should be noted that the exposure time needs to be set to integer times of the beam circling period to minimize any potential artifact.

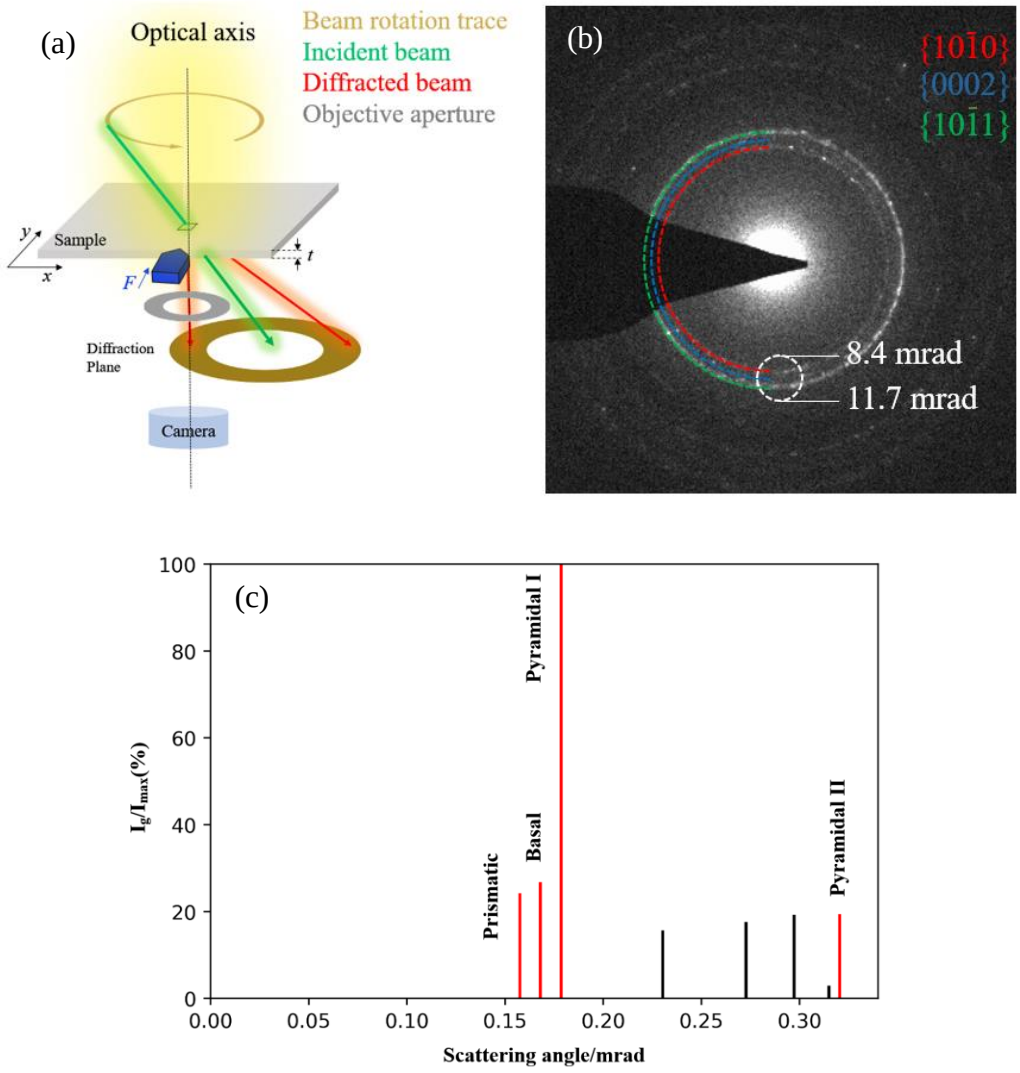

Figure 3.11 Experimental set-up for HCDF imaging combined with in-situ nano-indentation. (a) Schematic illustration of the HCDF implementation used in in-situ TEM nano-indentation test, the dark-blue arrow indicates the indenter tip; (b) SAED pattern of the nano-grains, the white dashed circle indicates where the objective aperture is inserted; (c) diffraction plot showing major diffractions of pure Mg, note the large gap between the pyramidal II and the three innermost reflections and multiple reflections that are not from any slip planes in between.

The objective aperture used in the current study yields an approximate collecting range of 8.4-11.7 mrad, as indicated by the white dashed circle in the selected-area electron diffraction (SAED) pattern shown in Figure 3.11 (b). Such collecting range allows tracking of three major slip planes, namely, basal {10$\bar{1}$0}, prismatic {0001}, and pyramidal I {10$\bar{1}$1} planes. As can be seen in the diffraction scattering angle plot shown in Figure 3.11 (c), if the pyramidal II planes were to be included, a much large aperture needs to be used, which not only includes unwanted information

from the non-slip planes in-between, but also deteriorates the image quality, as more inelastic electrons will be included, causing image blurring [140]. A specifically designed objective aperture with a nonconventional shape might solve this problem, but is beyond the scope of the current study, thus the pyramidal II $\{10\bar{2}2\}$ planes are not included. It should be noted that although <c+a> dislocations gliding on pyramidal II $\{10\bar{2}2\}$ planes have been reported [162] to actively contribute to the plastic deformation of Mg and its alloys, its CRSS is believed to be very close to that of pyramidal I planes [20], indicating their similar activity under the same loading condition. Therefore, although the orientation change of pyramidal II planes cannot be tracked under the current experimental setup, it is reasonable to assume similar behaviors to that of the tracked pyramidal I planes.

3.2.2.1 In-situ Technique: Nano-indentation (stress distributions)

The TEM observation region, which is thin enough to ensure electron transparency (i.e., a few hundred nanometers in thickness), is deemed under a plane stress condition since the indenter, with negligible changes in shape for a few hundred nanometers along the beam direction, applied load only along the sample plane. Our indenter has a Berkovich tip, which ideally is a three-sided pyramid with an apex angle of 142.3º. In reality, the indenter tip is always blunted, with a sphero-conical shape over a few hundred nanometers. Accordingly, the current experimental setting can be deemed as 2D indentation with a cylinder shape indenter. In order to consider the effects of a real Berkovich tip, 2D indentation using a wedge shape probe is also considered as the comparison for the case with cylinder shape indenters. The theoretical stress distribution is estimated according to Hertzman's contact theory (assume the elastic deformation) [163].

As illustrated in Figure 3.12 (a), a force F is applied to a cylindrical indenter with a radius R on a flat sample. The indentation depth δ, referring as the displacement, corresponds to a contact area of radius a. Therefore, the stress distribution under the indenter can be expressed using Equation 3.1.

$$\frac{\sigma_x}{P_{max}} = \frac{m}{a}\left\{1 + \frac{y^2 + n^2}{m^2 + n^2}\right\} + 2\frac{y}{a}$$

$$\frac{\sigma_y}{P_{max}} = -\frac{m}{a}\left\{1 - \frac{y^2 + n^2}{m^2 + n^2}\right\}$$

$$\frac{\tau_{xy}}{P_{max}} = \frac{n}{a}\left\{\frac{m^2 - y^2}{m^2 + n^2}\right\}$$

Equation 3.1 Equations describing the stress distribution around a cylindrical indenter with radius R [163].

In which,

$$m^2 = \frac{1}{2}\left\{\sqrt{(a^2 - x^2 + y^2)^2 + 4x^2y^2} + (a^2 - x^2 + y^2)\right\}$$

$$n^2 = \frac{1}{2}\left\{\sqrt{(a^2 - x^2 + y^2)^2 + 4x^2y^2} - (a^2 - x^2 + y^2)\right\}$$

$$a = 2\sqrt{\frac{FR}{\pi tE}}$$

$$P_{max} = \frac{2F}{\pi ta} = \sqrt{\frac{FE}{\pi tR}}$$

As we assume plane stress condition, the effective Young's Modulus can be calculated using Equation 3.2 [163]:

$$\frac{1}{E} = \frac{1}{E_{indenter}} + \frac{1}{E_{Mg}}$$

Equation 3.2 Equation used to calculate the effective Young's Modulus from Young's Modulus of the indenter and Mg.

Accordingly, the max shear stress distribution can be estimated from Equation 3.3 [163]:

$$\tau_{max} = \sqrt{{\tau_{xy}}^2 + \left(\frac{\sigma_x - \sigma_y}{2}\right)^2}$$

Equation 3.3 Equation used to estimate the maximum shear stress distribution.

and is plotted in Figure 3.12 (b). The max shear stress is ~0.3P_{max} *at* a depth of ~0.78a.

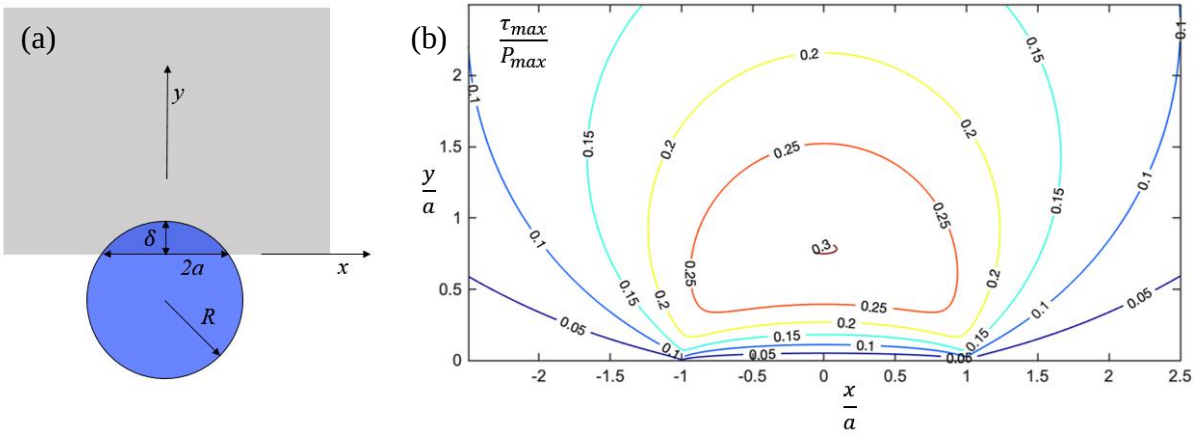

Figure 3.12 Stress distribution estimation of the conical tip case. (a) Schematic illustration of the conical tip indenter and (b) the corresponding calculated stress distribution.

In the case of wedge indenter, the max shear stress occurs along the y-axis. At the apex of the indenter, the pressure is infinite however the principal shear stress is finite. The plot comparing the principle shear stress of cylindrical indenter and wedge indenter is shown in Figure 3.13.

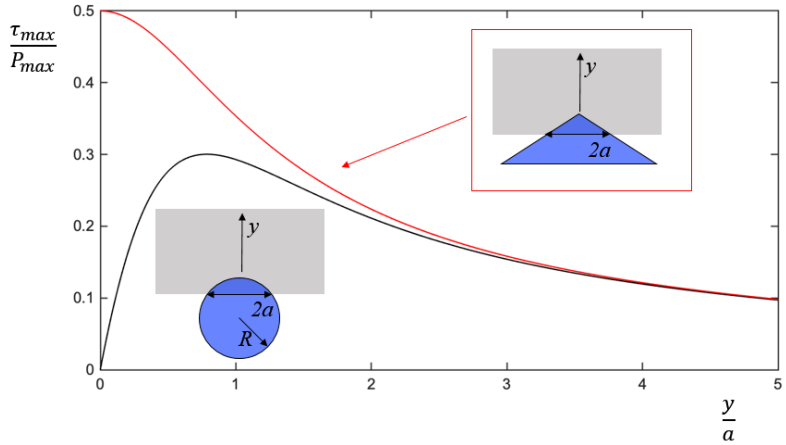

Figure 3.13 Comparison between the shear stress distributions along the y-axis of conical (black line) and wedge shaped (red line) indenter tip.

3.2.2.2 Thickness measurement

The contrast we see in low-magnification TEM micrograph rises from two major sources: mass-thickness contrast (attenuation due to incoherent elastic scattering--Rutherford scattering) and diffraction contrast (coherent elastic scattering – Bragg diffraction) [138]. When crystals are not orientated along zone axes, the contribution from diffraction contrast decreases, and the images can be approximately treated as a mapping of its mass-thickness distribution. In the case of homogeneous materials where density remains unchanged throughout samples (as in the current case), it means the contrast we see in the image is directly linked to the thickness of the samples given no strong Bragg's diffraction is activated. Such relationships can be described using Equation 3.4, where C is the image contrast, I_0 is the intensity of electrons measured at the empty area (without any specimen), I_{tr} is the intensity of transmitted electrons measured after going through the specimen, k the proportional factor, Z and A the atomic number and atomic weight of the components, respectively [164], the exponential coefficient x varies with accelerating voltage. Detailed procedures for thickness measurement using mass-thickness contrast have been elaborated by Pozsgai [164]. Given the same accelerating voltage and similar TEM illumination conditions are used, the equation obtained by Pozsgai [164] as shown in Equation 3.5 has been adopted for the thickness measurement of the wedge sample. All images for thickness measurement were taken without any objective aperture to minimize the influence of diffraction contrast.

$$C = log_{10}(\frac{I_0}{I_{tr}}) = k\rho t\frac{Z^x}{A}$$

Equation 3.4 Equation describing the mass-thickness contrast in TEM [164].

$$C = log_{10}(\frac{I_0}{I_{tr}}) = \frac{1.44*10^{-4}log_{10}^{e}\rho tZ^{1.96}}{A}$$

Equation 3.5 Mass-thickness contrast equation obtained experimentally by Pozsgai [164] for accelerating voltage of 200 kV.

3.2.2.3 HCDF Contrast Simulation Using Modified Multi-slicing Algorithm

Although HCDF is not a new technique, it was mostly used for measuring grain size, characterizing dislocations, etc. in previous research [138-140]. While HCDF is proposed to track the orientation change of slip planes in the current study, there is yet to be any detailed contrast-orientation study of HCDF. Thus to clarify such uncertainty, a self-modified multi-slicing algorithm has been used to simulate the contrast of HCDF images along multiple different crystallographic axes. The original multi-slicing code written by Kirkland [165] is an algorithm essentially simulating the transmission process of electrons through thin foils inside TEM. The key idea of this model is to slice the thin foil into atomic layers along the beam transmission direction (z-direction) as shown in Figure 3.14 (a). The multi-slicing algorithm simplifies three-dimensional electron-matter interaction as the propagation of two-dimensional interaction within each atomic layer over the sample thickness. The transmission process of the incident electrons through the sample can be divided into two parts: the transmitting part at the slicing layers marked by the horizontal black lines and the propagating part through the vacuum between individual layers, if the slicing is done such that the position of atoms in sample coincides with the slicing layers, very accurate simulation results can be obtained.

To make the multi-slicing algorithm compatible with HCDF imaging, a virtual objective aperture allowing conical illumination conditions is needed. In the original code, the insertion of the virtual objective aperture is done by letting only electrons with scattering angle $\theta<x$ (x being the diameter of the central hole in the objective aperture) contribute to the imaging process. As mentioned earlier, the HCDF imaging achieved by tilting and rotating the beam is equivalent to using an annular objective aperture, thus the HCDF imaging can be simulated by adding an inner limitation of allowed electrons, namely, changing $\theta<x$ to $y<\theta<x$ as the new criteria for electrons contributing to the imaging process, where y is the inner radius of the annular aperture, a visualization of how the modified code works in HCDF mode is shown in Figure 3.14 (b).

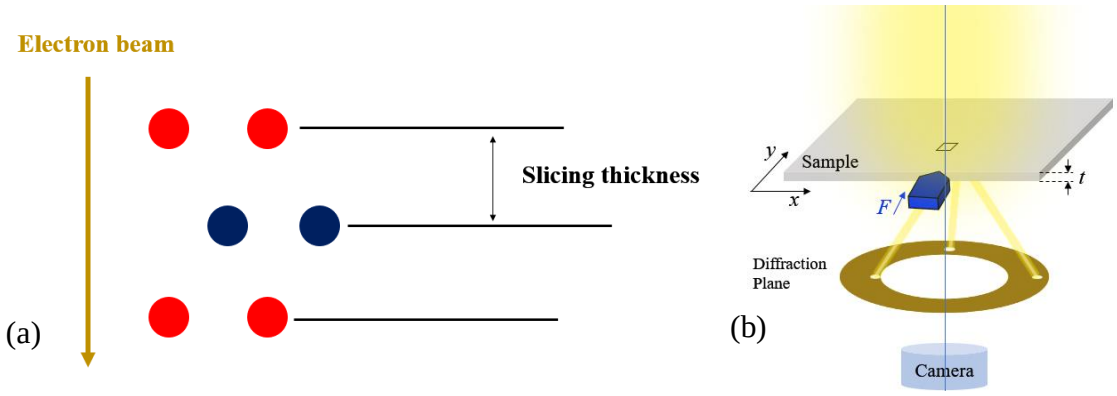

Figure 3.14 Principle of multi-slicing model for HCDF imaging. (a) Illustration of the transmission process of the incident beam in multi-slicing model, red and dark-blue circles represent atoms located at different layers in the sample; (b) visualization of the annular collector used in the modified multi-slicing algorithm.

Due to dynamic scattering effects, the intensities of both incident beam and diffracted beams oscillate periodically, a common example being the thickness fringes found in BF and DF images near the edge where thickness gradient exists [138]. Similar oscillation is expected in HCDF imaging, so along with simulation for different zone axes, simulation for the same zone axis but with different sample thickness is also required. Considering the fact that simulation program can only manually input each simulation parameter, an overwhelming amount of time and effort are needed if the job was to be handled manually. To make matters worse, each simulation requires an individual atomic model as input, creating them manually is also daunting, to say the least. To reduce the overwhelming task to an acceptable level, a series of automation scripts written in Python have been created so that most work can be done automatically by the computer itself, the detailed process will be introduced in the following.

The multi-slicing algorithm only accepts input with Cartesian coordinates, thus instead of hexagonal lattice coordinates, an orthogonal unit-cell of Mg needs to be used. A base-centered orthogonal unit-cell can be extracted out of the hexagonal lattice [138], as can be seen in Figure 3.15 (a, b). To transform between two unit-cell coordinates, one needs to know the relationship between the three base vectors of two unit-cell. The c-axis ([0001]-direction) is essentially the same for the two unit-cells, the relationship for the other two axes is shown in Figure 3.15 (c). Thus the

relationship between two unit-cell can be mathematically described by three linear equations shown in Equation 3.6 from which the transformation matrix B can be obtained as shown in Equation 3.7. It should be noted pure Mg is used in the current simulation for simplification as minor alloying of Gd in the current case is unlikely to drastically change the image contrast.

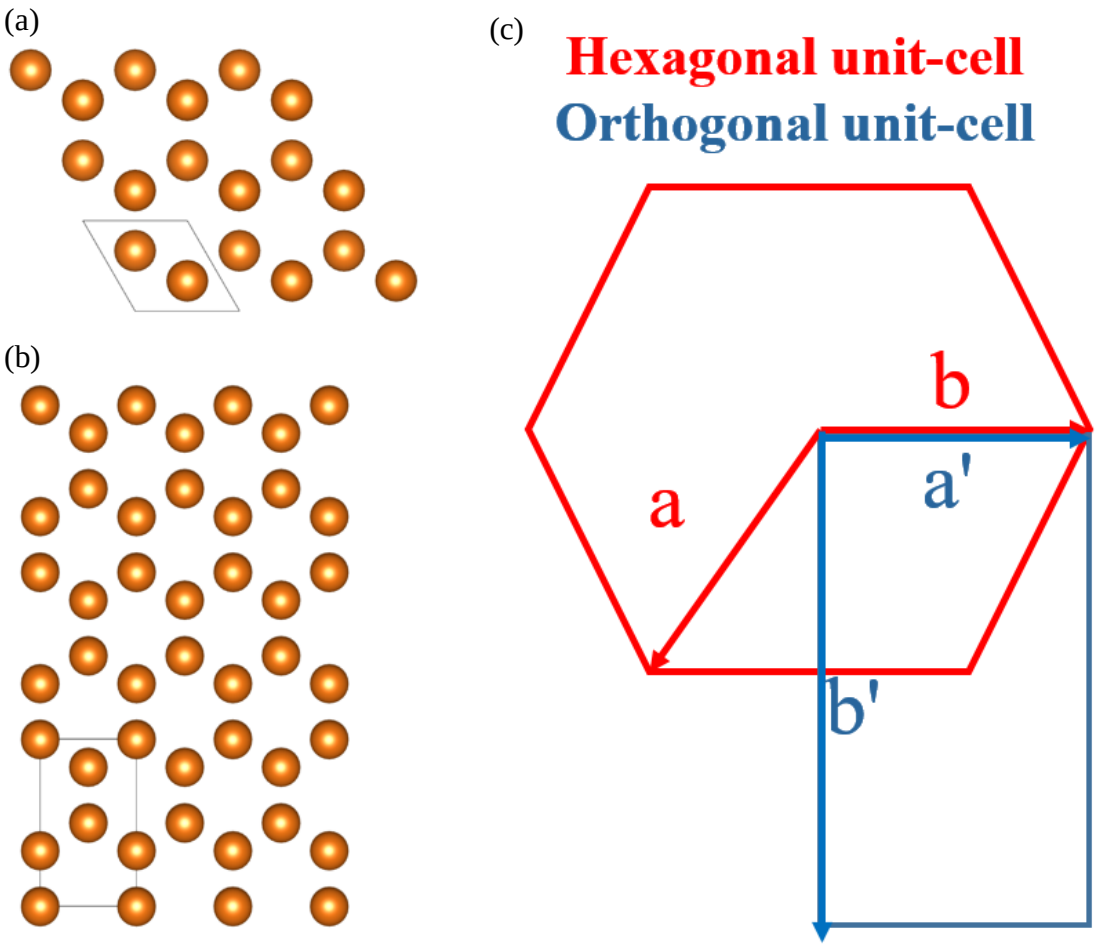

Figure 3.15 Mg unit-cells in hexagonal and orthogonal coordinates viewed along [0001] for multi-slicing simulation. Schematic illustration showing the (a) hexagonal unit-cell and (b) the base-centered unit-cell, uni-cells are multiplied for better visualization; (c) relationship between base vectors of hexagonal and orthogonal unit-cell of Mg.

$$a=-0.5*a'+0.5*b'+0*c'$$
$$b=1*a'+0*b'+0*c'$$
$$c=0*a'+0*b'+1*c'$$

Equation 3.6 Linear equations connecting the base vectors of hexagonal unit-cell (abc) and the orthogonal unit-cell (a'b'c')

$$B=\begin{bmatrix} -0.5 & 0.5 & 0 \\ 1 & 0 & 0 \\ 0 & 0 & 1 \end{bmatrix}$$

$$hkl_{hex}^{T} = B * HKL_{orth}^{T}$$

$$uvw_{hex}^{T} = [B^{T}]^{-1} * UVW_{orth}^{T}$$

Equation 3.7 The transformation matrix B connecting the hexagonal cell to the orthogonal cell, and the corresponding transformation equation for plane index (hkl) and vector index (uvw) [166].

To simplify the simulation process, all crystallographic indices used for calculation is based on the orthogonal coordinates except the output after finishing all the simulation. The calculated orientations are generated by letting each index in <*uvw*> iterate from 0 to 4 ([000] is excluded), yielding a total of 124 directions. However, due to the symmetry of hexagonal crystals, most of them are crystallographically identical and give essentially the same simulation results. The multi-slicing algorithm is computationally intensive, these redundant works are removed based on symmetry before any real simulation starts.

After all zone axis indices are generated, super-cells of each direction need to be created to be used as the input atomic structure of the multi-slicing algorithm. The multi-slicing code uses discrete fast Fourier transformation (DFFT) to increase the calculation efficiency, consequently, a so-called "wrap around" phenomenon occurs, meaning the left-and-right or top-and-bottom edges effectively touch each other causing potential artifacts in the image. To reduce such artifacts, a periodical boundary condition is required for the super-cell used for simulation [165]. Because the multi-slicing code always uses the z-axis as the incident beam direction, a new "unit-cell" needs to be found based on crystals rotated to a given zone axis, in order to meet the periodical boundary condition criteria. There are few existing software like "Cartesian" [167], however, while the

software gives the correct unit-cell for some low-index zone axes, it fails to find the correct unit-cell for high-index zone axes which are also essential in the current study. To solve this problem, a new program called "Super-cell" has been written by the author, the flow chart explaining how the program works is shown in Figure 3.16 (a). Starting with the original unit-cell of Mg, the *a*, *b*, *c* of the new unit-cell are initialized as all 0; then checking on the product of *a*, *b*, *c* will be applied, if it doesn't equal to 0, meaning *a*, *b*, *c* have all been found, then the program outputs the new unit-cell and lattice parameters, which will be used to generate series of supercells with different thicknesses for further multi-slicing simulations. If the value of $a \times b \times c$ equals 0, meaning at least one of them has not been found yet (box too small to find). The unit-cell then gets expanded 3 times along *x*, *y*, and *z* directions and rotated to a given zone axis whose algorithm will be described shortly in the following part. Next, a searching algorithm based on the translational symmetry of crystals is used to find possible *a*, *b*, and *c* in the expanded super-cell. An example of how lattice parameter *a* of the new cell is found for zone axis [0001] is shown in Figure 3.16 (b). It should be noted that all computer uses limited precision for float number, causing inevitable round-off error during each calculation, thus a small tolerance is used during the searching. The run time of this program scales with atom numbers in the simulation box which increases to $3 \times 3 \times 3 = 27$ times for each expansion, for some high-order zone axis which has extremely large unit-cell parameters, the computer used for simulation could run out of memory before finding every *a*, *b*, and *c*, thus a maximum value of 40 Å is set for the simulation box beyond which the program simply use 40 Å as the unfound parameters to generate the super-cell. Another reason for choosing such cut-off is related to the run-time of the simulation algorithm itself. For a simulation box with non-periodical boundary conditions, a simulation box as large as possible is good in terms of reducing the "wrap around" error. However, due to the intensive computation power needed for multi-slicing simulation, an extremely big simulation box too quickly drains out the computer, resulting in unacceptable calculating time, thus a cut-off of 40 Å is chosen as a compromise between accuracy and running time based on the currently available computation resources which is a personal

computer. Larger unit-cell with truly periodical boundary condition can be used, thus yielding higher precision, given computer with higher computational power was used.

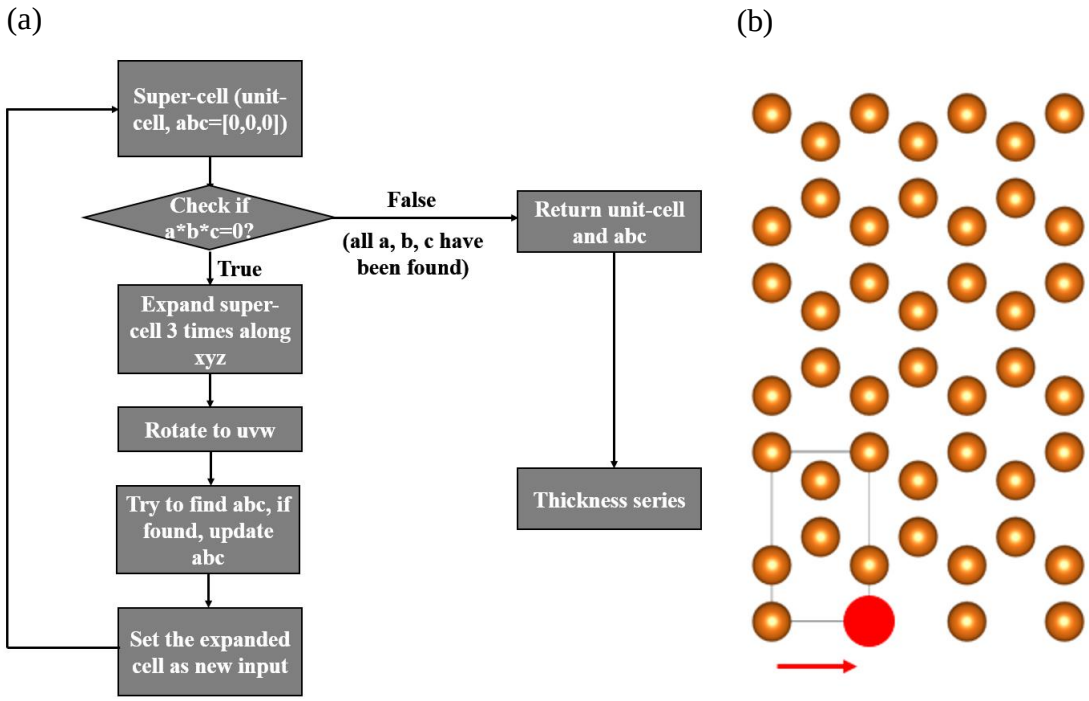

Figure 3.16 Finding simulation boxes under given crystallographic axes. (a) Flow chart for the program "Super-cell" responsible for creating unit-cells for any given orientation; (b) example showing how to find the lattice parameter a of new crystal rotated to [0001], a search is conducted in x-y plane along the x-direction, the distance between the atom at origin and the next repeating atom (red) is considered as the new lattice parameter along the x-direction (a), similarly, b and c can be found given large enough super-cell.

Similar to the transformation matrix used to transfer plane/vector indices between hexagonal and orthogonal unit-cell, the coordinates of crystal rotated to any specific zone axis can be related using a rotation matrix *R* which is given by the angles between the old and new coordinates axis [166], as shown in Figure 3.17.

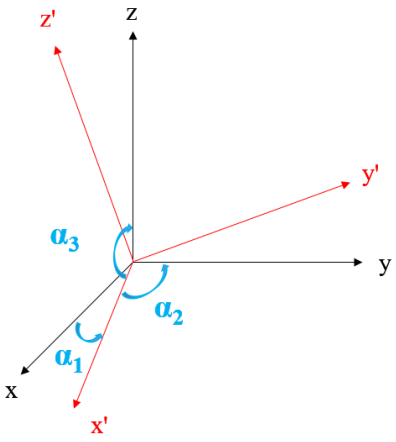

$$R = \begin{bmatrix} \cos\alpha_1 & \cos\alpha_2 & \cos\alpha_3 \\ \cos\beta_1 & \cos\beta_2 & \cos\beta_3 \\ \cos\gamma_1 & \cos\gamma_2 & \cos\gamma_3 \end{bmatrix}$$

$$A_{original} = R \times A_{rotated}$$

Figure 3.17 Rotation matrix R connecting the rotated and original crystals. The original and rotated coordinates are in black and red, respectively; angles α1, α2, and α3, etc. represent the angles between the rotated x' axis and the original x, y and z-axis, etc., and are visualized in the figure as light blue as examples.

One may have noticed that only one axis is fixed by a given orientation to which the crystal rotates, to finalize the rotation, another base vector pointing to the horizontal direction is needed which needs to be chosen for each zone axis. An easy way to find this vector is by the help of a simulated diffraction pattern. By definition, any g vector (*hkl*) (or say reciprocal vector) in the diffraction pattern of a zone axis is perpendicular to the zone axis [*uvw*] itself. Thus if we use these two vectors as the base vectors of the rotated coordinates, due to the orthogonality of Cartesian coordinates, another base vector can be then automatically calculated accordingly. It should be noted that the g vector is a reciprocal space vector while the zone axis is a real space vector, transformation between these two spaces is needed. The corresponding transformation matrix G is shown in Equation 3.8.

$$uvw^T = G^{-1} \times hkl^T$$

$$G^{-1} = \begin{bmatrix} a^*a^* & a^*b^* & a^*c^* \\ b^*a^* & b^*b^* & b^*c^* \\ c^*a^* & c^*b^* & c^*c^* \end{bmatrix}$$

Equation 3.8 Transformation matrix G connecting real space vector [uvw] and reciprocal vector (hkl), [166] where a^*, b^*, c^* represents the lattice parameters of the reciprocal lattice.

The validity of the "Super-cell" program can be demonstrated by the comparison shown in Figure 3.18 (a-c). It can be clearly seen from the figures that the new unit-cell generated by the "Super-

cell" program correctly reproduces the minimal periodicity of the crystal along the [110] axis, while the "Cartesian" program gives a non-primitive unit-cell with redundant atoms.

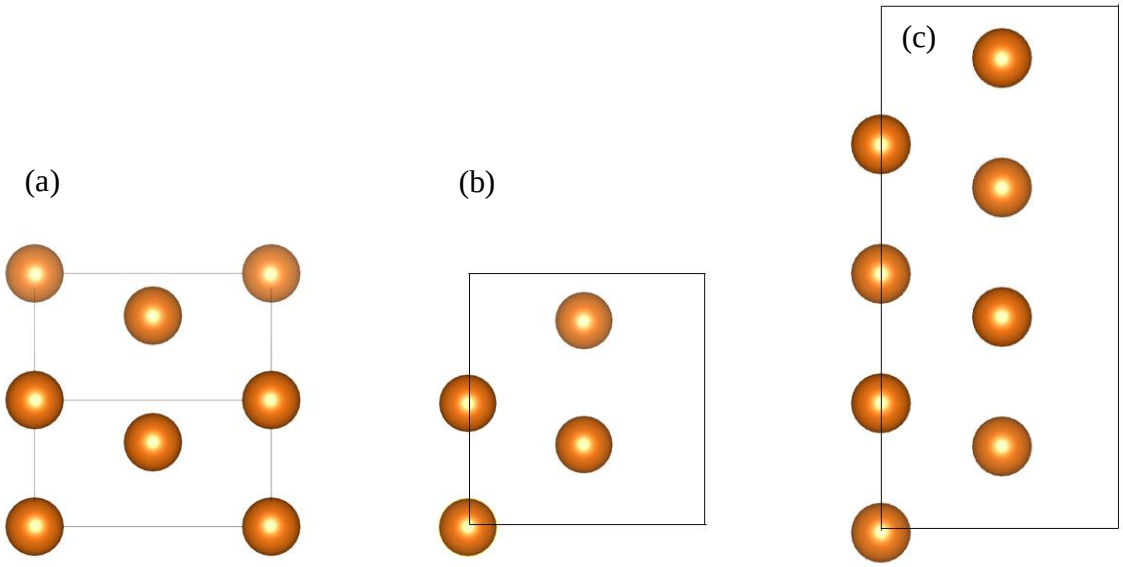

Figure 3.18 Comparison between "Super-cell" and "Cartesian". (a) Original orthogonal unit-cell viewed along [110], note atoms at four corners have the same height (z-value); (b) [110] unit-cell generated by "Super-cell" and [110] unit-cell generated by "Cartesian" [167].

Once all the simulation boxes are created using the above-mentioned "Super-cell" program, another script named "ShellFile" is used to generate a Linux shell script named "Autorun.sh", which contains all command lines needed to run simulations over all simulation boxes. Upon running, the "Autorun.sh" program automatically completes all the simulations and outputs series of simulated HRTEM images calculated under different zone axes and sample thicknesses which will be used for further analysis, for each zone-axis and sample thickness, both DF and BF images are calculated for consistency check. It is worth mentioning that due to the small size of the simulation boxes (maximum 4 nm* 4 nm), the area of any simulated HRTEM image is comparable to or smaller than the size of one pixel in experimental HCDF images captured in the current study, thus it is only reasonable to use the intensity averaged over entire simulated image to represent the HCDF intensity. Additionally, to make all images directly comparable, all averaged intensity is normalized based on the intensity of the direct beam, similar to what has been used in the quantification of

HAADF images [168-170]. Thus the complete flow chart of the simulation can be summarized by the plot shown in Figure 3.19, starting with an orthogonal Mg unit-cell, simulation boxes with different orientations and sample thicknesses are automatically generated by "Super-cell", based on which a Linux shell file "Autorun.sh" is generated by "ShellFile". As mentioned earlier, running "Autorun.sh" automatically inputs all the simulation boxes into the "Multi-slicing" simulation program for image calculation.

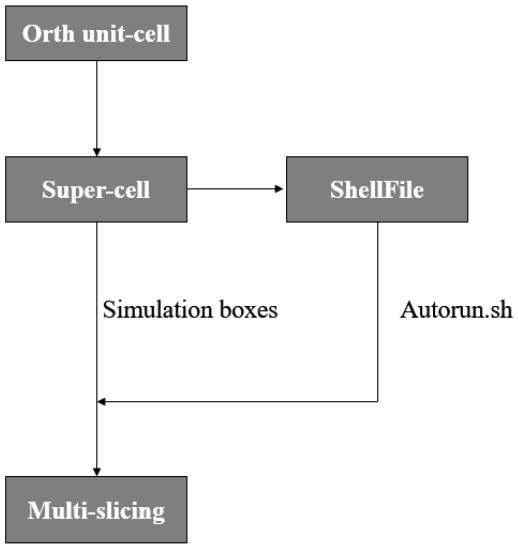

Figure 3.19 Simulation flow chart for the HCDF image simulation

3.3 Experimental Set-up for Tailoring Dislocations via Hot Compression

In order to introduce the desired dislocation structure, uniaxial hot-compression tests were conducted on the rectangular pure Mg samples at elevated temperatures (400 ^{o}C) along their long axis until fracture. To preserve the microstructures obtained during hot-compression to room temperature, an immediate water quenching was done on all samples after the deformation.

TEM can directly visualize defects like dislocations due to their strain field which causes differences in Braggs' condition, resulting in contrast differences around defects [138]. With the help of double-tilt holders, TEM is also capable of viewing samples along different crystal zone axis, which can be essential to the study of dislocations. To prepare the thin film needed for TEM

observation, the as-quenched samples were first cut into thin slices 0.5 mm in thickness using wire cutting, such that their surface normal either parallel or perpendicular to the compression direction. This cutting strategy is to ensure wider coverage of orientation during TEM observation since the tilting angle of the double-tilt holder is limited. Pre-thinning of these slices was carried out using series of sandpapers until the thickness was reduced to ~0.12 mm. Disks of 3 mm in diameter were then punched out of these pre-thinned slices for the final thinning. The final thinning was done using a twin-jet polishing machine with a mixed solution comprised of 10 vol. % perchloric acid and 90 vol. % ethanol. All TEM characterization was conducted on a JEOL 2100F TEM operated at 200 kV. The ellipticity map of HRTEM images was created using an open-sourced Python library called "Atomap" [171].

Atomic models of dislocation arrays used for diffraction simulation were built by periodically inserting <c>-screw dislocations with alternating signs, forming a hexagonal pattern with an inter-spacing of ~7 nm within a perfect Mg lattice, consistent with the experimental observation. A part of this model is illustrated in Figure 3.20. The inserted dislocations are pure screw dislocations with Burgers vectors either <c> or <-c>. The whole simulation box has the dimensions of 81 nm*81 nm*1.0 nm in the $[11\bar{2}0]$ direction (x-axis), the $[10\bar{1}0]$ direction (y-axis) and [0001] direction (z-axis), respectively. An empirical potential developed by Liu et al. [172] was chosen to apply additional structural relaxation to the model. Corresponding diffraction pattern simulation was conducted using an algorithm proposed by Coleman et al. [173], which includes the effects of atomic displacement on the diffraction patterns.

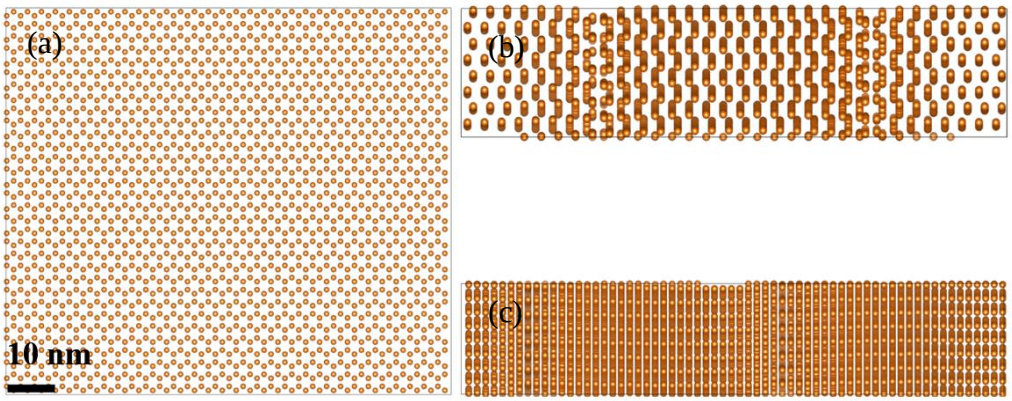

Figure 3.20 Part of the atomic model used for diffraction simulation viewed along (a) [0001], (b) [$10\bar{1}0$] and (c) [$11\bar{2}0$].

Chapter 4 Results: Nano-crystalline Mg-Gd Alloys Synthesis

4.1 Microstructure of the Synthesized Nano-crystalline

As can be seen in the BF image shown in Figure 4.1 (a), contrary to the coarse-grained microstructure observed in EBSD and twin-jet polished samples, multiple nano-grains with size ~100 nm can be clearly identified in the micrograph, the corresponding SAED pattern shown in Figure 4.1 (b) also exhibits characteristic ring-feature of diffraction from polycrystalline materials. Both image and diffraction indicate the presence of prevailing nano-grains, which is totally unexpected for such samples subjected to high-temperature solid solution treatment. As such high temperature treatment is known to cause recrystallization and grain growth, resulting in coarse-grained microstructure [174], usually over micron scale. Additionally, these nano-grains are not confined to specific areas but distributed almost homogeneously in all observable area near the sample edge, as shown in Figure 4.1 (c), and judging by their continuous diffraction ring patterns showing uniform intensity distribution, most areas possess a rather uniform orientation distribution without strong texture. It is worth mentioning that no twinning is detected in any of the nano-crystalline wedge samples, the possible reason will be discussed in the following part regarding the formation of these nano-crystalline.

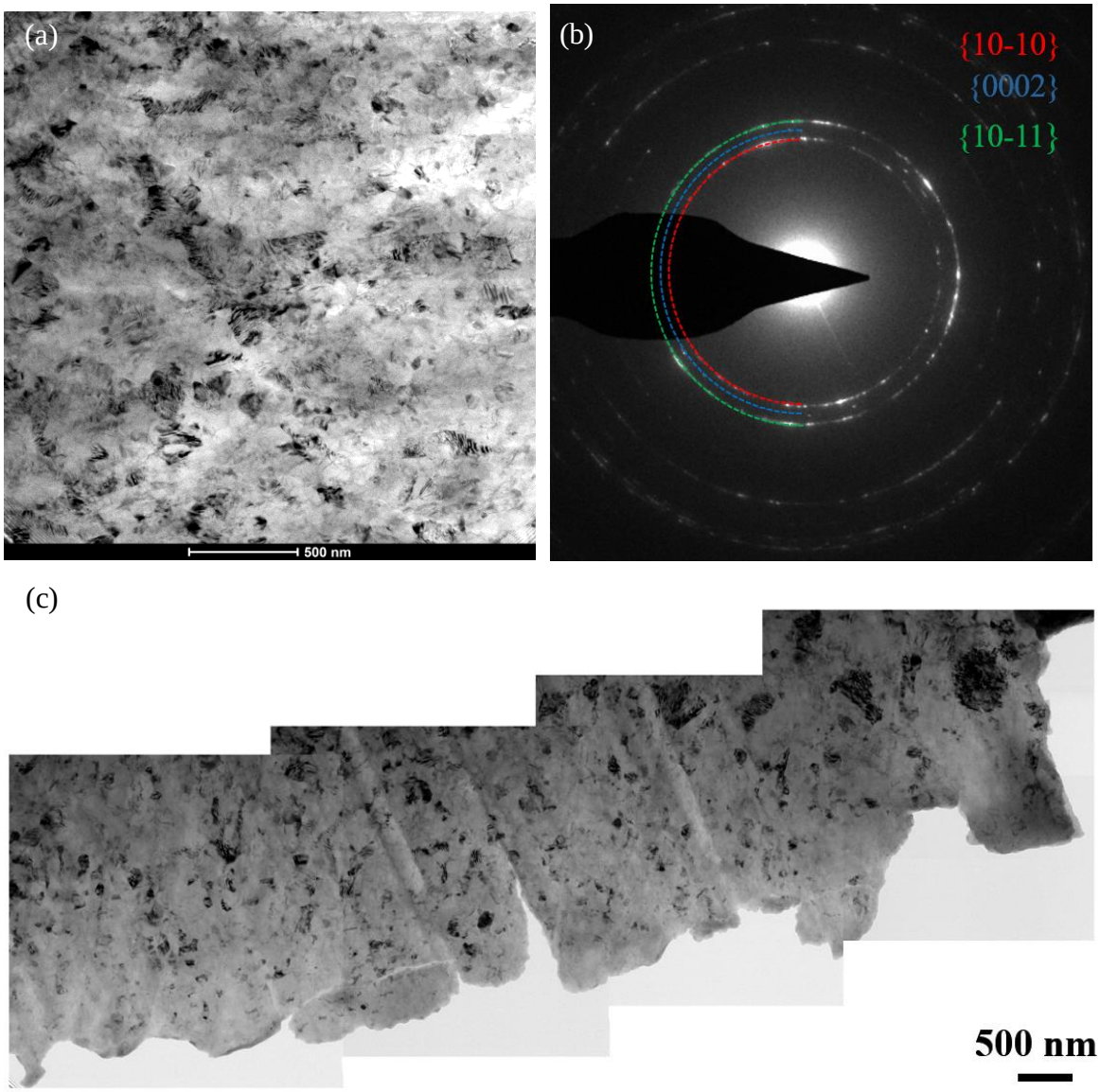

Figure 4.1 Typical TEM micrograph of the wedge TEM samples. (a)BF image and (b) corresponding SAED pattern of the wedge TEM sample prepared by direct mechanical polishing, showing diffraction rings belonging to Mg; both images indicate that the microstructure is comprised of numerous nano-grains; (c) stitched image

Though judging from solid solution treatment parameters used in previous refs on Mg-RE alloys [9, 10, 175], the temperature and duration in the current study should be enough to eliminate significant inhomogeneity considering only 2 wt.% Gd is added into the system. To exclude the possibility that these nano-crystalline are results of microstructural inhomogeneity, multiple wedge samples taken from different locations of the raw ingot were prepared using the same preparation

procedure described earlier, corresponding BF images and SAED patterns are shown in Figure 4.2 (a-d), all show similar microstructure comprised of nano-crystalline Mg.

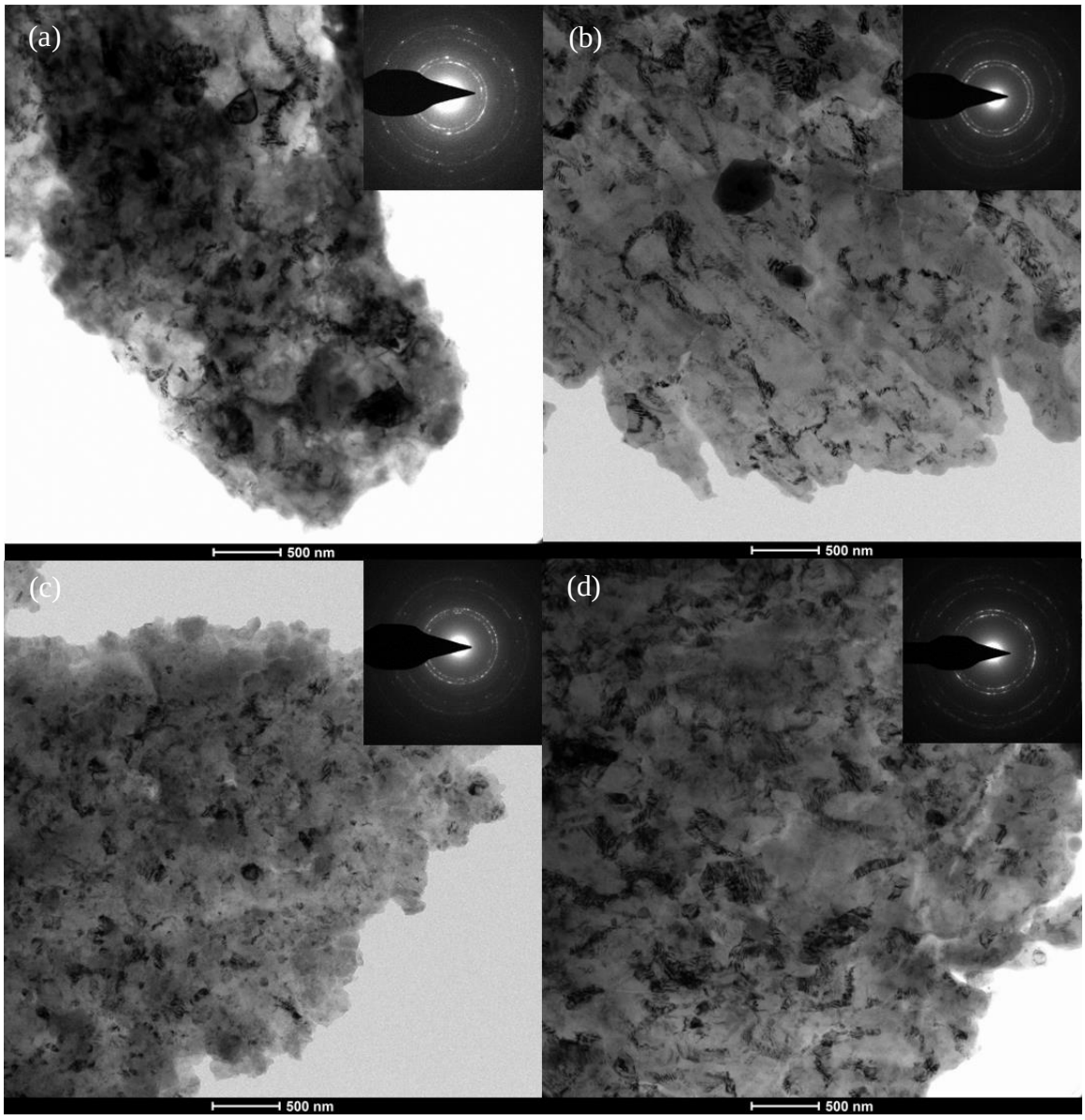

Figure 4.2 TEM-BF images and SAED patterns of nano-crystalline from various positions. (a-d) BF images and corresponding SAED patterns of wedge TEM samples taken from different locations of the raw ingot. All show nano-crystalline microstructure similar to that of the solid-solution treated samples.

In addition, similar wedge samples have been prepared using all hot compressed with different compression rates, as shown in Figure 4.3 (a-d), despite their different deformation history, all wedge samples show nano-crystalline structures similar to that of the undeformed solid-solution

treated samples. The similarity between these wedge samples indicates a likely common origin of the nano-grains: the mechanical polishing process. Only two mutual preparation processes, solid-solution treatment and wedge sample polishing, are shared by all these samples. The high-temperature solid-solution treatment is highly unlike to produce such fine grains, leaving the only possibility to the polishing process which will be discussed later in this chapter.

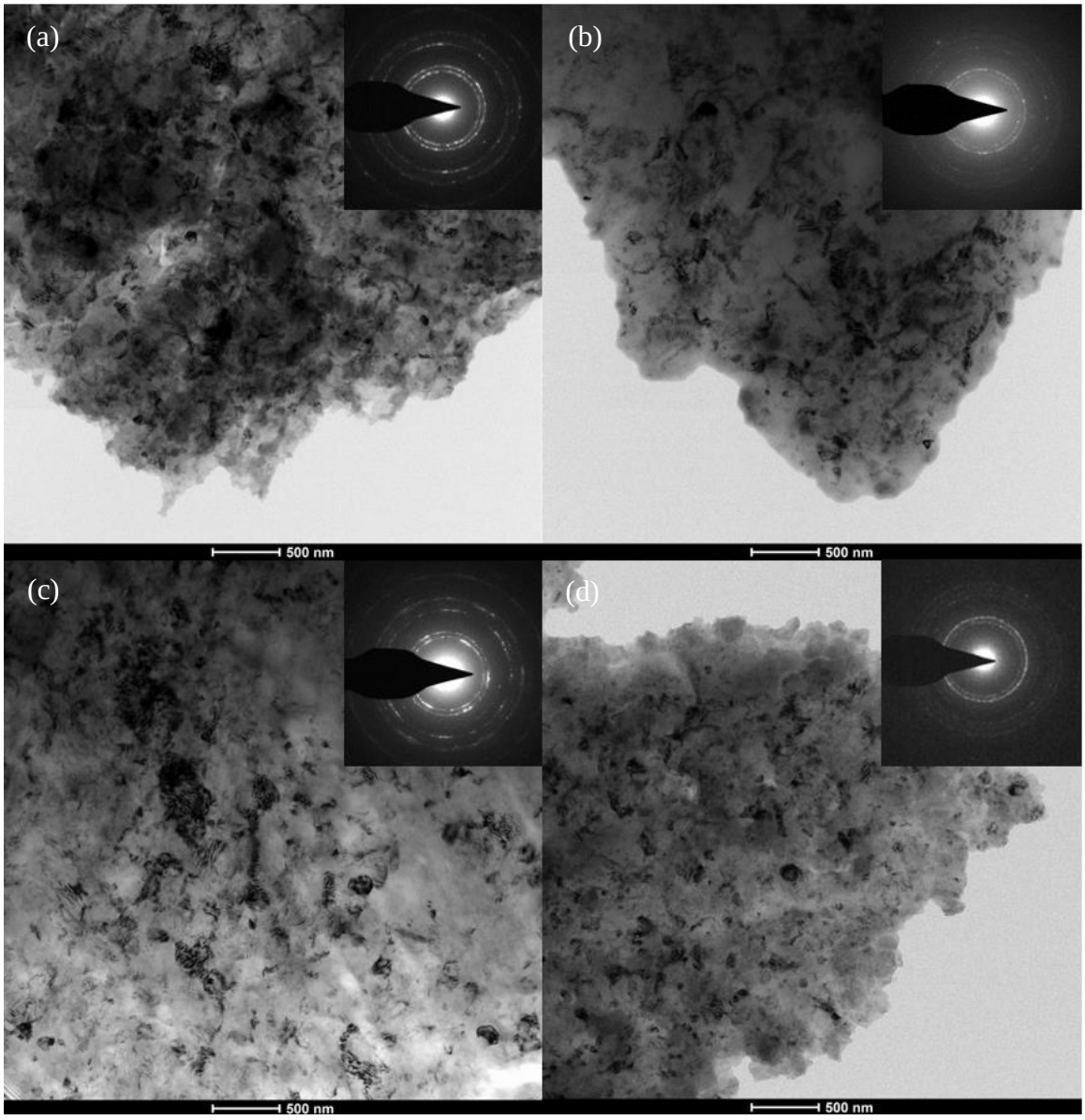

Figure 4.3 TEM-BF images and SAED patterns of nano-crystalline from samples subjected to different compression rates. (a-d) BF images and corresponding SAED patterns taken from samples subjected to 400 °C hot-compression with compression rates of 0.5 mm/min, 5 mm/min, 20 mm/min, and 200 mm/min, respectively.

4.2 Grain size distribution and sample thickness

Considering all wedge samples show similar microstructure, the undeformed solid-solution treated wedge samples were used to measure the average grain size of the nano-crystalline wedge samples. As can be seen in Figure 4.4 (a), it is hard to distinguish some grain boundaries in the BF image. So instead of using BF for grain size measurement, HCDF imaging is used for better accuracy [138, 140]. The three innermost diffraction rings showing strongest intensity ({0001}, $\{10\bar{1}0\}$ and $\{10\bar{1}1\}$) are used in current study, the corresponding HCDF images is exhibited in Figure 4.4 (b). It can be seen that compared to blurred grain boundaries in the BF image, many grain boundaries are showing higher contrast in the HCDF image, making the grain size measurement easier and more reliable [140]. The intercept method [176] has been used on multiple HCDF images to give the grain size distribution graph shown in Figure 4.4 (c), the average grain size is calculated to be ~114 nm. It should be noted that even though HCDF is used to maximize the visibility of nano-grains, there are still areas where grain boundaries are hard to distinguish, for instance, the area enclosed by the red lines shown in Figure 4.4 (b). Such area is simply counted as one grain, however, tilting experiments reveal that the above-mentioned area may also contain multiple nano-grains once they are tilted to certain orientations, as will be discussed in detail in the next chapter where multiple grains become visible due to grain rotation during in-situ TEM nano-indentation. Therefore, the calculated average grain size shown here is likely slightly bigger than the actual value.

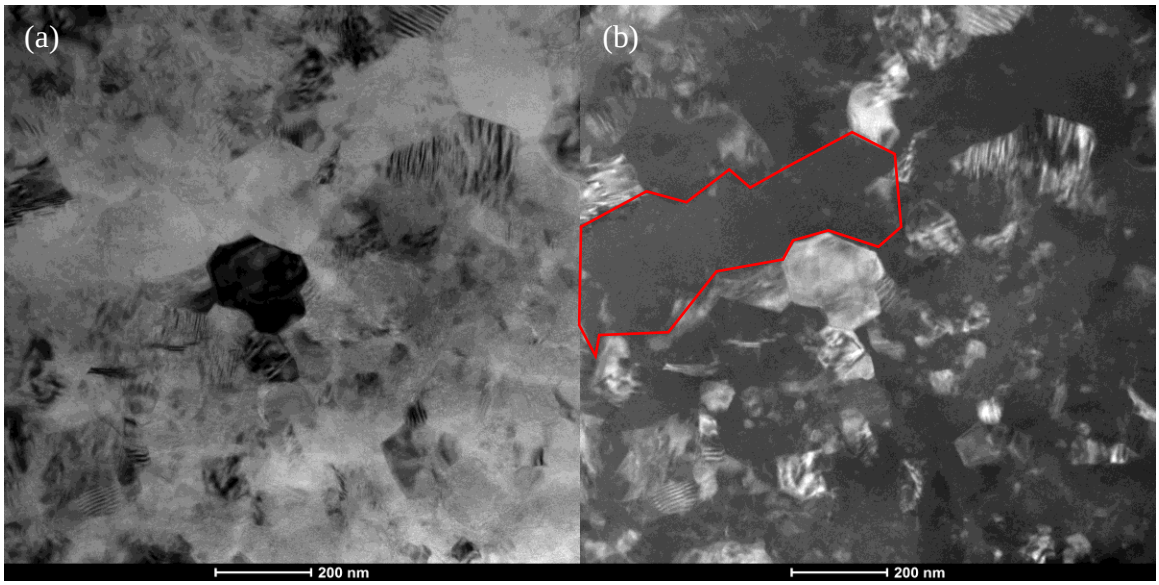

(c)

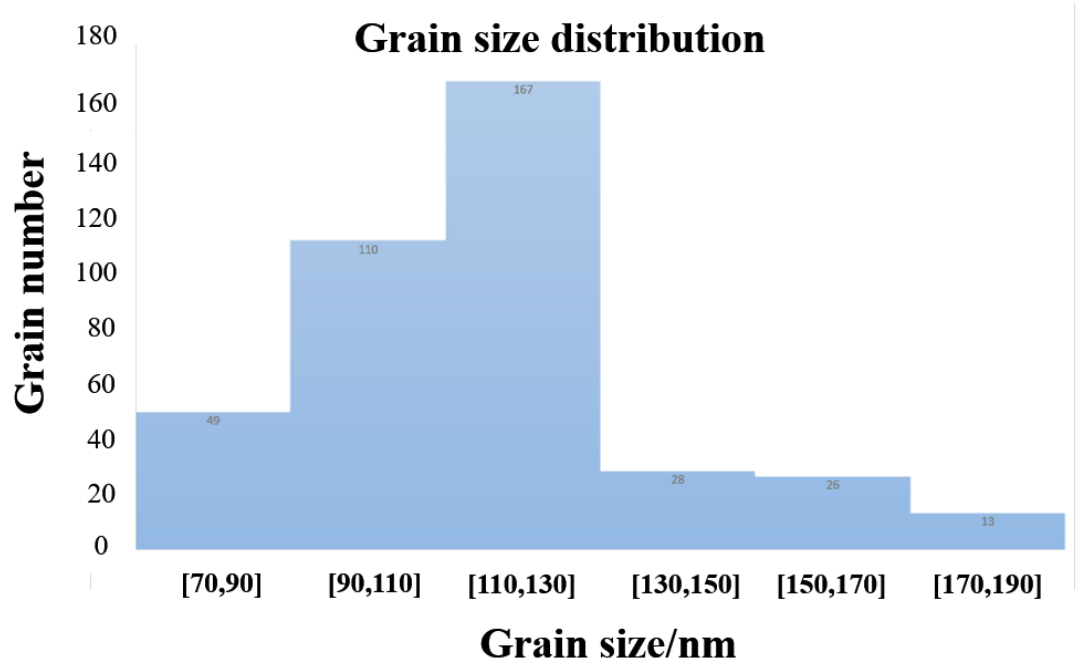

Figure 4.4 TEM characterization on the grain size distribution of the wedge samples. (a) BF and (b) HCDF images of the same area, note the higher visibility of grains in HCDF image; (c) size distribution of the wedge TEM sample made from solid-solution treated sample, values above each column correspond to grain numbers falling into such size range.

The sample thickness was calculated based on multiple TEM micrographs using Equation 3.5, all micrographs used for thickness measurement were taken without any objective aperture as indicated in ref. [164] to minimize errors caused by strong diffraction contrast. An example of the

thickness measurement is illustrated in Figure 4.5, from which shallow groves left by polishing (roughly along the black double-headed arrow) can be seen. Two areas indicated by blue and red lines (perpendicular to the polishing direction, thus supposed to have the same thickness along each line) were used for thickness calculation, which gives the thickness of ~ 514 nm and 362 nm, respectively. Since this calculation is purely based on mass-thickness contrast, those grains with strong Bragg diffractions (under zone axis, shown as grains showing relatively black contrast in the figure) will cause errors in the calculation. To minimize this effect, intensity averaged along each line is used which is the I_{tr} in Equation 3.5. To get I_0 in Equation 3.5, one needs only to measure the intensity outside the sample edge (blank area). The validity of the thickness measurement can be checked by calculating the wedge angle against the theoretical one which is 4^o. Using the thickness of two lines, the calculated wedge angle yields ~5.24^o, fairly close to the pre-set wedge angle, considering the inevitable mechanical error during the polishing process and the roughness of the sample surface caused by polishing, the consistency is deemed good. Using such thickness measurement method, the sample thickness of the wedge tip has been determined to be in the range of approximately 300-800 nm, depending on the quality of the sample preparation.

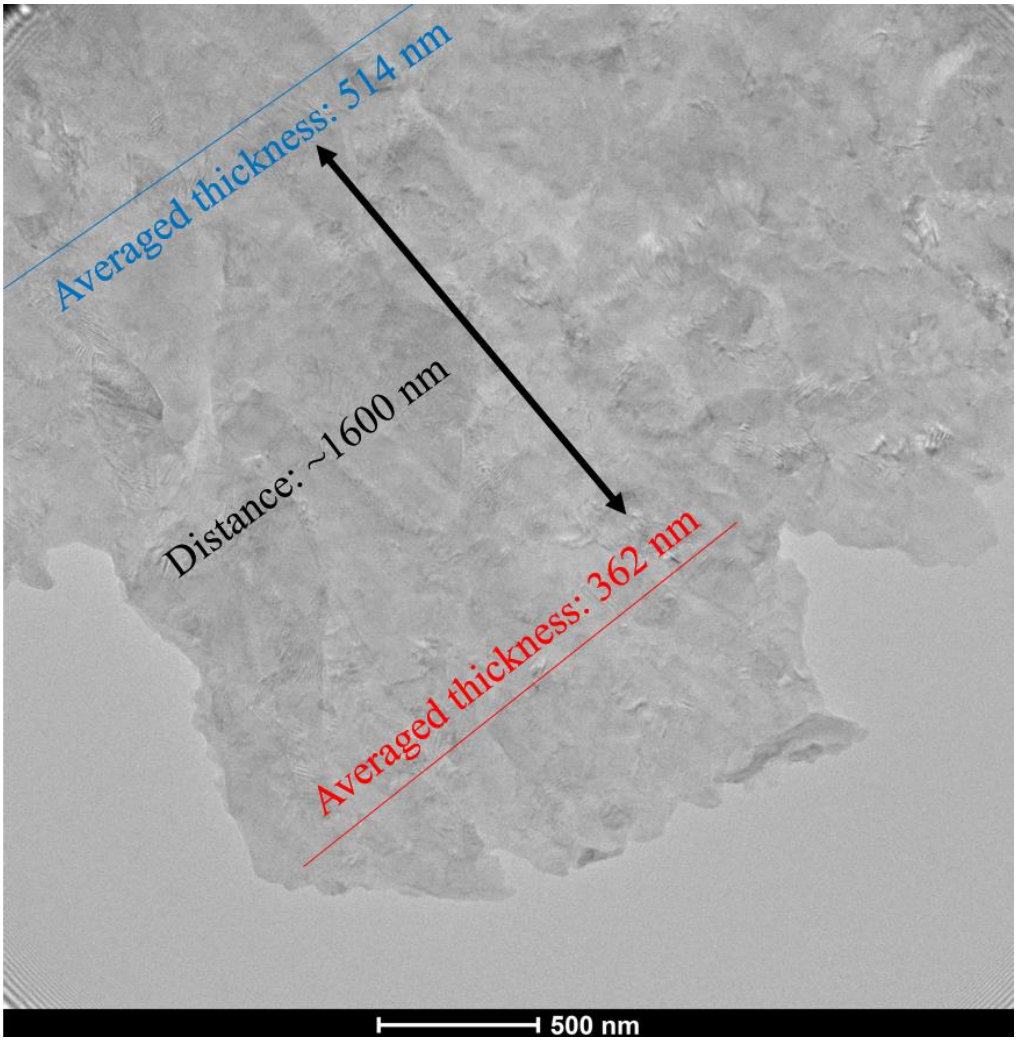

Figure 4.5 Thickness measurement used in the current study. Averaged intensity along each line is used for the thickness calculation to minimize the effects of diffraction contrast.

4.3 Origin of the Nano-crystalline in Wedge Samples: Rotational Dynamic-recrystallization (DRX)

The microstructural discrepancy between the nano-crystalline wedge TEM samples and the coarse-grained initial solid-solution treated samples strongly suggests that these nano-grains originate from the mechanical polishing process. This can be explained on the basis of SNC mentioned earlier, applying surface plastic deformation (the mechanical polishing as in the current case) has been used to produce nano-crystalline or gradient structures in previous research [64, 115, 116]. Understandably, the extent and effectiveness of mechanically induced SNC are directly

proportional to the strain/strain rate applied to the materials, which causes the relationship between the evolving strain/strain rate and the corresponding gradient structure shown in Figure 4.6 [177]. Consequently, in order to manufacture better nano-crystalline surface layers, methods capable of introducing large strain/strain rate are usually used, for example, surface mechanical attrition treatment (SMAT) [115], laser shot peening (LSP) [178], ultra-sonic shot peening (USSP) [179] and surface mechanical rolling treatment (SMRT) [180], etc. Despite of different approaches used, all these techniques share a similar idea of somehow deforming the surface layers, the major difference is the severity of plastic deformation being introduced. And understandably, the more severe the plastic deformation is on the surface, the finer and thicker the nano-crystalline layer would be [181]. It is therefore quite intriguing that in the current case large area of homogeneous nano-grains can be produced using such a low polishing rate (5 rpm) and relatively fine sandpapers (0.5 μm), considering that polishing using coarser sandpapers and higher polishing speed resulted in only a small portion of nano-grains in Cu, despite its similar hardness with Mg [182].

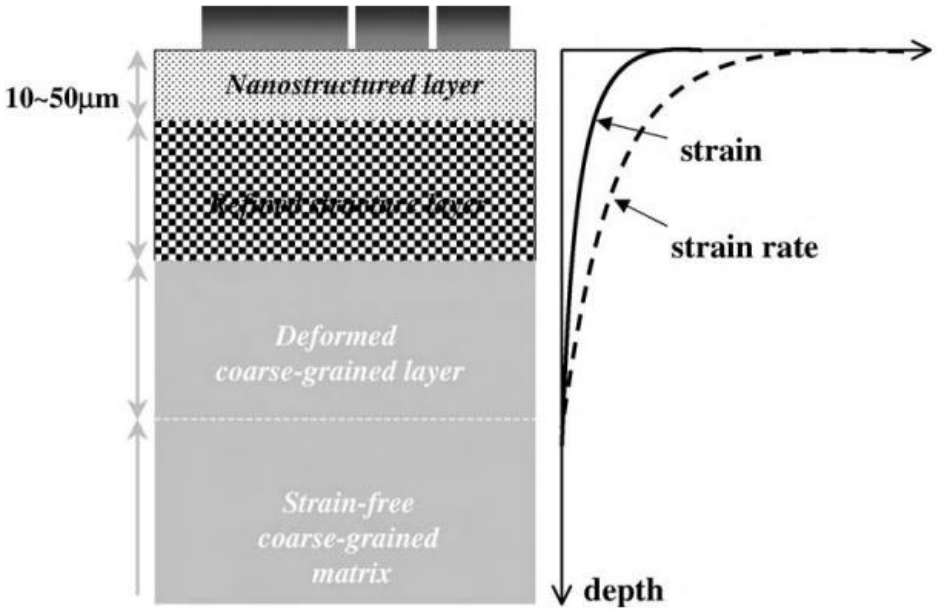

Figure 4.6 Schematic illustration of the evolution of strain/strain rate and corresponding microstructure along the depth of the nano-crystalline layer, adopted from ref. [177].

Though the majority of research on SNC in HCP materials is contributed to titanium (Ti) and its alloys, a few studies on Mg has shown that the formation mechanism of SNC in Mg and its alloys can be generally divided into the following three stages [115, 179, 183]: I) activation of deformation twinning caused by initial plastic deformation, which divides coarse grains into twin platelets; II) formation of shear bands, dislocation arrays, and sub-grains as the deformation proceeds; III) occurrence of DRX that leads to the formation of nano-crystalline. Unlike Ti and its alloys, Mg, with a higher c/a ratio, possesses fewer slip systems at room temperature, leading to the frequent activation of deformation twinning. Thus it is feasible for the twinning to take place in the early stage of the SNC process to help accommodate the plastic deformation. It should be noted that in the current case of wedge TEM samples, it is the top-most layer (which corresponds to stage III) that is essentially being observed, as a result, no deformation twinning has been found in any of the wedge TEM samples. Although the most observable areas of the wedge TEM samples are comprised of homogeneous nano-grains, there is still evidence of microstructural features from stage II in some area. As can be seen in Figure 4.7 (a, b), instead of well-defined nano-grains, lamellae with a high density of dislocations marked by red arrows are presented, the discontinuity in the corresponding SAED shown as the inset of Figure 4.7 (a) also demonstrates the presence of high-density dislocations and sub-grains, few nano-grains as indicated by the red circle exist near these lamellae. Though the high dislocation density in these areas makes it difficult to image individual dislocation lines, small mis-orientation caused by the presence of dislocations in these lamellae can be clearly seen via the convergent beam electron diffraction (CBED) patterns shown in Figure 4.8 (b-d). Such microstructures have been well documented in stage II of SNC in Mg and its alloys, as can be seen in Figure 4.7 (c, d) [179]. The formation of such lamellar structure is believed to be associated with the extensive activation of both basal and non-basal dislocation slips as the extent of deformation increases progressively [183].

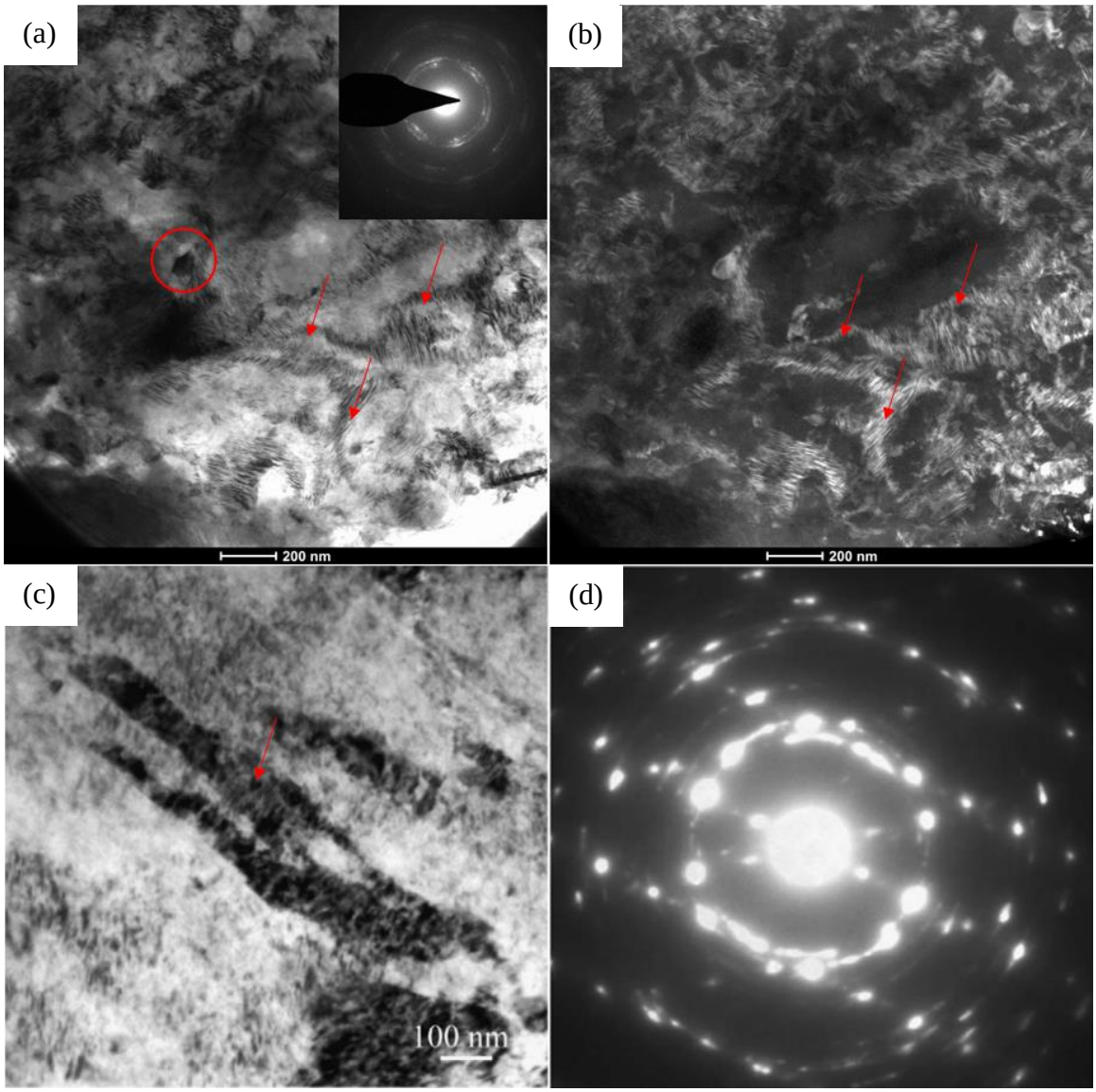

Figure 4.7 Areas with high dislocation density and less well-defined nano-crystalline. (a) BF and (b) DF images of areas containing highly deformed lamellae marked by red arrows, the corresponding SAED pattern showing discontinues diffraction ring is shown as inset, note there is still the presence of few nano-grains as noted by the red circle; (c) similar lamellae with a high density of dislocations in RE-Mg alloys prepared by USSP and (d) the corresponding discontinuous SAED pattern, both adopted from ref. [179].

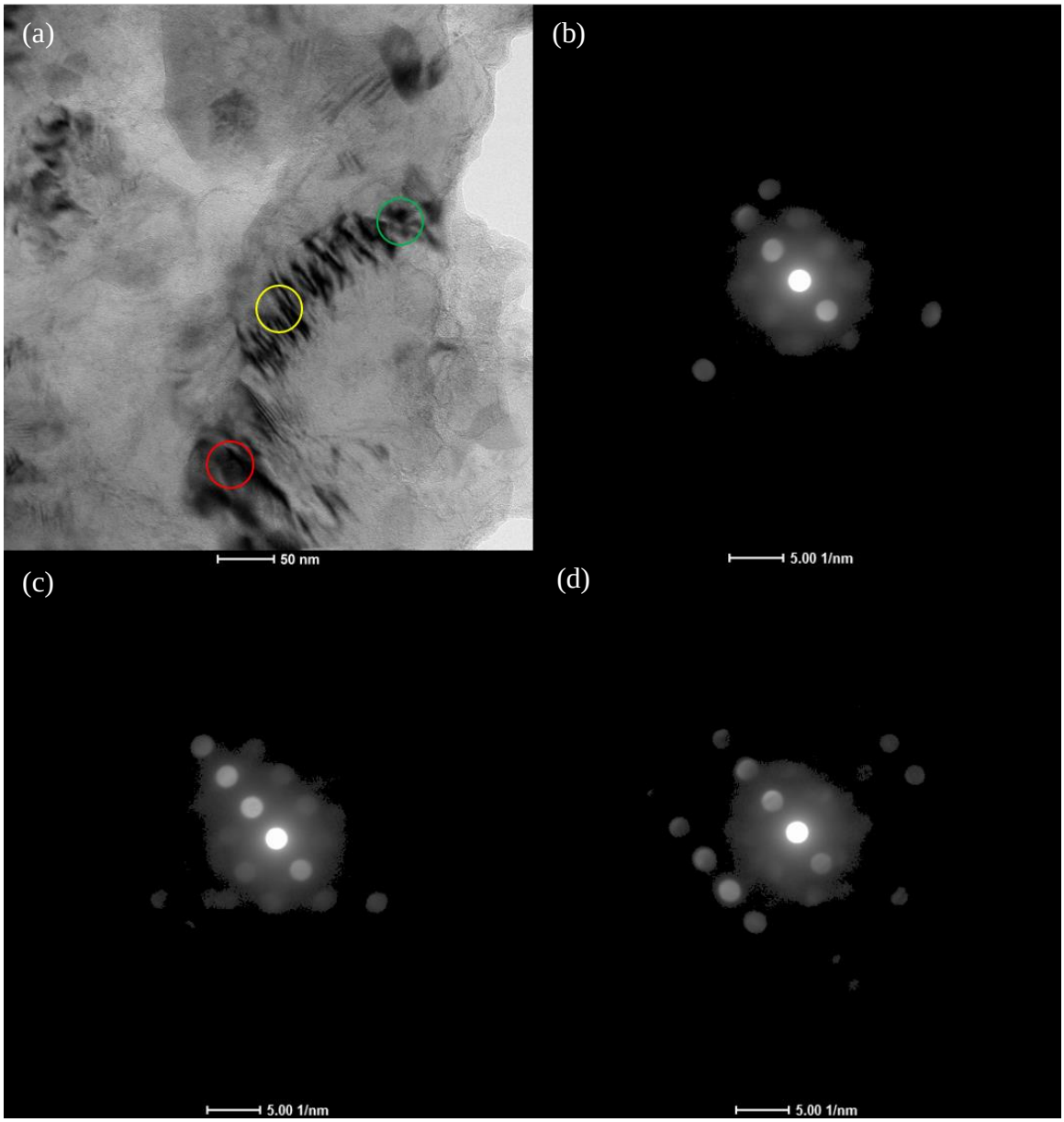

Figure 4.8 Mis-orientation inside area with complex contrast, indicating a high density of dislocations. (a) A lamella with a high density of dislocation inside, (b-d) CBED patterns taken at the red, yellow, and green circled areas, respectively, showing observable mis-orientation.

Closer inspection of these lamellar areas shows that sub-grain boundaries consisting of dislocations array can be found as exhibited in Figure 4.9 (a), similar to what is reported in ref. [183]. Though not clearly visible in the BF image, the mis-orientation across the sub-grain boundary marked by the red dashed curve can be seen unambiguously by the DF images using different diffraction spots as shown in Figure 4.9 (c, d). The curvature of the sub-grain boundary indicates the presence of

cross-slip during the deformation [184]. Due to limited available slip systems, the dislocation density inside the dislocation array in Mg is usually not high enough to form actual grain boundaries as in the case of cubic materials [185-187], instead, only sub-grain boundaries form which can store a significant amount of strain energy, leading to possible activation of DRX [183] that form the nano-grains observed in the current study. Those nano-grains inside the lamellar area (e.g., the one marked by the red circle in Figure 4.7 (a)) are likely the first few grains in these areas that have undergone such process.

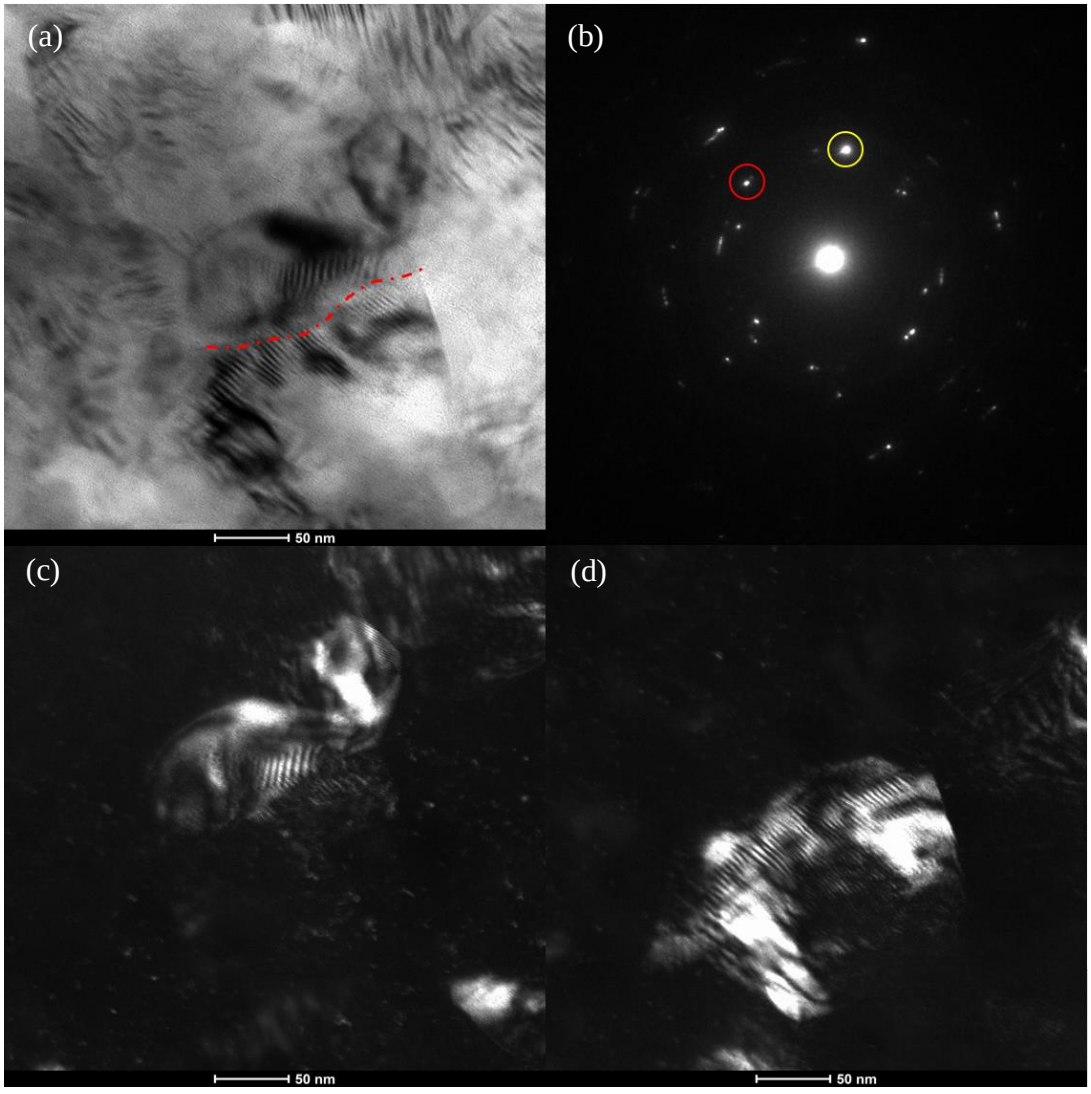

Figure 4.9 TEM micrographs showing potential sub-structures inside nano-crystalline. (a) BF image of a nano-grain containing a curvy sub-grain boundary marked by the red dashed curve and (b) the corresponding SAED pattern, reflections marked by red and yellow circle were used to form the DF images shown in (c) and (d).

Though DRX is mostly found in materials deformed at elevated temperature, pure Mg has a relatively low melting point (650 ^{o}C), leading to a DRX temperature as low as ~200 ^{o}C [183], which can be further decreased by the adding of alloying elements [188]. It is also known that the presence of strain can decrease the melting point and thus decrease the DRX temperature [189]. There are even reports on room temperature DRX happening in Cu which has a higher melting point than Mg [182, 190, 191]. While the wedge TEM samples are prepared at ambient temperature, heat can be generated through the mechanical polishing process, when the samples are thin enough, despite the fact that fine sandpaper and low polishing rate are used, the actual strain rate at the tip of the wedge may be high enough to cause a local temperature rising that is capable of triggering the DRX process. In fact, in some SMRT processes, liquid nitrogen is used to compensate for the mechanical heat caused by the deformation, to prevent the possible grain growth induced by the temperature rising after DRX [180]. Such cooling is unnecessary in the preparation process of the wedge TEM samples, due to their small size, low polishing rate, and liquid lubricant constantly applied, the heat generated by the deformation process quickly dissipates once the DRX is triggered, leaving no room for further grain growth.

The detailed DRX process involved in the formation of nano-grains in the wedge TEM sample may be understood on the basis of adiabatic shear bands (ASBs). ASBs are defined as areas with extremely localized plastic deformation, usually found in materials subjected to high-strain-rate deformation [192]. Both originated from SPD, similar deformation-induced nano-crystalline and lamellar structures have also been reported in the center and perimeter of ASBs [192, 193], which corresponds to stage III and stage II in mechanically induced SNC. While many different variations exist for the mechanisms of DRX, most of them can be classified into migrational and rotational types as proposed by Derby [194]. Although migrational DRX is commonly observed in metals, due to the extremely high strain rate, the deformation time is far too transient for the migrational DRX mechanism to account for the formation of ABSs. Consequently, the rotational DRX

mechanism, which is well-known in non-metallic geological materials like quartz [195], has been proposed to explain the DRX process of ABSs. It has been shown by Yang et al. [193], on basis of the rotational DRX mechanism, that nano-grains with sizes ranging from 100-500 nm can be formed through rotation of the sub-boundaries as quick as 20 μs, which can be even further decreased given higher temperature or smaller sub-grain size. The time needed for heat to dissipate from the wedge tip may be roughly calculated using Equation 4.1 [195], where x is the thermal diffusion distance, λ the thermal diffusivity, and t the time for thermal diffusion. Taking a sample thickness of ~400 nm for the thermal diffusion distance, 0.41 cm^2/s for the thermal diffusivity reported in alloys with similar chemical composition [196], the time needed to complete the heat transfer is ~1 ns, if 30 min polishing was chosen for the final polishing, a total of 1 ns×30 min×5 rpm=150 ns=0.15 μs can be obtained for the total time allowed for traditional migrational DRX. With such transient growing time, it is highly unlike for the migrational DRX to be responsible for the observed nano-crystalline [195]. Though the calculated growth time is relatively small compared to what is reported in ref. [195], the small sub-grain sizes as can be seen in Figure 4.9 and the possible high strain rate at the wedge tip may help the activation of such rotation process [197].

$$x=(\lambda t)^{1/2}$$

Equation 4.1 Equation for thermal diffusion distance [195].

4.4 Conclusions

In this chapter, nano-grains prepared via a novel sample preparation technique have been characterized using TEM, major findings can be summarized as follows:

1. Taking advantage of the mechanically induced SNC process, the new mechanical polishing approach combines the preparation of nano-grains and TEM thin film into one single step. No complicated equipment or process is required, and it can prepare nano-crystalline TEM samples in less than one hour out of coarse-grained Mg-Gd binary alloys with a good success rate, greatly

improving the efficiency. Additionally, such sample preparation is likely applicable to a wide range of metallic materials due to its surface treatment nature;

2. The prepared wedge TEM samples exhibit a rather homogeneous distribution of nano-grains ~114 nm across the sample tip. EBSD and TEM characterization on the initial solid-solution treated samples reveal the origin of these nano-grains to be mechanically induced SNC introduced by the polishing process;

3. The formation mechanism of these nano-grains is explained based on the rotational DRX process, to which the high stress/strain rate at the wedge tip likely contributes, making its activation possible at low temperatures.

Our current findings can be of great help to researchers interested in nano-crystalline materials by introducing a simple, fast, cost-efficient yet versatile way to manufacture nano-crystalline wedge samples used for TEM investigation.

Chapter 5 Results: Deformation Mechanisms of Nano-crystalline Metals

5.1 Feasibility of Using HCDF to Track Grain Re-orientation

The contrast-orientation relationship of HCDF needs to be confirmed before it's used experimentally. Shown in Figure 5.1 (a, b) is an example of the intensity oscillation curves with increasing sample thickness and corresponding simulated HCDF image with a sample thickness of 200 Å. The half oscillation periods of all calculated zone axes, which are obtained at the sample thickness with the first intensity maximum in the oscillation curve, are plotted in Figure 5.1 (c), from which it can be seen most zone axes have a half oscillation period around 200 Å. The fluctuation can be caused by slight differences in dynamics scattering of difference g-vectors, such as [0001] and $[1\bar{1}00]$. The amplitude of such fluctuations can be also likely amplified by the slicing error, because atoms are not exactly lying on flat planes for some high-order zone axis, causing higher simulation error [165]. As expected for the contrast-orientation relationship of HCDF, all zone axis containing at least one g-vector of the three slip planes (namely, slip plane(s) edge-on) show relatively strong intensity, usually above 0.1. While for those without any g-vector of the three slip planes, for example, the $[2\bar{2}03]$ zone axis exhibits negligible intensity ~0.002 for all calculated sample thicknesses up to ~400 Å. To better visualize this result, an IPF color-coded based on the intensity of each zone axis is shown in Figure 5.1 (d) using stereographic projection [138]. All zone axes without any g-vector of the three slip planes are essentially shown as black dots in the plot, blended with the background, the white edge around each data point merely serves as an indicator of where the zone axes with near zero intensity are located in the plot.

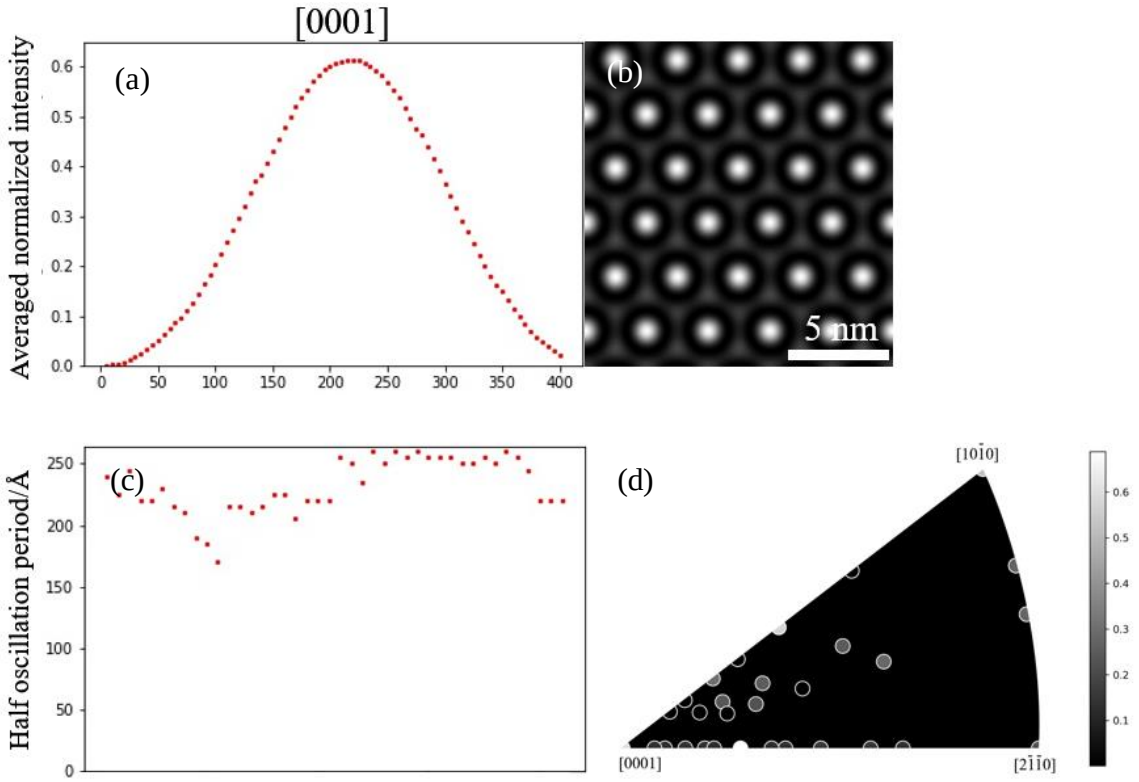

Figure 5.1 HCDF contrast with different crystallographic axes. (a) Intensity oscillation with sample thickness for [0001] zone axis and (b) the corresponding simulated HCDF image with sample thickness 200 Å; (c) half oscillation period distribution of all calculated zone axis; (d) IPF color-coded based on the calculated intensity of each zone axis, sample thickness was held constant at 200 Å for all data point in the plot.

Before jumping to the conclusion that HCDF can be indeed used for tracking orientation change based on their contrast, the validity of the simulation needs to be checked first. The oscillation curve of HCDF and BF images for the [0001] zone axis is shown in Figure 5.2, the self-consistency of the Multi-slicing program is demonstrated by the complementary intensity of HCDF and BF images at the same sample thickness, which roughly adds to 1, the flux for electron beam before interacting with the sample. The reason for the values to be less than 1 is that the collecting range of HCDF plus BF doesn't cover the whole reciprocal space, leaving some electrons unaccounted for. It should be noted that multi-slicing considers only the elastic interaction between electrons and sample atoms, those electrons subjected to inelastic scattering will essentially be lost [165], which is the reason that multi-slicing works better for very thin sample thickness where elastically scattering of electrons dominates.

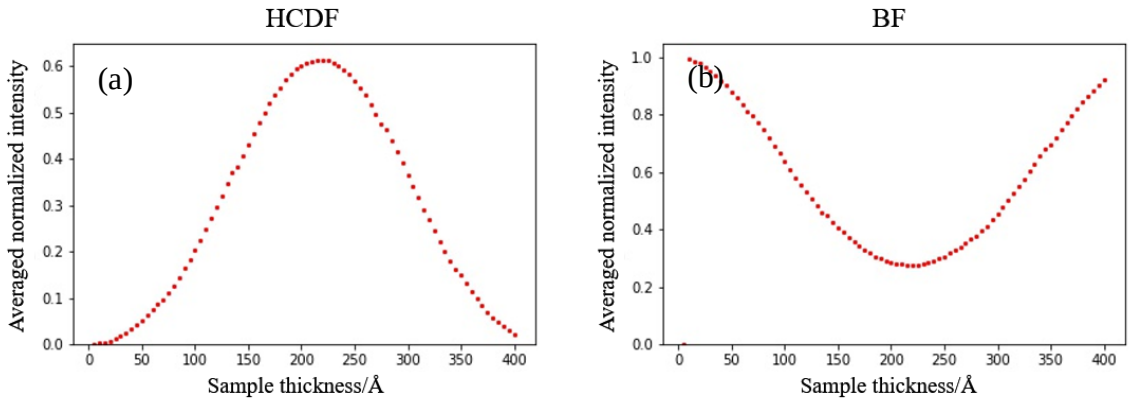

Figure 5.2 Comparison between the intensity oscillation curves of HCDF and BF images. (a) HCDF and (b) BF, showing complementary intensity given the same sample thickness.

To demonstrate that the modified virtual objective aperture is indeed working appropriately to form HCDF images, images of the $[10\bar{1}0]$ zone axis simulated with three specific collecting ranges are shown in Figure 5.3 (a-c). When the collecting range is $k<30$ 1/nm (k is in spatial frequency, following the convention of $k=1/d$ in ref. [165]), both g=$(1\bar{2}10)$ and g=(0002), indicated by red and green arrows in Figure 5.3 (d), are allowed to contribute to the image, since HRTEM image is essentially phase contrast image caused by the interference between difference reflections [138], a regular lattice image can be formed by the interference between g=(0002) and g=$(1\bar{2}10)$. However, if the collecting range is changed to 15 1/nm$<k<$ 16 1/nm so that only g=$(1\bar{2}10)$ is allowed to contribute to the image. Since only one reflection is allowed to form the image this time, only fringe image as shown in Figure 5.3 (b) can be formed. Similarly, if the collecting range is set to 8 1/nm $<k<$ 11 1/nm so that only g=(0002) contributes to the image, another image with perpendicular fringes caused by the g=(0002) reflection is formed in Figure 5.3 (d). The consistency between the collecting angle and the simulated images indicates that the modified virtual objective aperture for HCDF imaging is indeed working appropriately. Therefore, it can be concluded, based on the above simulation results, that it is feasible to use contrast changes in HCDF images to present the orientation changes of Mg.

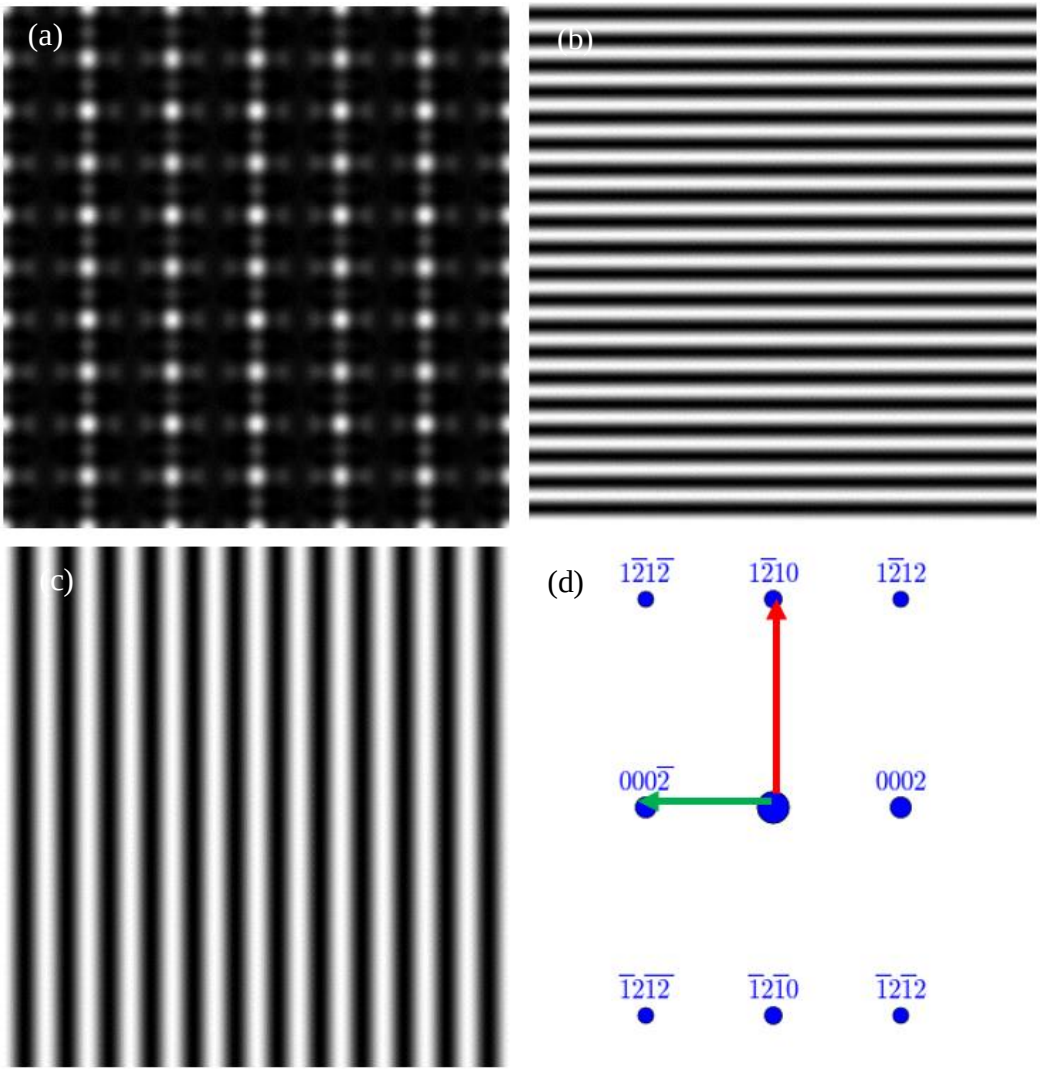

Figure 5.3 Verification of applied virtual aperture. Simulated images taken with collecting angle of (a) k<30 1/nm, (b) 15 1/nm <k <16 1/nm and (c) 8 1/nm <k< 11 1/nm for [10$\bar{1}$0] zone axis; (d) simulated SAED pattern of [10$\bar{1}$0] zone axis, g=(1$\bar{2}$10) and g=(0002) responsible for the fringes seen in (b) and (c) are noted by red and green arrows, respectively.

5.2 Significant Grain Re-orientation

TEM nano-indentation was conducted on the wedge sample and recorded in BF imaging mode, the corresponding load-displacement curve and series of snapshots taken from the movie are exhibited in Figure 5.4 (a, b). Contrast changes of nano-grains during indentation indicate possible orientation changes, there are also abundant complex linear contrast moving quickly during deformation, especially near the indenter tip, likely due to dislocation activities.

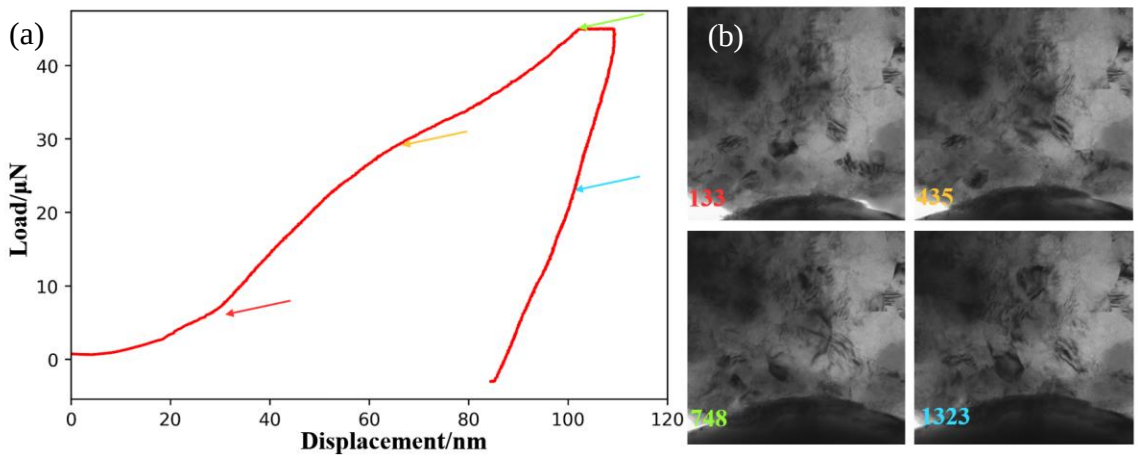

Figure 5.4 In-situ TEM nano-indentation test recorded in BF imaging mode. (a) The corresponding load-displacement curve and (b) snapshots taken from the movie, the color and value of the colored number in each image indicate where at the curve and at which frame of the movie they are taken.

The original microstructure and corresponding SAED pattern before indentation are exhibited in Figure 5.5 (a, c), the grain orientation shows a rather random distribution, as can be seen by the spotty but rather homogeneous ring-like diffractions. The post-mortem inspection shown in Figure 5.5 (c, d) after the nano-indentation is performed shows that some grains have undergone noticeable grain re-orientation, as demonstrated by the SAED pattern in (d) where less continuous diffraction ring and redistribution of diffraction spots have been captured. Apart from grain rotation, some grain boundary migration has also been noticed. As can be seen in Figure 5.5 (a, c), the grain boundary of a nano-grain marked by the red circle in (a) has advanced towards the sample edge, forming a tip-like grain boundary in (c), while other grain boundaries of the nano-grain show little change. Such result hints at possible cooperation between these two mechanisms, as past MD simulations suggest that these grain rotation and grain boundary migration can happen simultaneously and the coupling between them likely leads to better plasticity of nano-crystalline materials by reducing the CRSS of dislocation emission [127, 198].

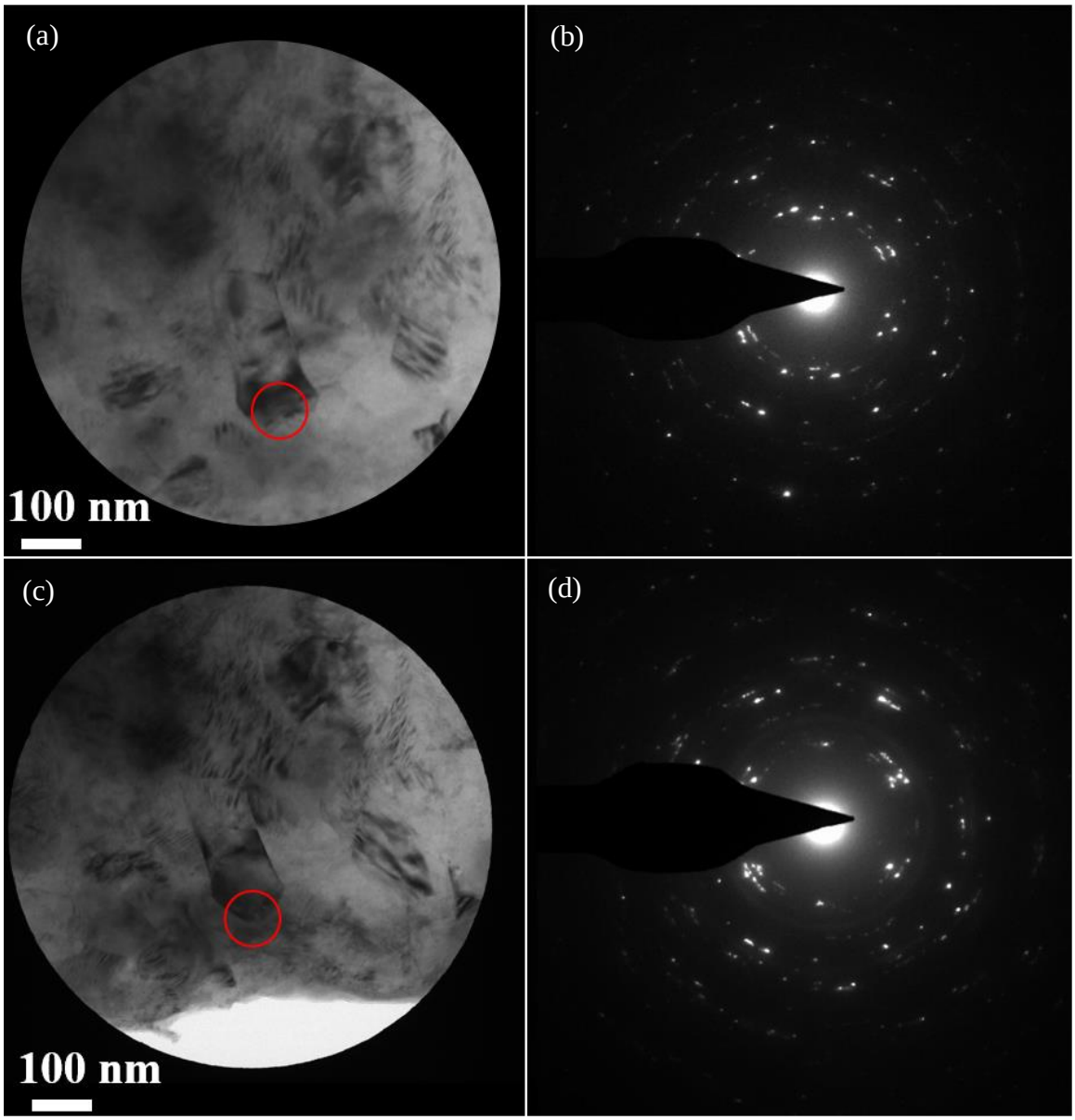

Figure 5.5 Comparison between the BF images and corresponding SAED patterns of the same area after deformation. (a,b) before and after (d) indentation. Note the obvious redistribution of diffraction spots in SAED patterns and the grain boundary migration marked by the red circle. The circles enclosing the images in (a) and (c) show the area selected by the select-area aperture.

Although the above BF and corresponding SAED pattern give a rough idea that grain rotation might have happened during nano-indentation, it offers no indication whatsoever of the nature of the rotation process itself. The dynamic nature of in-situ nano-indentation imposes strong limitations on the techniques that can be used for characterization, essentially excluding scanning-based techniques like EBSD or TKD due to excessive time required. Atomic image approaches like

HRTEM can be possible in certain cases [199, 200], but have rather strict limitations like limited viewing area and is unable to track large angles of rotation. The most effective way used previously is conventional DF imaging, however, few nano-grains can be tracked simultaneously due to the fact that only a limited portion of diffraction is used for imaging while the most part of it is just simply dumped, as can be seen in the previous research using conventional DF for imaging [137] [201]. Additionally, if the grain rotates such that its diffraction moves out of the objective aperture but still stays on another portion of the diffraction ring, conventional DF then fails to recognize it and simply treated that plane as being rotated away from edge-on. These problems can all be solved if HCDF is applied, as the whole diffraction rings are now being collected. A comparison of how much more grains HCDF can track than conventional DF imaging is shown in Figure 5.6 (a, b), where the HCDF image is clearly showing significantly superior imaging ability for nano-crystalline materials. Thus HCDF is adopted in the in-situ TEM indentation test to study in more detail what exactly happened during the indentation.

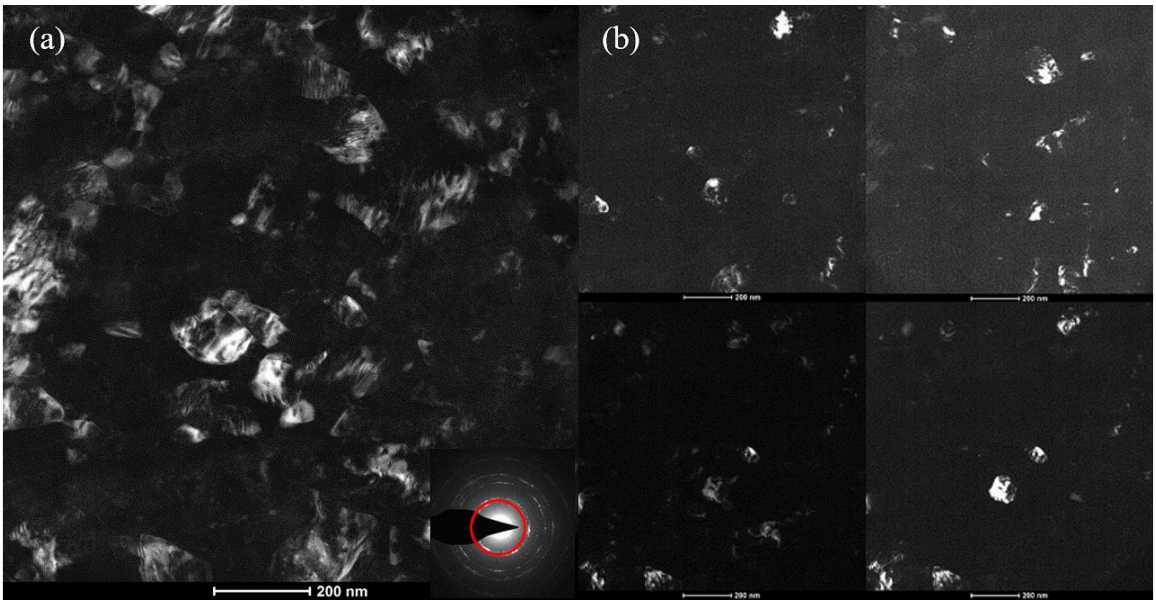

Figure 5.6 Comparison between HCDF and conventional DF imaging. (a) HCDF image formed using diffraction rings noted by the red circle, showing multiple grains in bright contrast (slip planes edge-on) and (b) four conventional DF images of the same area formed using one portion of the diffraction rings noted by the red circle, much fewer grains are now in bright contrast.

As can be seen in Figure 5.7 (a), the HCDF image taken before indentation, most areas like the one marked by the red circle show none or dim contrast, meaning none of their three slip planes were edge-on before indentation. According to the corresponding SAED pattern shown as an inset in Figure 5.7 (c), the nano-grains before indentation show a rather homogenous orientation distribution. However, as can be seen in the HCDF snapshot taken from the late stage of nano-indentation shown in Figure 5.7 (b), numerous small grains near the indentation tip are now showing bright contrast. Especially for the red-circle marked area that previously showed dim contrast, where multiple nano-grains with high contrast are now clearly visible. The comparison between these two images demonstrates that the rotation of these nano-grains is not completely random, but follows a specific pattern such that more of their slip lanes are rotated edge-on. It should be noted that despite having been carefully aligned with the indenter, bending of the sample during indentation is practically inevitable, considering the previous random orientation distribution, it is unlikely that the bending alone can cause simultaneously edge-on of slip planes of multiple grains marked by the red circle in Figure 5.7 (b). The SAED pattern now shows fewer continuous diffraction rings as shown in Figure 5.7 (d). Such "texture-like" feature is another indication that grain rotation indeed happened during the indentation, after all, bending of the sample cannot produce such diffraction pattern with preferential grain orientations (note the concentrated diffraction arch indicated by the red arrows). Rotation of these grains (some as large as ~100 nm) is rather uncommon as grain rotation is usually believed to be more favorable in small grains with tens of nanometers in size. The possible reason could be that the GBs in current samples might be non-equilibrium, as heating experiments have been shown that these nano-grains are not stable and tend to grow easily at low temperature heat treatment (~170 ^{o}C). Thus the rotation process might be driven by the energy reduction to transfer these unstable GBs to more stabilized states. Another possible reason may be attributed to the two free surfaces presented in the case of wedge samples, as compared to bulk cases where grain deformation is constrained by their neighbors. Such rotation of grains has been observed in multiple indentations done in different

samples, as can be seen in Figure 5.8, another indentation done at thicker sample (~200 nm). Most indentations show edge-on of slip planes and tendency for grains to be linked together at the late stage of deformation.

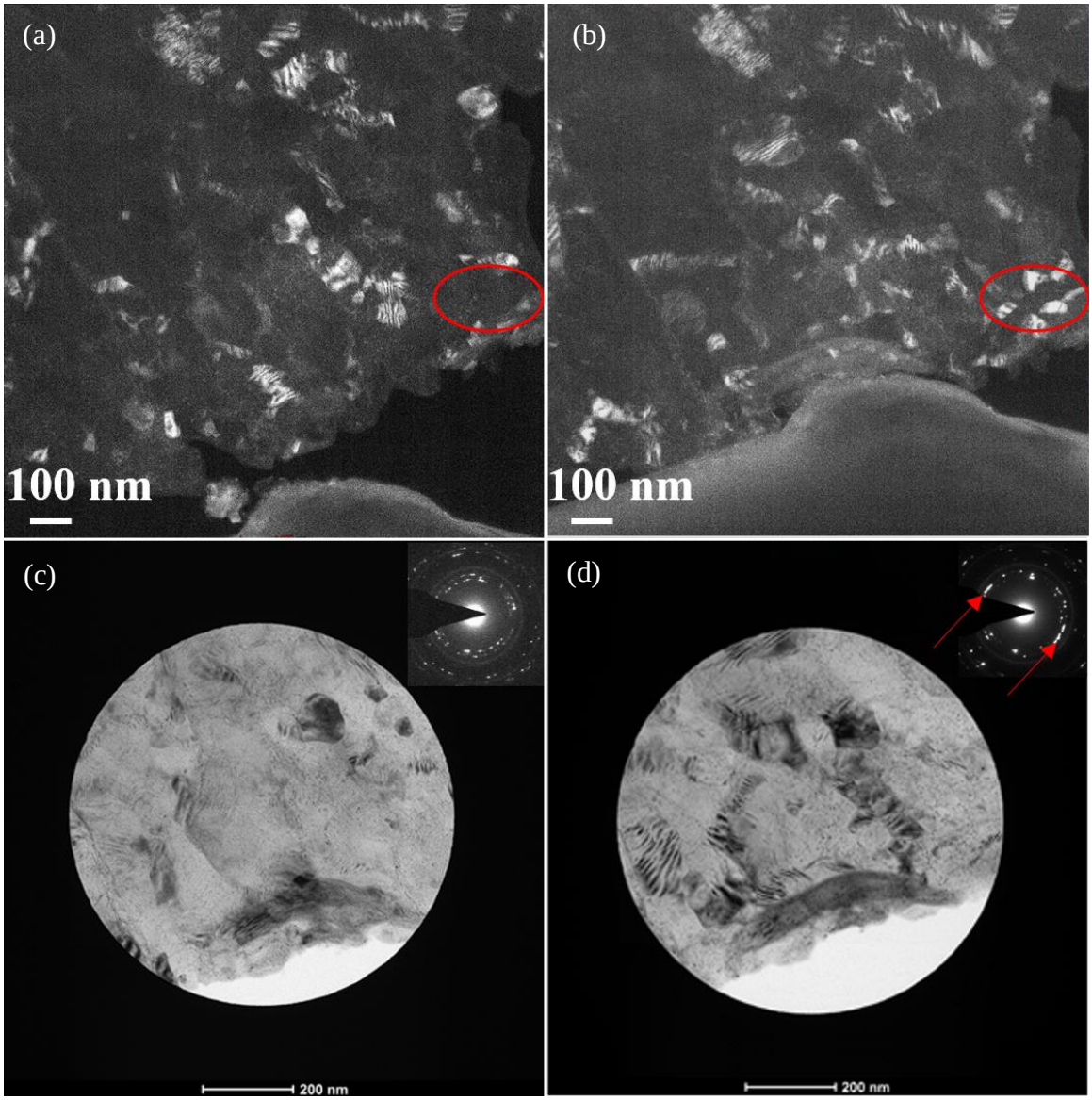

Figure 5.7 Grain re-orientation during the in-situ nano-indentation. (a) HCDF image taken before the nano-indentation and (b) HCDF snapshot taken from the movie at the late stage of indentation, note multiple areas previously dim are now showing bright contrast; BF images and corresponding SAED patterns taken (c) before and (d) after indentation.

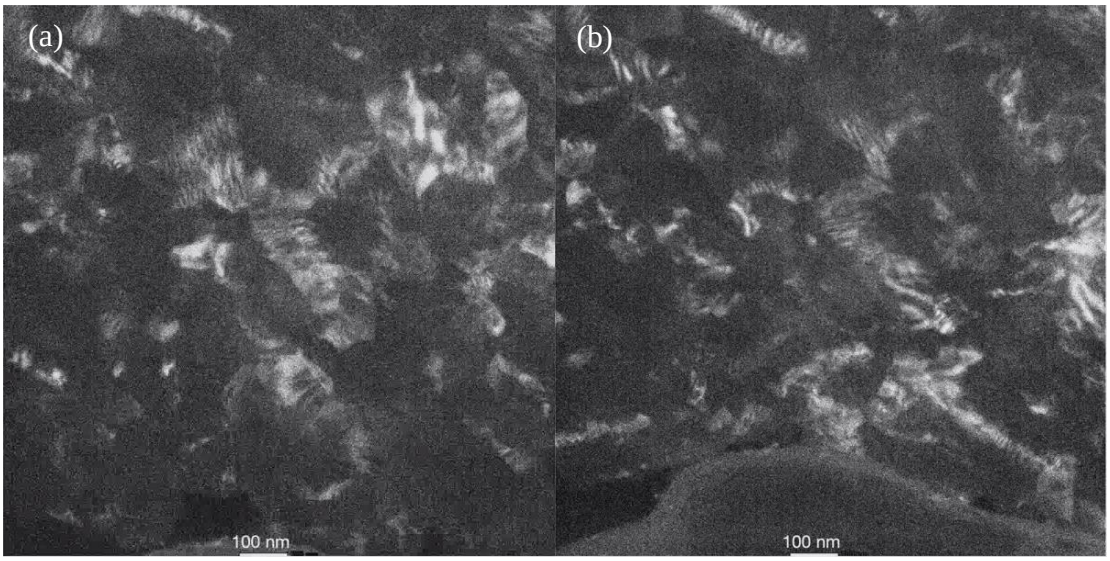

Figure 5.8 Another indentation done at a thicker sample. (a) Before and (b) at the late stage of indentation.

Though difficult to perform HRTEM during indentation, post-mortem HRTEM analysis can still offer valuable information in addition to the in-situ data. As can be seen in Figure 5.9 (a), an HRTEM image taken before indentation, the corresponding fast Fourier transformed (FFT) image generated using the red-rectangular area indicates that only one set of $(1\bar{1}01)$ planes marked by the yellow line, which is the pyramidal I slip plane, was edge-on. Interestingly, after indentation, as can be seen in Figure 5.9 (b), the corresponding FFT image reveals that despite that the $(1\bar{1}01)$ planes remain almost unchanged, the grain is now rotated to the $[1\bar{2}1\bar{3}]$ zone axis, which means two additional slip planes, pyramidal I $(0\bar{1}11)$ and prismatic $(10\bar{1}0)$ have been rotated edge-on. Given the fact that the $(1\bar{1}01)$ plane remains effectively unchanged throughout the indentation, the rotation likely happened by rotating around the plane normal of the $(1\bar{1}01)$ plane. Such observation that more slip planes of Mg are being rotated edge-on agrees perfectly with the in-situ observation. It is worth mentioning that similar to what was discussed in Figure 5.5, additional grain boundary migration has also been captured. The angle between the lower grain boundary marked by the white line and the horizontal was ~24.6^o before indentation, however, this angle is increased to ~46.8^o after indentation, indicating the presence of grain boundary migration. This further demonstrates the possible cooperative operation between grain rotation and grain boundary migration.

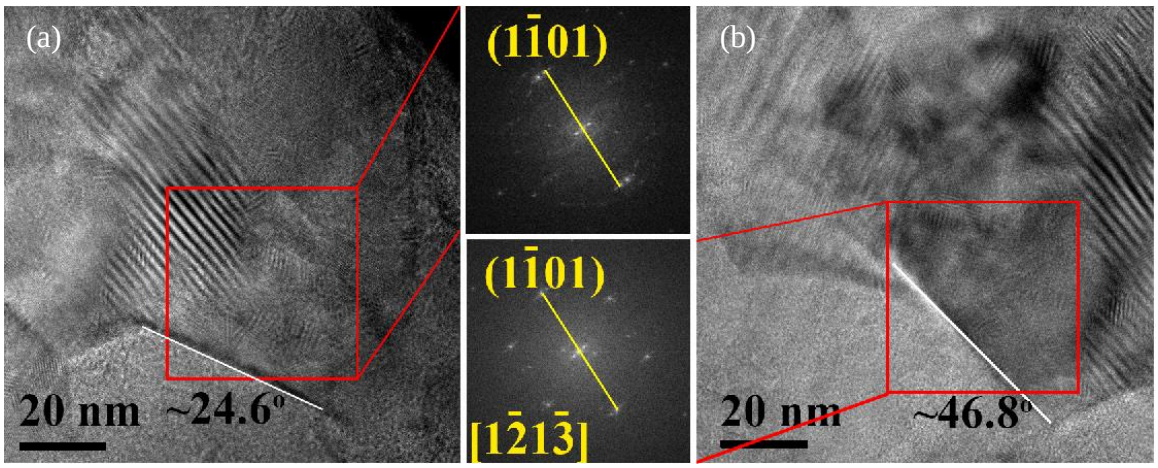

Figure 5.9 HRTEM micrographs and the corresponding FFT images of the same nano-grain. Images taken (a) before and (b) after indentation.

5.3 Dislocation Activities

Similar to those nano-crystalline produced by SPD or in the ABSs [193, 200], pre-existing dislocations left by the preparation process have also been found in nano-crystalline of the current samples. As can be seen in Figure 5.10 (a), complex contrast, which is a common indicator for lattice dislocation and residual stress [200], can be seen in multiple nano-grains. Closer DF examination using g=(10$\bar{1}$1) on a grain located at the center is exhibited in Figure 5.10 (b), where the discontinuity in Moiré fringes marked by the red circle also indicates the presence of dislocations [202].

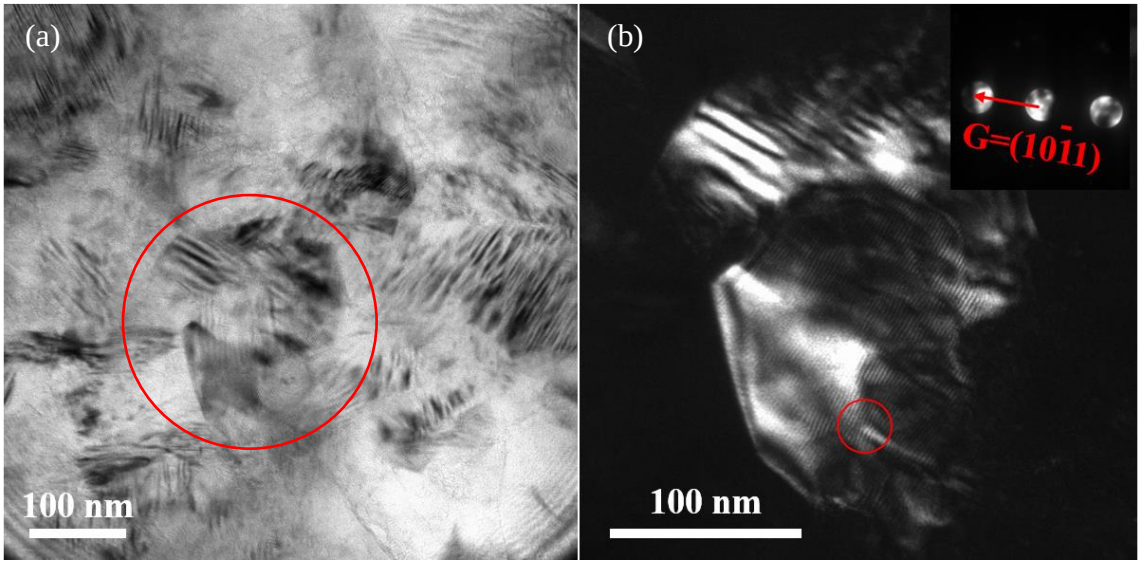

Figure 5.10 Evidence showing pre-existing dislocations inside nano-crystalline used in the current study. (a) BF image showing complex contrast inside nano-grains; (b) DF image using g=(10$\bar{1}$1) of the red-circled grain in (a), note the discontinuity in the Moiré fringes indicated by the red circle.

Although dislocations abundantly exist in the as-prepared samples and likely are involved to the plastic deformation during the nano-indentation, our HRTEM results show that newly formed dislocations also contribute actively to the deformation process. As can be seen in Figure 5.11 (a), an HRTEM image of a nano-grain under [0001] zone axis taken before indentation, Burgers' loop analysis on the upper part of the corresponding filtered inverse fast Fourier transformed (IFFT) image is closed thus no dislocation existed in this part before indentation. However, as can be seen in Figure 5.11 (c), the HRTEM of the same grain taken after indentation, once cleaned grain interior now shows linear black contrast, indicating the possible presence of dislocations. Burgers' loop analysis was performed on the same area, this time, however, an opening in the loop indicated by the red arrow appears, which means a dislocation with edge-<a> component has been created during the indentation. Interestingly, the orientation of this grain barely changes after indentation, as can be seen in the almost identical FFT images shown as insets in Figure 5.11 (a, c), despite the fact that it is close to the indenter tip during the deformation. The reason might be the grain already has 3 sets of {10$\bar{1}$0} slip planes edge-on under [0001] zone axis before deformation, making it easy to deform without any rotation of the grain.

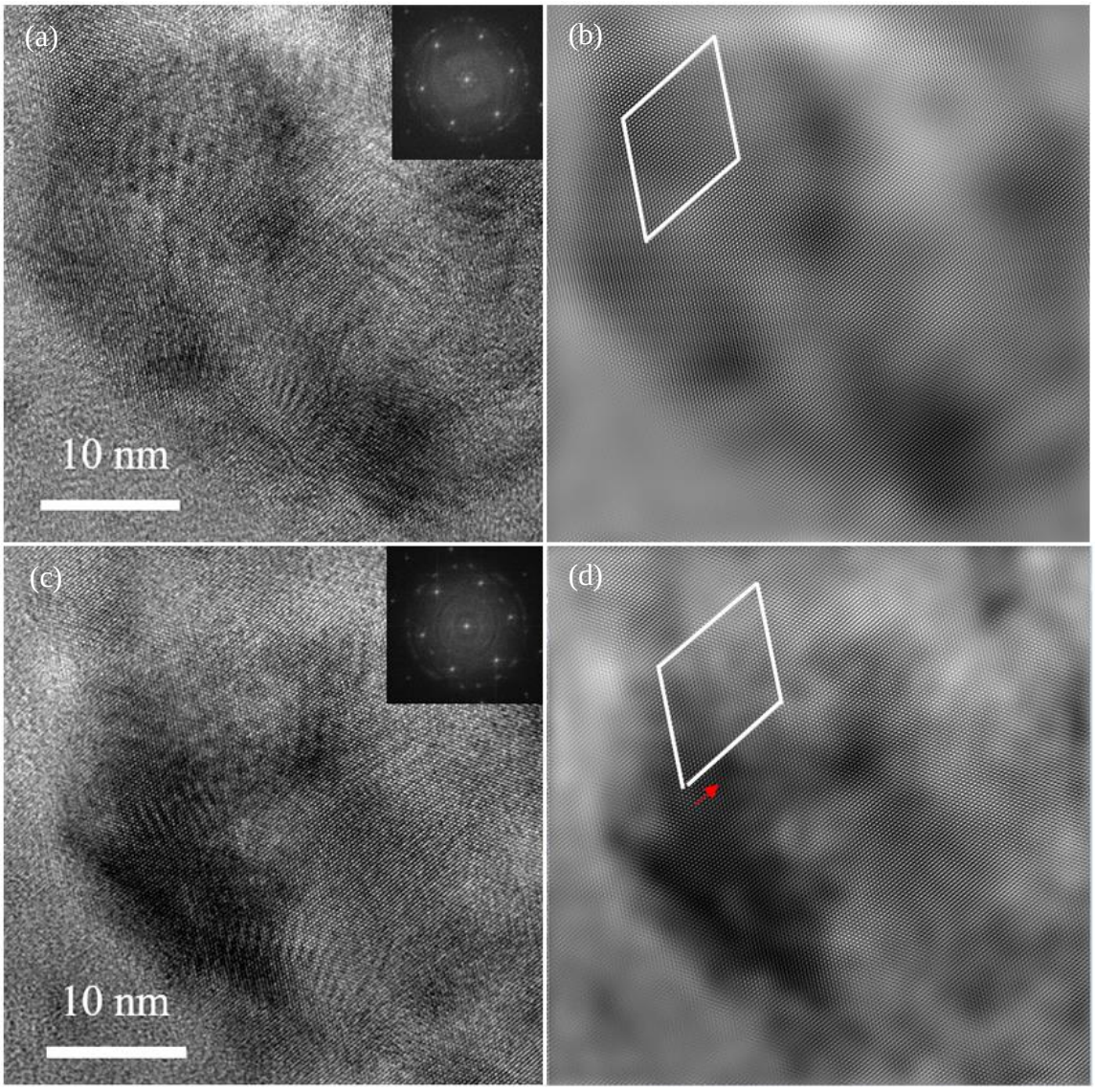

Figure 5.11 HRTEM images of a nano-grain under [0001] zone axis. Taken (a) before and (c) after indentation, showing unchanged orientation after deformation; Burgers' loop analysis on the same area in IFFT images of the nano-grain (b) before and (d) after indentation.

5.4 Cooperative Deformation Mechanism Involving Grain Rotation and Dislocation Slip

Despite the fact that many researchers have found that both grain rotation and dislocation slip can contribute to plastic deformation of materials with intermediate grain size [137, 198, 203, 204] [205-207], there are actually few experimentally demonstrate possible cooperative deformation of these two deformation modes. Past researches on this topic largely remain in simulation. For

example, Liu et al. reported that grain rotation facilitates the emission of dislocations from GBs by significantly reducing the emission energy and the critical shear stress required for the emission process [205]. Similarly, Zhang et al. claimed that the grain rotation process aligns the grains such that the angle between their $[1\bar{1}0]$ direction (which is the slip direction) and the loading direction converges to ~30^{o} after deformation, indicating the occurrence of texture [125]. Though such alignment cannot be directly observed in HCDF images, it may be linked to the "texture-like" feature of the SAED pattern after indentation, as shown in Figure 5.7 (d), where most of the edge-on slip planes are rotated to the strong diffraction arch.

If such collective deformation mechanism indeed happens during the nano-indentation, "softening" of materials is expected due to the alignment of slip planes/directions as the deformation proceeds, since the difficulty of dislocation emitting from or transmitting through grain boundaries highly depends on how the slip planes/directions align with each other [208-211]. It should be noted that although the 2D SAED patterns allow only inspection of the alignment of slip planes, considering grain rotation already happened during the deformation, the slip directions likely will be aligned too through grain rotation to reduce the flow stress needed for deformation.

The load-displacement curve of an in-situ nano-indentation and series of HCDF snapshots taken from different data points in the curve are shown in Figure 5.12 (a, b). As can be seen in the load-displacement curve, instead of work hardening conventionally observed during deformation, the slope of the curve gradually decreases as indentation proceeds, indicating "softening". As discussed earlier, the corresponding HCDF snapshots show increased area with bright contrast, indicating the alignment of slip planes/directions. It can be seen that the last HCDF snapshot taken at No. 1769 frame of the movie corresponds to where the plastic instability happens in the load-displacement curves. Along with the large strain burst, large areas near the tip showing bright contrast are now clearly visible in the image, in another word, these areas are now in a "soft" orientation for dislocation slip, the complex linear-like features marked by the red circle also hints the extensive

activity of dislocations. The whole deformation process of the nano-grains may be described as following: at the beginning of indentation, activation of pre-existing dislocations and grain rotation gradually rotate slip-planes of nano-grains to align with each other, facilitating the emission and transmission of dislocations at grain boundaries, when enough area is effectively rotated to such "soft" orientation, plastic instability happens showing as large strain burst at the late stage of the load-displacement curve.

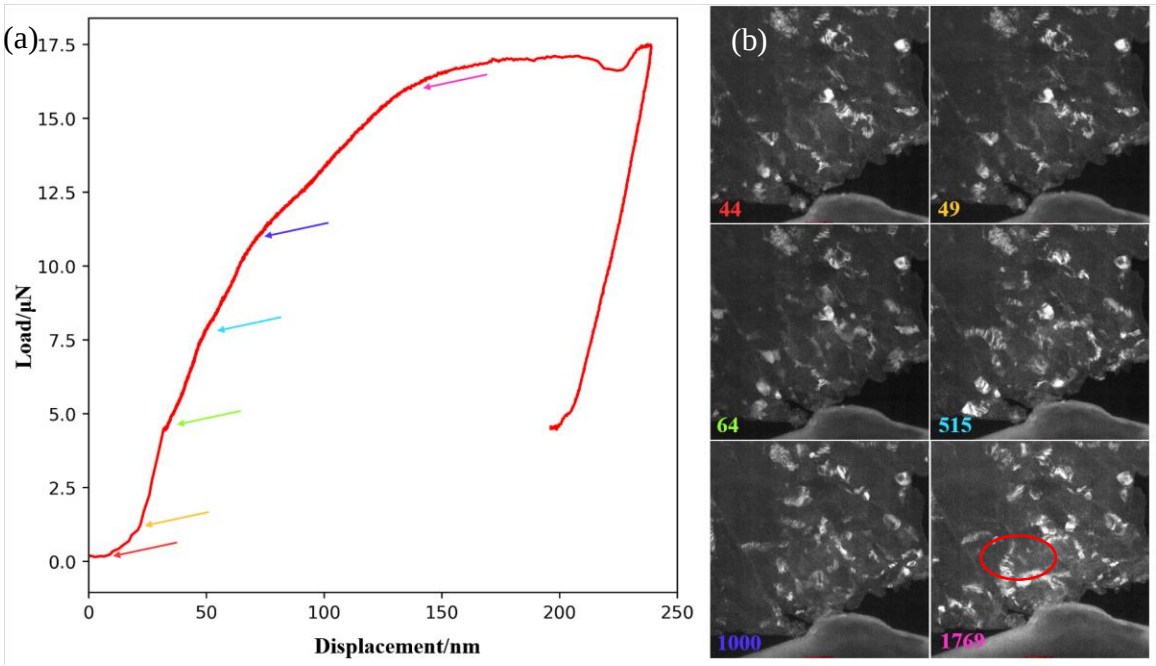

Figure 5.12 The load-displacement curve of in-situ nano-indentation and a few snapshots taken from the corresponding movie. (a) Load-displacement of an in-situ nano-indentation test; (b) series of HCDF snapshots taken from the video, the color and value of the colored number in each image indicate where at the curve and at which frame of the video they are taken.

5.5 Conclusions

In this chapter, HCDF has been used for the first time to track the slip planes' re-orientation of nano-crystalline during deformation, major conclusions can be drawn as follows:

1. Multi-slicing simulation results show that HCDF can be used to track the change in orientation in real-time using its contrast-orientation relationship in images. Additionally, given that an adequate collecting range is used, tracking the re-orientation of certain slip plane(s) is also possible;

2. Significant grain rotation has been observed using HCDF imaging during in-situ TEM nano-indentation, results suggest that grains tend to rotate such that more of their slip planes being edge-on (parallel to the viewing direction). “Texture-like” feature in the SAED patterns taken after indentation also indicates the possible alignment of slip planes/directions during the deformation process;

3. Accordingly, a collective deformation mechanism involving both grain rotation and dislocation slip has been demonstrated experimentally for the first time, which is further supported by the consistency between the load-displacement curve and the corresponding HCDF snapshots.

Our findings here deepen the understanding of the deformation mechanism of Mg alloys with intermediate grain size, experimentally validate the possible collective deformation mode between grain rotation and dislocation slip suggested previously by simulations. And in doing so, introduced HCDF imaging as a new effective characterization method for tracking the re-orientation of grains/slip planes in real-time, offering new possibilities for in-situ TEM mechanical tests.

Chapter 6 Results: Self-patterning <c>-screw Dislocation Arrays in Pure Mg

6.1 Hexagonal Patterns Found in Hot-compressed Pure Mg

Hexagonal patterns, with an interspacing of approximately 5-15 nm, are frequently observed viewed along [0001] during TEM inspection on the as-quenched high-purity Mg samples, which resembles the <c>-screw dislocation array decorated with Gb segregation found in hot-extruded Mg-Gd binary alloys [153]. A typical hexagonal pattern of a few microns in size located near a low-angle grain boundary is shown in Figure 6.1 (a), the viewing direction is along the <c>-axis (i.e. [0001] direction). Such hexagonal pattern resembles the lattice fringe image of Mg viewed along <c>-axis, a quick measurement on the patterned area, however, shows that the inter-spacing is approximately 7 nm, much greater than that of Mg lattice which is ~0.186 nm. Additionally, extra satellite diffraction spots exhibiting six-fold symmetry have been found in the selected area electron diffraction (SAED) pattern taken from the patterned area, as shown in Figure 6.1 (c). The distance between these extra reflections and enclosed Mg reflection corresponds to a spacing of ~7 nm in real space, which agrees well with the measured inter-spacing of the hexagonal pattern. The good agreement between the SAED pattern and BF image indicates that the extra satellite reflections originate from the hexagonal pattern. Additionally, though it is practically impossible to tilt the same hexagonal pattern to the perpendicular <b>-axis (i.e. $<1\bar{1}00>$ direction) of Mg, straight-line features are detected lying <c>-axis for another area viewed along <b>-axis, as shown in Figure 6.1 (b). The corresponding SAED pattern presented in Figure 6.1 (d) can be indexed as the $[01\bar{1}0]$ zone axis of the Mg matrix, without sign of satellite spots around the Mg reflections. Interestingly, the inter-spacing of these straight-line features falls also in the range of 5-15 nm, similar to that of the hexagonal pattern viewed along the <c>-axis. The contrast of these features resembles that of dislocations and is also commonly found near a low-angle grain boundary. The

consistency between the interspacing observed from the above-mentioned two perpendicular directions, along with the fact that they both originate from low-angle grain boundary, indicates that they may share a common origin and these patterns are likely composed of straight dislocation lines along <c>-axis, similar to the dislocation array reported in Mg-Gd alloy [153].

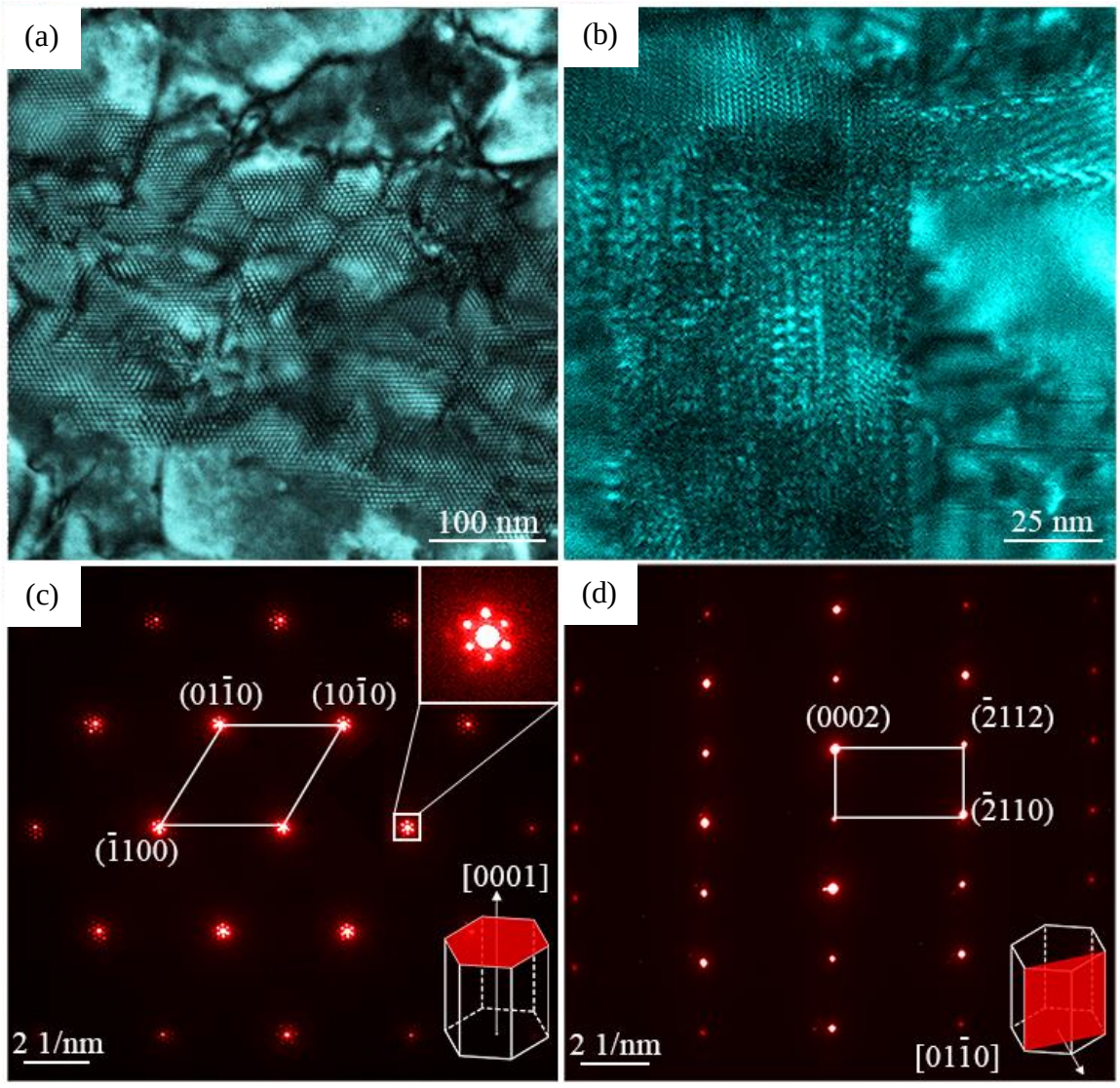

Figure 6.1 Hexagonal patterns near low-angle grain boundaries in Mg. (a) BF micrograph viewed along <c>-axis and (c) the corresponding diffraction patterns with additional six reflections around each Mg reflections; (b) BF micrograph and (d) the corresponding diffraction pattern viewed along <b>-axis.

6.2 <c>-screw Dislocation Arrays in Pure Mg

To clarify the nature of these hexagonal patterns, HRTEM images were taken on the patterned area as shown in Figure 6.2. Viewed along <c>-axis as shown in Figure 6.2 (a), a close inspection on the enlarged inset shown at the right upper corner reveals that the hexagonal patterns are actually comprised of light-dark contrast area at each hexagonal node, as indicated by the area enclosed by the red circle. Similar light-dark contrast has been repeatedly reported in samples containing edge-on screw dislocations [212, 213]. Theoretically, no visible contrast is expected to rise for end-on screw dislocations inside infinitely thick crystals, due to the fact that the atomic displacements of end-on screw dislocations are entirely parallel to the viewing direction. However, in our case of TEM observation, one deals with thin film with limited dimension along sample thickness. Such finite dimension introduces surface relaxation to the dislocation stored inside, causing in-plane displacement around the dislocation core (i.e., the so-called Eshelby twist [214]), responsible for the reported light-dark contrast of end-on screw dislocations [212, 213] [215, 216]. Additionally, the in-plane displacement caused by the Eshelby twist introduces observable ellipticity of atomic columns recorded in HRTEM images. These unique characteristics of screw dislocations make it possible to unambiguously confirm their existence in TEM samples.

To demonstrate that the patterned area is indeed comprised of end-on <c>-screw dislocations, an open-sourced Python library, “Atomap”, has been adopted to generate the ellipticity map of a light-and-dark spot inside the patterned area as shown in the HRTEM in the lower part of Figure 6.2 (b), the dislocation core locates at where the light and dark contrast meets and is marked by the red arrow. The corresponding ellipticity map shown in the upper part of Figure 6.2 (b) shows clear evidence of circular ellipticity of atomic columns around the dislocation core marked by the red arrow, exactly as predicted by the Eshelby twist. It is worth mentioning that most ellipticity maps are not symmetric around the dislocation core (e.g., the ellipticity map shown in Figure 6.2 (b) is stretching from lower left to upper right), in contrast to the theoretical symmetric configuration.

This is due to limited precision in peak finding of atomic columns which is subjected to influence from experimental factors like sample drifting during image acquisition and the quality of TEM samples.

Additional proof suggesting the existence of <c>-screw dislocations can be found along the perpendicular <b>-axis direction. As shown in Figure 6.2 (c), distorted (0001) atomic planes are clearly presented in the HRTEM micrograph, which resembles that of <c>-screw dislocations. Corresponding simulated HRTEM was calculated using the multi-slicing algorithm code developed by Kirkland [165], based on an atomic model consisting of <c>-screw dislocation dipole arrays. The simulated image is overlapped on the left part of the experimental micrograph shown in Figure 6.2 (c), showing fairly good agreement with the experimental dislocation cores (indicated by the red arrows). The consistency between HRTEM images acquired from two perpendicular directions indicates that the observed hexagonal patterns are indeed comprised of <c>-screw dislocation dipoles.

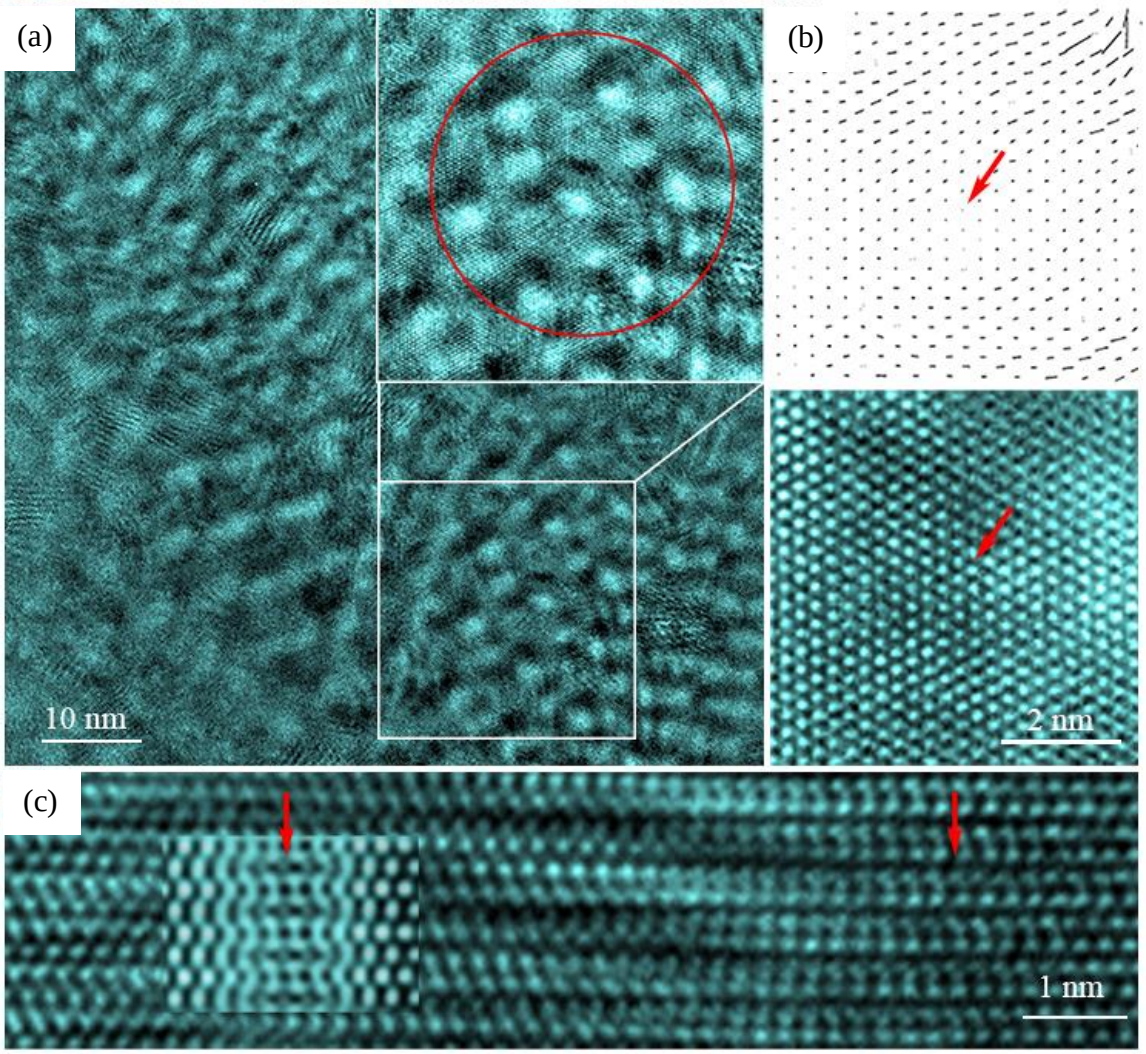

Figure 6.2 Atomistic structures of hexagonal patterns. (a) Hexagonal patterns viewed along <c>-axis, the rectangular area is enlarged in the upper right inset. (b) HRTEM micrograph and corresponding ellipticity map, showing circular ellipticity around an end-on <c>-screw dislocation core; (c) The experimental HRTEM micrograph and its overlapped simulation counterpart viewed along the <b>-axis, demonstrating the distorted (0001) atomic planes, dislocation cores are indicated by red arrows.

Based on this conclusion, we constructed an atomic model consisting of patterned <c>-screw dislocation dipoles with symmetric boundary conditions. One remaining problem is the origin of the hexagonal satellite spots around Mg reflections, accordingly, a diffraction pattern simulation algorithm proposed by Coleman et al. [173] was adopted to generate simulated diffraction patterns based on the constructed model, in order to check if these satellite reflections can be explained by the <c>-screw dislocation array theory. This algorithm uses a modified kinematic diffraction theory approach where a discrete reciprocal mess is used to capture any change in the reciprocal lattice

from which the diffraction pattern is generated. Due to the fact that the kinematic diffraction theory inherently considers the atomic position of all atoms contributing to diffraction, this algorithm can naturally reproduce minor changes in diffraction patterns caused by atomic displacement which in our case originates from dislocations. To better visualize the atomic model used for diffraction pattern simulation, shown in Figure 6.3 (a), atoms in the model are color-code based on their displacement from perfect lattice position along the <c>-axis, which is a key characteristic of <c>-screw dislocations. The corresponding simulated diffraction pattern is shown in Figure 6.3 (b), similar to the experimental pattern shown in Figure 6.1 (c), satellite reflections showing hexagonal symmetry can be found around each Mg $\{10\bar{1}0\}$ reflection. The additional intensity seen in the simulated pattern is caused by the finite size of the simulation box which causes elongated relrods, a phenomenon well-known for diffraction from crystals with finite dimensions [138, 173].

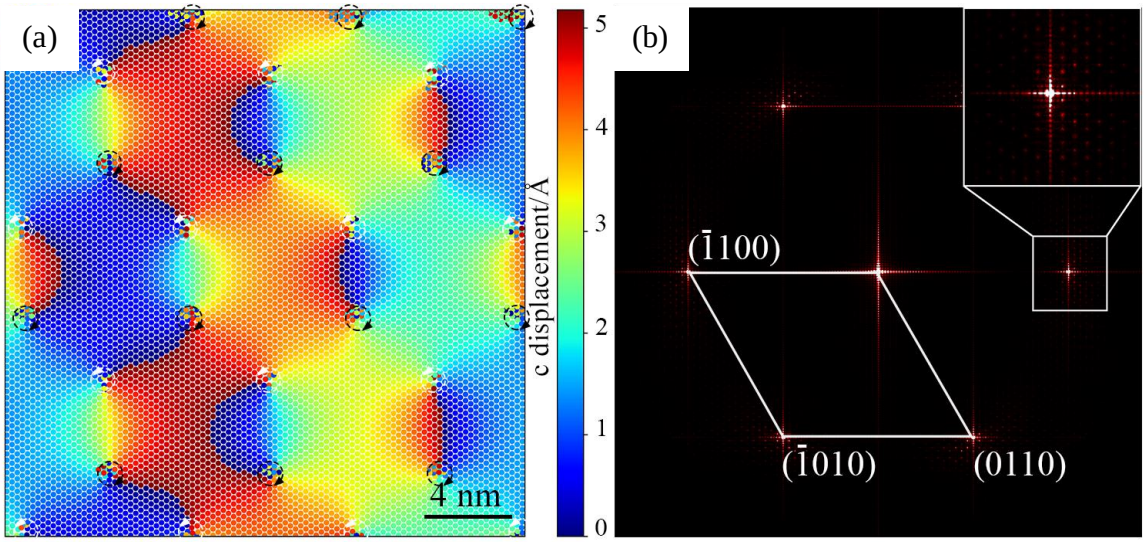

Figure 6.3 Atomic model of self-patterned dislocations. (a) A map of the atomic displacement along the <c>-axis, the viewing direction is [0001] (i.e., <c>-axis), black and white dashed circles represent indicate the position of dislocations with opposite signs, (b) the corresponding simulated SAED, showing similar six extra reflections around each main reflection.

6.3 Ordered Structure or Projection Artifacts

Though all the above analysis based on both real-space and reciprocal space information gives consistent agreement that the hexagonal pattern found in the current study is comprised of <c>-

screw dislocation array, one may argue that a similar hexagonal pattern or the satellite pattern may originate from simple projection artifacts during TEM observation. As all TEM micrographs are projected images, this kind of ambiguity in projections commonly confuses TEM analysis, making the interpretation of some TEM images less straightforward. The most commonly encountered one is probably the so-called "Moiré patterns" where additional artifacts showing periodical structures appear from the overlapping of two crystals with similar lattice constants [138]. It has been already well-established in the literature that it is theoretically possible to generate periodical structure in TEM images and corresponding satellite reflections by introducing double diffraction effects, instead of coming from real ordered structures. For instance, twist grain boundaries, where two grains with a certain mis-orientation stack over each other, are also capable of producing periodical "Moiré patterns" along with similar satellite spots seen as in our case [217, 218]. However, in addition to the evidence discussed previously, it can be shown that the possibility of twist grain boundaries as the origin of current experimental results can be further excluded by careful analysis on the nature of the low-angle grain boundary where the patterns are located and the diffraction pattern with extra satellite reflections.

One important characteristic of the previously reported <c>-screw dislocation array found in Mg-Gd binary alloys is that these structures always locate at low-angle tilt grain boundaries [153], as shown in Figure 6.4 (a-c). In the current study, the same features have been found for hexagonal patterns in pure Mg as shown in Figure 6.4 (d-e). Taking patterns in pure Mg shown in Figure 6.4 (e) as examples, it has been found by Burgers' loop analysis that the low-angle grain boundary consists of a row of periodically spaced dislocations with edge-<a> component (i.e., $1/3<11\bar{2}0>$), as indicated by the yellow arrows. Meanwhile, other patterned area away from the grain boundary shows no opening of the Burgers' loop, indicating no edge component for any dislocations in these areas. The nature of tilting grain boundaries predicts that the mis-orientation (i.e., tilting angle) between two adjacent grains is determined by the spacing of edge dislocations at the grain

boundaries [138]. And identical to what has been shown in ref. [153], the mis-orientation of the grain boundary at which the hexagonal patterns locate can be attributed entirely to the edge <a> dislocation components revealed by the Burgers' loop analysis. That is to say, the grain boundaries where the hexagonal patterns locate are pure tilt grain boundaries. Since both the formation of "Moiré patterns" and the occurrence of double diffraction requires overlapping crystals which can only be achieved through twist grain boundary, this essentially excludes the "Moiré patterns" interpretation of the hexagonal patterns.

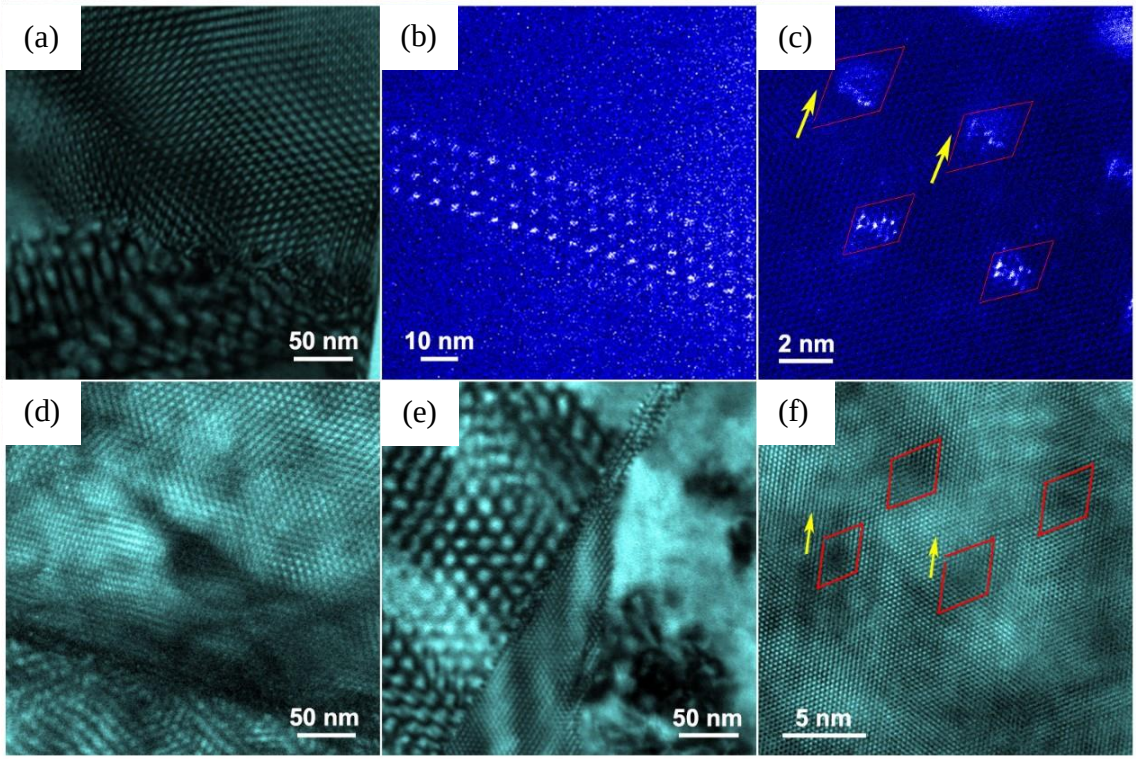

Figure 6.4 Hexagonal patterns located at low-angle tilt grain boundaries. (a-c) are in Mg-Gd alloys, adopted from ref. [153] and (d-f) are in pure Mg. (a) TEM image showing the edge of the hexagonal pattern. The interspacing of <15 nm suggests dislocation patterns while the interspacing of >20nm is likely because of twist boundaries (artifacts from "Moiré patterns"); (b) scanning transmission electron microscopy (STEM)-HAADF image showing the Gd segregations at dislocation patterns (Z-contrast imaging, with Gd shown as bright dots). It should be noted that well-formed Gd segregations were recorded in Mg-Gd alloys with a post heat-treatment at 200-300 °C while dislocation patterns were found in as-deformation Mg-Gd alloys [153]. (c) STEM-HAADF image showing that the dislocation pattern has a dislocation array with the edge component. Identified Burgers vectors of 1/3<11$\bar{2}$0> are labeled by arrows. (d-e) TEM images showing the edge of hexagonal patterns (with an interspacing of <15 nm, top part in (a) and right part in (d)). (f) HRTEM image taken at the edge of the hexagonal pattern, showing an array of edge dislocations with identified Burgers vector of 1/3<11$\bar{2}$0>.

As mentioned earlier, double diffraction from two overlapping crystals, as in the case of twist grain boundaries, can produce similar satellite reflections to what is shown in Figure 6.1 (c). If we consider a 3^{o} twist grain boundary and allow the six innermost reflections ($\{10\bar{1}0\}$) of the [0001] zone to contribute double diffraction process (which is reasonable, because the intensity of high order diffractions quickly fades away, thus has limited impact on double diffraction), a similar pattern with satellite reflections showing hexagonal symmetry can indeed be generated, as shown in Figure 6.5 (a). However, one key characteristic of such double-diffracted pattern is that there are always two sets of strong reflections coming from the upper and lower crystals which are color-coded into red and black in Figure 6.5 (a), respectively. Such features have been reported for satellite reflections caused by overlapping crystals [219], as shown in Figure 6.5 (c, d). Additionally, another key feature of the double-diffracted pattern is its asymmetry showing the "rotation-like" feature of the satellite spots, note how the intensity distribution of the six satellites shifts around, as marked by the red ellipses in both simulated and experimental images shown in Figure 6.5 (a, b). These features of the diffraction pattern are, however, totally absent in our experimental diffraction pattern shown in Figure 6.1 (c). Therefore, even if the grain boundary at which the patterns locate is a twist boundary in nature, which is unlikely based on the previous discussion, it still cannot correctly reproduce the same experimental pattern obtained in the current study.

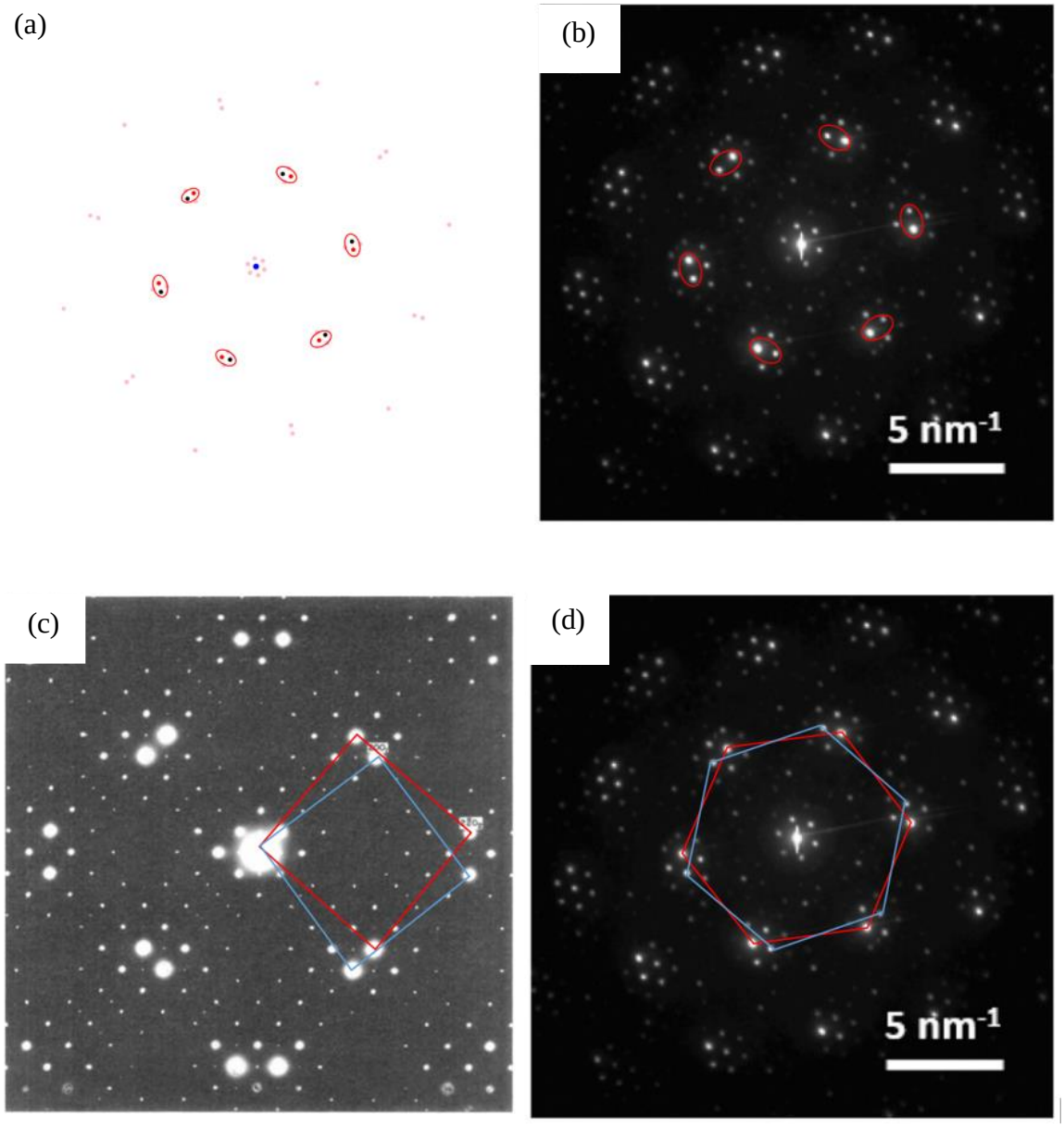

Figure 6.5 Intensity analysis on the satellite diffraction pattern caused by double-diffraction. (a)Simulated diffraction pattern of a 3º twist boundary allowing the inner most reflections for double diffraction, diffraction from upper crystal, lower crystal, and double diffraction are color-coded into red, black and pink; (b) experimental diffraction pattern of two overlapping crystals, main reflections are pointed out by red circle, reproduced from ref. [219]; (c, d) satellite spots resulting from double diffraction of twist boundary and two stacking crystals, reproduced from ref. [220] and ref. [219].

6.4 Formation Mechanism and Possible Potential of the <c>-screw Dislocation Arrays

Due to the rather low mobility of <c> dislocations originating from its large Burgers' vector, it is energetically unfavorable for <c> dislocations to directly move and self-assemble into the observed dislocation patterns. Accordingly, an alternative formation mechanism for the <c>-screw dislocation array observed in the current study has been proposed on the basis of dislocation interactions, as shown in Figure 6.6 (a-d). Pyramidal <c+a> slip becomes more active in Mg and its alloys when deformed at elevated temperature [221-223], <c+a> dislocations are consecutively generated during hot-compression, forming the low-angle grain boundaries where the patterns locate, the following <c+a> dislocations then pile-up which likely causes large stress concentration. Then due to such large stress concentration, the newly arriving <c+a> dislocations may cross-slip onto $\{1\bar{1}00\}$ prismatic planes and then dissociate into individual <c> and <a> dislocations. Due to the high mobility of <a> dislocations, the dissociated <a> dislocations quickly glide away and annihilate with another opposite signed <a> dislocations, leaving only <c> dislocations behind. Similar dissociation process of <c+a> dislocations has been proven possible under high stress using MD simulation [26], and also experimentally reported in deformed Mg [156, 157]. The <c> dislocation left on prismatic planes will then likely align along the <c>-direction due to the low line energy associated with a screw dislocation, and finally self-assemble into the observed hexagonal LEDS, in order to reduce the total strain energy.

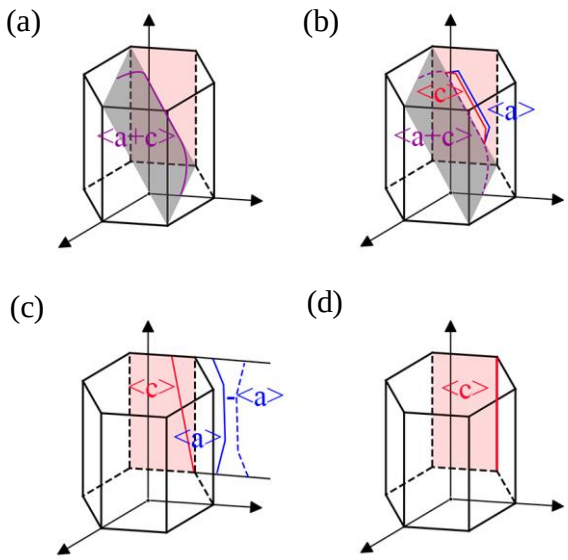

Figure 6.6 Proposed formation mechanism of self-patterning <c>-screw dislocation array. (a) <c+a> dislocation (marked by purple line) glides on pyramidal plane (pyramidal II {11$\bar{2}$2} plane as an example shown in the figure) and then a pure screw segment form on a {1$\bar{1}$00} prismatic plane, (b) the <c+a> dislocation on the prismatic plane dissociates into one <c> dislocation (marked by red line) and one <a> dislocation (marked by blue line), (c) the <a> dislocation glides easier than the <c> dislocation on prism plane, and can be annihilated with other <a> dislocations, (d) <c> dislocations become screw type to reduce the line energy, and are patterned due to elastic interaction.

Unlike "Taylor lattice" found in fatigued cubic materials, this new LEDS can be manufactured by simple hot-deformation, a much simpler and common practice compared to cyclic loading. Thanks to its special orientation (perpendicular to the easy gliding basal slip), this LEDS is expected to have a much higher work hardening effect due to more and stronger dislocation interaction with the easy gliding basal slip, leading to better strengthening. Additionally, such orientation also makes the chance of interaction with basal <a> slip higher than non-basal ones, leading to preferentially strengthening of basal slip. Naturally, the CRSS ratio between non-basal and basal slips can be reduced. As such high CRSS ratio is believed to be responsible for the poor ductility of Mg under room temperature, lots of research has shown by reducing it, the ductility of Mg can be significantly improved due to activation of more slip systems. For example, the addition of RE elements like Y can preferentially enhance basal slip more than non-basal ones, resulting in a significantly reduction in the CRSS ratio between basal and pyramidal II slip from ~100 in pure Mg to ~3 in Mg-0.1Y alloys [20]. Therefore, such LEDS shows good promise as an effective yet

easy-to-manufacture strengthening defect structure that likely improves both the strength and ductility of Mg and its alloy.

6.5 Conclusions

In this chapter, by using pure Mg as the model system, it has been demonstrated that through simple hot compression, periodical <c>-screw dislocation array, a promising effective strengthener for Mg and its alloy, can be manufactured without the presence of any solute elements. Key conclusions can be drawn as follows:

1. Combining HRTEM images and corresponding SAED patterns, it has been found that the hexagonal patterns obtained in current hot compressed samples are comprised of <c>-screw dislocations with alternating signs, similar to the "Taylor lattice" found in fatigued cubic materials;

2. The potential influence of solute elements structure has been decoupled and proven not essential to the formation of such dislocation, indicating its possible application to a wide range of alloy systems, though it may also serve as templates for periodical segregation as reported in ref. [153];

3. A possible formation mechanism for the <c>-screw dislocation arrays found in the current study has been proposed on the basis of cross-slip and dissociation of <a+c> dislocations which show enhanced activity during deformation at elevated temperature;

4. Due to its special configuration which intercepts perpendicularly with the easy-gliding basal slip, the <c>-screw dislocation array found in current study is promising in terms of improving both the strength and ductility of Mg and its alloys.

Our findings here might enlighten the design of new high-strength Mg alloy systems by introducing a new strengthening dislocation sub-structure.

Chapter 7 Summary and Future Works

7.1 Summary of the thesis

In this thesis, in order to reduce the addition of RE alloying elements used for manufacturing high-performance Mg alloys, a promising alternative solution, defects engineering, which exploits the defect structures naturally existing in real-world crystalline materials, is explored. Two strengthening defects structures, including excessive grain boundaries within nano-crystalline materials and a novel periodic dislocation structure, have been taken into account. The key findings obtained in the current study will be briefly summarized in the following part.

Starting with the idea of introducing an excessive amount of grain boundaries to essentially form nano-crystalline materials, which show many unique and superior mechanical properties compared to their coarse-grained counterparts, a new nano-crystalline synthesizing technique using simple mechanical polishing has been invented for the first time. By exploiting the mechanically induced SNC effect, such mechanical polishing based approach effectively combines nano-crystalline fabrication and TEM sample preparation into one single step. Nano-grained Mg-Gd binary with grain size ~114 nm were successfully prepared using this new polishing approach. Procedures for manufacturing such nano-crystalline wedge TEM sample that can be directly used for TEM observation has been described in detail. Understandably due to its surface treatment nature, TEM characterization on samples prepared out of materials with different initial microstructures revealed that the initial microstructure has no noticeable impact on the nano-crystalline formed in the prepared sample. The origin of the nano-crystalline in the current study is believed to be SPD introduced by the mechanical polishing process, which leads to rotational DRX responsible for the nano-crystallization, similar to the case in ASBs. Although it is quite remarkable that such fine nano-grains can be obtained by very low-speed polishing at room temperature, the possible reasons may be linked to the small size and the thin thickness of samples when the polishing is nearly

finished. Using the proposed mechanical polishing approach, a nano-crystalline TEM wedge sample can be easily prepared within less than 1 hour out of coarse-grained Mg-Gd binary alloys despite of its initial microstructure with a good success rate. Additionally, such preparation approach is likely applicable to other Mg alloy systems or other metals, considering its SPD nature and numerous success in fabricating nano-crystalline using SPD in various metals. Our findings here offer a simple, fast yet cost-effective way to manufacture nano-crystalline TEM samples by controlled mechanical polishing, no sophisticated equipment or additional preparation process are needed. This finding can be valuable to many researchers interested in nano-crystalline materials, as it offers a simple and versatile solution to the common problem in these studies as to how to manufacture the nano-crystalline samples in the first place.

With the nano-crystalline Mg-Gd sample manufactured, we turned to the long-standing controversy on the deformation mechanism of nano-crystalline with intermediate grain size to which the prepared nano-crystalline belongs. Trying to clarify the possible coupling between grain rotation and dislocation activity in intermediate-sized nano-crystalline, a new approach using HCDF imaging was proposed to track the grain/ slip planes re-orientation, as an improved technique to the conventional DF imaging used in past research. To demonstrate the feasibility of using HCDF imaging, several automation Python scripts have been written to simulate the HCDF contrast using a self-modified Multi-slicing algorithm. Simulation results suggest that as expected the contrast change in HCDF imaging is indeed directly linked to orientation changes and thus can be used to do the proposed tasks. HCDF imaging combined with in-situ TEM nano-indentation tests was then carried out to study in real-time the dynamic deformation process of the nano-crystalline used in the current study. Systematic TEM analysis shows that both grain rotation and dislocation activities operate actively during the deformation process. With further analysis on the indentation load-displacement curve and corresponding movie, it has been first experimentally demonstrated that a cooperative deformation mode involving both grain rotation and dislocation activity contributes to

the deformation process, leading to the "softening" phenomenon observed as the indentation proceeds. Along with proposing a better characterization technique for the study of nano-crystalline materials, our findings also offer new insights into the detailed deformation process of intermediate-sized nano-crystalline, possibly pushing the development of high-performance Mg alloys achieved by grain refining.

Apart from grain boundaries, another common defect, dislocations, has also been studied trying to maximize its strengthening effects. Unlike past research which focuses mostly on the density/distribution of dislocations, in this study we explored the possible impact of the type and configuration of dislocations. Starting with a novel hexagonal LEDS decorated with Gd segregation [153] which shows promising potential as an effective strengthener, we used pure Mg as the model system to decouple the possible effect of alloying elements from the formation of such dislocation structures. By using a similar hot deformation approach as reported in ref. [153], area with hexagonal patterns was obtained by simple uniaxial hot compression. To clarify the origin of such patterns, detailed HRTEM and SAED analyses were conducted combined with image/diffraction simulation. All experimental and simulation results indicate that the hexagonal patterns are comprised of <c>-screw dislocation dipoles, likely the same LEDS structure reported in ref. [153] but formed without the help of any alloying elements. The formation mechanism of such LEDS has also been tentatively discussed based on dislocation interactions. Due to its unique dislocation configuration, such LEDS not only promotes dislocation interactions causing more work hardening that improve the strength, it also likely selectively enhances the easy-gliding basal slip to reduce the CRSS ratio between non-basal and basal slip, thus contributing to the ductility of materials. Our findings here demonstrate the formation of such LEDS is independent of alloying elements and is thus likely available to a wide range of alloy systems, offering new insights into the design of high-performance Mg alloy.

7.2 Suggestions for Future Work

With the fast mechanical polishing method invented for nano-crystalline TEM sample preparation and HCDF imaging proposed for characterizing the deformation process of nano-crystalline materials, the future goal of this work should focus on two directions: first, on the sample preparation technique, a more detailed formation mechanism of the nano-crystalline found in the current study and the possible influencing preparation parameters should be further studied; second, although the cooperative deformation modes involving grain rotation and dislocation activity has been demonstrated in our sample, further study is still needed to clarify other potential deformation mechanisms like grain boundary sliding and partial dislocations, etc.

7.2.1 Understanding the formation mechanism of nano-crystalline and possible influencing preparation parameters.

Although nano-crystalline can be fabricated by the proposed mechanical polishing approach and the mechanical SNC phenomenon is attributed to its formation, how such fine nano-crystalline could form under current preparation conditions remains elusive, considering the much higher milling speed and temperature in the conventional SPD. Comparison experiments can be done by preparing wedge TEM samples using different polishing parameters, like applied loading, temperature, polishing speed, etc. Current experimental results suggest that the microstructures of prepared wedge TEM samples are not sensitive to the initial microstructure, but some inhomogeneous area with less defined nano-grains suggests that the microstructure of prepared samples can be tuned by different polishing parameters. As can be seen in Figure 7.1, it has been found that compared to samples prepared using brand new diamond sandpaper film, those prepared by used sandpapers, which likely have weaker abrasive powers, instead of well-defined nano-crystalline, areas with a high density of dislocation in the form of dislocation forest/cells can be observed throughout the sample. Apart from further supporting that these nano-crystalline are a

direct result of the mechanical polishing process, such difference indicates the possibility to tune the nano-crystalline by changing the polishing parameters.

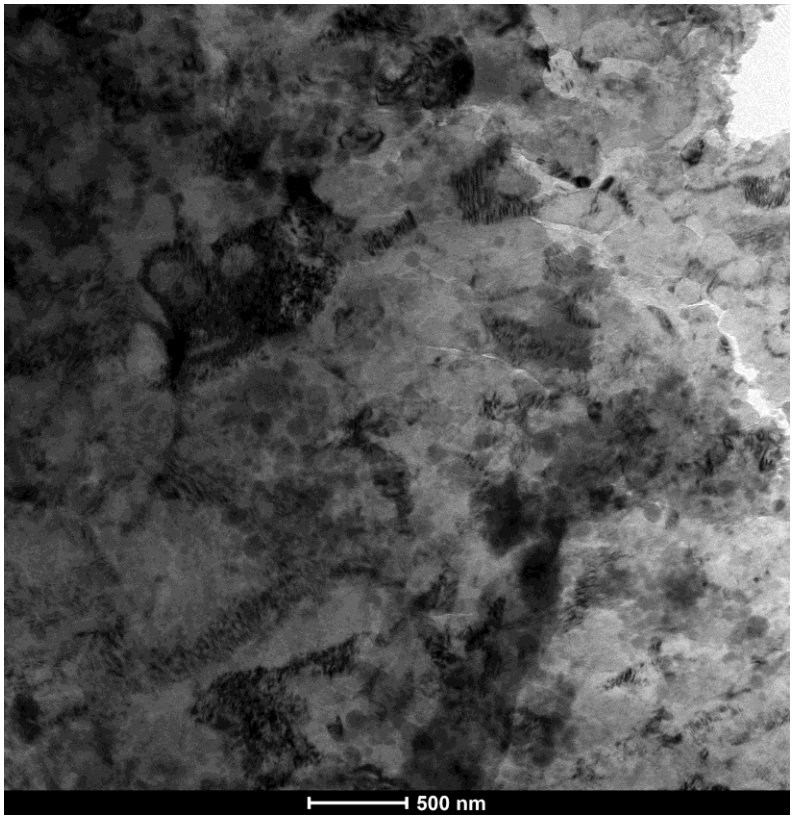

Figure 7.1 Wedge TEM sample prepared with used sandpapers, showing dislocation forest/cells instead of well-defined nano-crystalline.

It is still experimentally challenging to use coarse sandpapers to do the final polishing which forms the wedge for TEM observation, due to the fact that the higher removing ability of coarse sandpapers is easier to damage the thin tip. However, if the polishing parameters could be optimized in the future, it is promising that a range of microstructures with different grain sizes/dislocation densities could be manufactured using the mechanical polishing approach.

7.2.2 Study on Other Possible Deformation Mechanisms in the Deformation of Nano-crystalline Materials

It is well-known that as the grain size reduces, multiple additional deformation modes like partial dislocations, grain boundary sliding, grain boundary migration, etc. can be involved [135, 203, 224-

227], causing the rather complex deformation behavior of nano-grains which is still under debating. In this thesis, only dislocation activity and grain rotation have been taken into account. The possible coupling between grain rotation and grain boundary migration has been hinted by a few experimental results, more detailed study is necessary to understand such deformation process. HCDF imaging can potentially be used to study this process. While HCDF imaging in the current study gives valuable information on grain orientations, the size limitation of the aperture prevents individual analysis of different slip planes, due to their close d spacing. If a smaller aperture similar to what is used for nano-beam electron diffraction [228] could be used, tracking individual slip planes in real-time during in-situ nano-indentation tests can be possible. Grain boundary sliding, which is considered to play an important role in the deformation of nano-crystalline, likely took place in the indentation process of the current samples, but it can prove difficult to capture such sliding with conventional imaging approaches. Liu [229] has successfully captured the grain boundary sliding under SEM using a marker line approach. In future work, similar markers may be used to serve as references so that sliding can be simply revealed by the displacement of those reference lines.

7.2.3 Study the Impact of the Dislocation Arrays on the Deformation Process of Mg

As the periodical dislocation arrays have been successfully introduced in pure Mg, the next research plan on such structure is to study the deformation process of such structure using in-situ TEM. Although judging by its configuration, the dislocation structure found in the current study is likely superior in terms of strengthening, the absolute volume percentage of such structures in current samples is relatively small, making its contribution to the macro mechanical properties to be limited. Thus it is hard to investigate its real impact on the mechanical properties of Mg using macro mechanical testing techniques. To better understand the strengthening effects, we need to isolate the dislocation structure and do mechanical tests at specific areas where the dislocation structures locate. Considering the small scale of the dislocation structures and their defect nature, in-situ TEM

nano-indentation is well-suited for such study and will be used to characterize the deformation process and the possible influence on the mechanical properties of Mg in the future.

References

1. Chen, T.J., et al., *Effects of Zn content on microstructures and mechanical properties of Mg–Zn–RE–Sn–Zr–Ca alloys.* Materials Science and Engineering: A, 2014. **607**: p. 17-27.

2. Zhang, D., et al., *A high-strength low-rare-earth-alloyed magnesium alloy via traditional hot-extrusion*. Journal of Alloys and Compounds, 2019. **810**: p. 151967.

3. Sekar, P., Sanna, N., and Desai, V., *Enhancement of resistance to galvanic corrosion of ZE41 Mg alloy by equal channel angular pressing.* Materials and Corrosion, 2020. **71**(4): p. 571-584.

4. Kasprzak, W., et al., *Correlating Hardness Retention and Phase Transformations of Al and Mg Cast Alloys for Aerospace Applications.* Journal of Materials Engineering and Performance, 2015. **24**(3): p. 1365-1378.

5. Kulekci, M.K., *Magnesium and its alloys applications in automotive industry*. The International Journal of Advanced Manufacturing Technology, 2008. **39**(9): p. 851-865.

6. Pollock, T.M., *Weight Loss with Magnesium Alloys.* Science, 2010. **328**(5981): p. 986.

7. Canada, N. R. (2018, September 4). Government of Canada. Natural Resources Canada. Retrieved June 25, 2022, from https://www.nrcan.gc.ca/energy-efficiency/transportation-alternative-fuels/personal-vehicles/choosing-right-vehicle/tips-buying-fuel-efficient-vehicle/factors-affect-fuel-efficiency/vehicle-weight/21024.

8. Gupta, M. and Sharon, N., *Magnesium, Magnesium Alloys, and Magnesium Composites.* 2011: John Wiley & Sons.

9. Suzuki, M., et al., *Creep behavior and deformation microstructures of Mg–Y alloys at 550 K.* Materials Science and Engineering: A, 1998. **252**(2): p. 248-255.

10. Zhang, J., et al., *Microstructure and mechanical properties of an Mg-Zn-Zr alloy modified by rare earth of Erbium*, Materials Science Forum, 2009. **610-613**: p. 810-814.

11. Catar, R. and Altun, H., *Investigation of stress corrosion cracking behaviour of Mg-Al-Zn alloys in different pH environments by SSRT method.* Open Chemistry, 2019. **17**(1): p. 972-979.

12. Prabhu, T., *An overview of high-performance aircraft structural al alloy-AA7085.* Acta Metallurgica Sinica (English Letters), 2015. **28**(7): p. 909-921.

13. Guo, H., et al., *Microstructure and mechanical properties of cooled and tempered Cu and Nb-bearing ultra-low carbon steels*, Materials Science Forum, 2010. **638-642**: p. 3242-3247.

14. Zhao, D., *Activation and Suppression of Non-Basal Slip and Extension Twinning in Magnesium and Magnesium Alloys*, 2021, Texas A&M University.

15. Alaneme, K.K. and Okotete, E.A., *Enhancing plastic deformability of Mg and its alloys—A review of traditional and nascent developments.* Journal of Magnesium and Alloys, 2017. **5**(4): p. 460-475.

16. Zhang, J. and Joshi, S.P., *Phenomenological crystal plasticity modeling and detailed micromechanical investigations of pure magnesium.* Journal of the Mechanics and Physics of Solids, 2012. **60**(5): p. 945-972.

17. Akhtar, A. and Teghtsoonian, E., *Solid solution strengthening of magnesium single crystals—ii the effect of solute on the ease of prismatic slip.* Acta Metallurgica, 1969. **17**(11): p. 1351-1356.

18. Christian, J.W. and Mahajan, S., *Deformation twinning*. Progress in Materials Science, 1995. **39**(1): p. 1-157.

19. Fan, H., et al., *Temperature effects on the mobility of pyramidal <c+a>dislocations in magnesium.* Scripta Materialia, 2017. **127**: p. 68-71.

20. Wu, J., et al., *Study of basal< a> and pyramidal< c+ a> slips in Mg-Y alloys using micro-pillar compression*. Philosophical Magazine, 2020. **100**(11): p. 1454-1475.

21. Liu, S., et al., *Optimization in strength-ductility of heterogeneous Mg-13Gd alloy via small extrusion ratio combined with pre-aging*. Materials Science and Engineering A, 2022. **833**.

22. Guan, L., et al., *Activation of <c+a> slip and enhanced ductility in as-extruded Mg-Gd-Y-Nd alloys through Si addition.* Materials Science and Engineering A, 2021. **804**.

23. Sandlöbes, S., et al., *On the role of non-basal deformation mechanisms for the ductility of Mg and Mg-Y alloys.* Acta Materialia, 2011. **59**(2): p. 429-439.

24. Xu, J., et al., *Revealing the role of pyramidal <c+a> slip in the high ductility of Mg-Li alloy*. Journal of Magnesium and Alloys, 2021 (in press).

25. Zeng, Z.R., et al., *Effects of dilute additions of Zn and Ca on ductility of magnesium alloy sheet.* Materials Science and Engineering A, 2016. **674**: p. 459-471.

26. Wu, Z. and Curtin, W.A., *The origins of high hardening and low ductility in magnesium.* Nature, 2015. **526**(7571): p. 62-67.

27. Hu, W.W., Yang, Z.Q. and Ye, H.Q., *<c+a> dislocations and their interactions with other crystal defects in a Mg alloy.* Acta Materialia, 2017. **124**: p. 372-382.

28. Yang, Z., et al., *Direct observation of dislocation dissociation and Suzuki segregation in a Mg–Zn–Y alloy by aberration-corrected scanning transmission electron microscopy.* Acta Materialia, 2013. **61**(1): p. 350-359.

29. Luo, A.A., *Recent magnesium alloy development for elevated temperature applications.* International Materials Reviews, 2004. **49**(1): p. 13-30.

30. Xie, J., et al., *Towards developing Mg alloys with simultaneously improved strength and corrosion resistance via RE alloying*. Journal of Magnesium and Alloys, 2021. **9**(1): p. 41-56.

31. Imandoust, A., et al., *A review on the effect of rare-earth elements on texture evolution during processing of magnesium alloys.* Journal of Materials Science, 2017. **52**(1): p. 1-29.

32. Itoi, T., et al., *A high-strength Mg–Ni–Y alloy sheet with a long-period ordered phase prepared by hot-rolling.* Scripta Materialia, 2008. **59**(10): p. 1155-1158.

33. Rong, W., et al., *The role of bimodal-grained structure in strengthening tensile strength and decreasing yield asymmetry of Mg-Gd-Zn-Zr alloys.* Materials Science and Engineering: A, 2019. **740-741**: p. 262-273.

34. Zheng, L., et al., *Microstructures and mechanical properties of Mg–10Gd–6Y–2Zn–0.6Zr(wt.%) alloy*. Journal of Alloys and Compounds, 2011. **509**(35): p. 8832-8839.

35. Zhang, Z., et al., *Effects of phase composition and content on the microstructures and mechanical properties of high strength Mg–Y–Zn–Zr alloys.* Materials & Design, 2015. **88**: p. 915-923.

36. Yu, Z., et al., *Fabrication of a high strength Mg–11Gd–4.5Y–1Nd–1.5Zn–0.5Zr (wt%) alloy by thermomechanical treatments.* Materials Science and Engineering: A, 2015. **622**: p. 121-130.

37. Graedel, T.E., et al., *What Do We Know About Metal Recycling Rates?* Journal of Industrial Ecology, 2011. **15**(3): p. 355-366.

38. Yang, L., X. Li, and K. Lu, *Making Materials Plain: Concept, Principle and Applications.* Acta Metallurgica Sinica, 2017. **53**(11): p. 1413-1417.

39. Krivanek, O.L., et al., *Atom-by-atom structural and chemical analysis by annular dark-field electron microscopy.* Nature, 2010. **464**(7288): p. 571-574.

40. Meng, L., et al., *Dual-gated single-molecule field-effect transistors beyond Moore's law.* Nature Communications, 2022. **13**(1).

41. Hall, E.O., *The deformation and ageing of mild steel: III Discussion of results.* Proceedings of the Physical Society. Section B, 1951. **64**(9): p. 747-753.

42. Petch, N.J., *The Cleavage Strength of Polycrystals.* Journal of the Iron and Steel Institute, 1953. **174**: p. 25-28.

43. Yu, H., et al., *The mechanism for the high dependence of the Hall-Petch slope for twinning/slip on texture in Mg alloys.* Acta Materialia, 2017. **128**: p. 313-326.

44. Wang, J., et al., *Near-ideal theoretical strength in gold nanowires containing angstrom scale twins.* Nature Communications, 2013. **4**(1): p. 1742.

45. Wei, Y., et al., *Evading the strength–ductility trade-off dilemma in steel through gradient hierarchical nanotwins.* Nature Communications, 2014. **5**(1): p. 3580.

46. Cheng, Z., et al., *Extra strengthening and work hardening in gradient nanotwinned metals.* Science, 2018. **362**(6414).

47. Lu, L., et al., *Revealing the maximum strength in nanotwinned copper*. Science, 2009. **323**(5914): p. 607-610.

48. Ding, Q., et al., *Nano-twin-induced exceptionally superior cryogenic mechanical properties of a Ni-based GH3536 (Hastelloy X) superalloy*. Materials Today Nano, 2021. **14**(100110). .

49. Baskaran, I., Narayanan, T., and Stephen, A., *Pulsed electrodeposition of nanocrystalline Cu–Ni alloy films and evaluation of their characteristic properties.* Materials Letters, 2006. **60**(16): p. 1990-1995.

50. Wasekar, N.P., et al., *Pulsed electrodeposition and mechanical properties of Ni-W/SiC nano-composite coatings.* Materials & Design, 2016. **112**: p. 140-150.

51. Lee, J., et al., *Tuning the crystallinity of thermoelectric Bi2Te3nanowire arrays grown by pulsed electrodeposition.* Nanotechnology, 2008. **19**(36): p. 365701.

52. Ando, D., Koike, J., and. Sutou Y., *Relationship between deformation twinning and surface step formation in AZ31 magnesium alloys.* Acta Materialia, 2010. **58**(13): p. 4316-4324.

53. Koike, J., et al., *The activity of non-basal slip systems and dynamic recovery at room temperature in fine-grained AZ31B magnesium alloys.* Acta Materialia, 2003. **51**(7): p. 2055-2065.

54. Schioøtz, J. and Jacobsen K.W., *A maximum in the strength of nanocrystalline copper*. Science, 2003. **301**(5638): p. 1357-1359.

55. Sokol, M., et al., *An inverse Hall-Petch relation in nanocrystalline MgAl2O4 spinel consolidated by high pressure spark plasma sintering (HPSPS).* Scripta Materialia, 2017. **139**: p. 159-161.

56. Giga, A., et al., *Demonstration of an inverse Hall-Petch relationship in electrodeposited nanocrystalline Ni-W alloys through tensile testing.* Scripta Materialia, 2006. **55**(2): p. 143-146.

57. Nabarro, F.R.N., Basinski, Z.S., and Holt, D.B., *The plasticity of pure single crystals.* Advances in Physics, 1964. **13**(50): p. 193-323.

58. Faria, C.G., et al., *Increasing the work hardening capacity of equal channel angular pressed (ECAPed) aluminum through multi-axial compression (MAC).* Materials Letters, 2016. **174**: p. 153-156.

59. Das, D. and Chattopadhyay, P.P., *Influence of martensite morphology on the work-hardening behavior of high strength ferrite–martensite dual-phase steel.* Journal of Materials Science, 2009. **44**(11): p. 2957-2965.

60. Park, K.T., et al., *Thermal stability and mechanical properties of ultrafine grained low carbon steel.* Materials Science and Engineering: A, 2000. **293**(1): p. 165-172.

61. Jia, D., et al., *Deformation behavior and plastic instabilities of ultrafine-grained titanium.* Applied Physics Letters, 2001. **79**(5): p. 611-613.

62. Song, R., et al., *Overview of processing, microstructure and mechanical properties of ultrafine grained bcc steels.* Materials Science and Engineering: A, 2006. **441**(1): p. 1-17.

63. Wang, Y.M. and Ma, E., *Three strategies to achieve uniform tensile deformation in a nanostructured metal.* Acta Materialia, 2004. **52**(6): p. 1699-1709.

64. Fang, T.H., et al., *Revealing Extraordinary Intrinsic Tensile Plasticity in Gradient Nano-Grained Copper.* Science, 2011. **331**(6024): p. 1587-1590.

65. Lavrentev, F.F., *The type of dislocation interaction as the factor determining work hardening.* Materials Science and Engineering, 1980. **46**(2): p. 191-208.

66. Lavrentev, F.F. and Pokhil, Y.A., *Relation of dislocation density in different slip systems to work hardening parameters for magnesium crystals.* Materials Science and Engineering, 1975. **18**(2): p. 261-270.

67. Hansen, N. and Kuhlmann-Wilsdorf, D., *Low energy dislocation structures due to unidirectional deformation at low temperatures.* Materials Science and Engineering, 1986. **81**: p. 141-161.

68. Hughes, D.A., *Microstructural evolution in a non-cell forming metal: Al-Mg.* Acta Metallurgica et Materialia, 1993. **41**(5): p. 1421-1430.

69. Neumann, P., *Low energy dislocation configurations: A possible key to the understanding of fatigue.* Materials Science and Engineering, 1986. **81**: p. 465-475.

70. Ma, B.T. and Laird, C., *Dislocation structures of copper single crystals for fatigue tests under variable amplitudes.* Materials Science and Engineering: A, 1988. **102**(2): p. 247-258.

71. An, D. and Zaefferer, S., *Formation mechanism of dislocation patterns under low cycle fatigue of a high-manganese austenitic TRIP steel with dominating planar slip mode.* International Journal of Plasticity, 2019. **121**: p. 244-260.

72. Taylor, G.I., *The mechanism of plastic deformation of crystals. Part I.—Theoretical.* Proceedings of the Royal Society A, 1934. **145**(855): p. 362-387.

73. Kuhlmann-Wilsdorf, D., *Theory of plastic deformation: - properties of low energy dislocation structures.* Materials Science and Engineering: A, 1989. **113**: p. 1-41.

74. Mughrabi, H., *Microscopic Mechanisms of Metal Fatigue*, in *Strength of Metals and Alloys*, Strength of Metals and Alloys: Proceedings of the 5th International Conference, Aachen, Federal Republic of Germany, 1979. **3**: p. 1615-1638.

75. Liu, H., et al., *Guided Self-Assembly of Nano-Precipitates into Mesocrystals.* Scientific Reports, 2015. **5** (16530).

76. Gleiter, H., *Nanocrystalline materials.* Progress in Materials Science, 1989. **33**(4): p. 223-315.

77. Lu, K., *Stabilizing nanostructures in metals using grain and twin boundary architectures.* Nature Reviews Materials, 2016. **1**(5): p. 1-13.

78. Tjong, S.C. and Chen, H., *Nanocrystalline materials and coatings.* Materials Science and Engineering: R: Reports, 2004. **45**(1): p. 1-88.

79. Fatemi, S.M., et al., *Alleviation of Mechanical Anisotropy in Ultrafine/Nano-grained AZ31 Magnesium Alloy.* Journal of Materials Engineering and Performance, 2018. **27**(8): p. 4270-4279.

80. Tang, W., et al., *Mechanical anisotropy and deep drawing behaviors of AZ31 magnesium alloy sheets produced by unidirectional and cross rolling.* Journal of Materials Processing Technology, 2015. **215**: p. 320-326.

81. Suh, J., et al., *Enhanced mechanical behavior and reduced mechanical anisotropy of AZ31 Mg alloy sheet processed by ECAP.* Materials Science and Engineering: A, 2016. **650**: p. 523-529.

82. Figueiredo, R.B. and Langdon, T.G., *Grain refinement and mechanical behavior of a magnesium alloy processed by ECAP.* Journal of Materials Science, 2010. **45**(17): p. 4827-4836.

83. Lin, H.K., Huang, J.C., and Langdon, T.G., *Relationship between texture and low temperature superplasticity in an extruded AZ31 Mg alloy processed by ECAP.* Materials Science and Engineering A, 2005. **402**(1-2): p. 250-257.

84. Yi, S., et al., *Mechanical anisotropy and deep drawing behaviour of AZ31 and ZE10 magnesium alloy sheets.* Acta Materialia, 2010. **58**(2): p. 592-605.

85. Barnett, M., et al., *Influence of grain size on the compressive deformation of wrought Mg–3Al–1Zn.* Acta Materialia, 2004. **52**(17): p. 5093-5103.

86. Chino, Y., et al., *Mechanical anisotropy due to twinning in an extruded AZ31 Mg alloy.* Materials Science and Engineering A, 2008. **485**(1-2): p. 311-317.

87. Chao, Q., et al., *Nanoparticle-mediated ultra grain refinement and reinforcement in additively manufactured titanium alloys.* Additive Manufacturing, 2021. **46**: p. 102173.

88. Martin, J.H., et al., *Grain refinement mechanisms in additively manufactured nano-functionalized aluminum.* Acta Materialia, 2020. **200**: p. 1022-1037.

89. Croteau, J.R., et al., *Microstructure and mechanical properties of Al-Mg-Zr alloys processed by selective laser melting.* Acta Materialia, 2018. **153**: p. 35-44.

90. Karakulak, E., *A review: Past, present and future of grain refining of magnesium castings.* Journal of Magnesium and Alloys, 2019. **7**(3): p. 355-369.

91. Li, P., Tang, B., and Kandalova, E.G., *Microstructure and properties of AZ91D alloy with Ca additions.* Materials Letters, 2005. **59**(6): p. 671-675.

92. Hirai, K., et al., *Effects of Ca and Sr addition on mechanical properties of a cast AZ91 magnesium alloy at room and elevated temperature.* Materials Science and Engineering: A, 2005. **403**(1): p. 276-280.

93. Yu, W., et al., *Existing form and effect of zirconium in pure Mg, Mg-Yb, and Mg-Zn-Yb alloys.* Rare Metals, 2009. **28**(3): p. 289-296.

94. Pryds, N. and Huang, X. *The effect of cooling rate on the microstructures formed during solidification of ferritic steel.* Metallurgical and Materials Transactions A, 2000. **31**(12): p. 3155-3166.

95. Motegi, T., *Grain-refining mechanisms of superheat-treatment of and carbon addition to Mg–Al–Zn alloys.* Materials Science and Engineering: A, 2005. **413**: p. 408-411.

96. Li, M., Tamura, T., and Miwa, K., *Controlling microstructures of AZ31 magnesium alloys by an electromagnetic vibration technique during solidification: From experimental observation to theoretical understanding.* Acta Materialia, 2007. **55**(14): p. 4635-4643.

97. Tsuji, N., et al., *Ultra-fine grained bulk steel produced by accumulative roll-bonding (ARB) process.* Scripta Materialia, 1999. **40**(7): p. 795-800.

98. Frazier, W.E., *Metal additive manufacturing: A review.* Journal of Materials Engineering and Performance, 2014. **23**(6): p. 1917-1928.

99. Raghavan, N., et al., *Localized melt-scan strategy for site specific control of grain size and primary dendrite arm spacing in electron beam additive manufacturing.* Acta Materialia, 2017. **140**: p. 375-387.

100. Du, J., et al., *Improvement of grain refining efficiency for Mg–Al alloy modified by the combination of carbon and calcium.* Journal of Alloys and Compounds, 2009. **470**(1): p. 134-140.

101. Cao, P., Qian, M., and StJohn D.H., *Native grain refinement of magnesium alloys.* Scripta Materialia, 2005. **53**(7): p. 841-844.

102. Shao, C.W., et al., *Improvement of low-cycle fatigue resistance in TWIP steel by regulating the grain size and distribution.* Acta Materialia, 2017. **134**: p. 128-142.

103. Zhang, B., et al., *Effects of calcium on texture and mechanical properties of hot-extruded Mg-Zn-Ca alloys.* Materials Science and Engineering A, 2012. **539**: p. 56-60.

104. Al-Zubaydi, A.S., et al., *Evolution of microstructure in AZ91 alloy processed by high-pressure torsion.* Journal of Materials Science, 2016. **51**(7): p. 3380-3389.

105. Kocich, R., et al., *Simulation and practical verification of ECAP of magnesium alloy AZ91.* Journal of Achievements in Materials and Manufacturing Engineering, 2006. **18**(1-2): p. 295-298.

106. Zhang, L., et al., *Surface nanocrystallization of Mg-3wt.% Li-6wt.% Al alloy by surface mechanical attrition treatment.* Materials Characterization, 2016. **120**: p. 124-128.

107. Tao, N., et al., *An investigation of surface nanocrystallization mechanism in Fe induced by surface mechanical attrition treatment.* Acta Materialia, 2002. **50**(18): p. 4603-4616.

108. Agnew, S.R., et al., *Microstructure and mechanical behavior of nanocrystalline metals.* Materials Science and Engineering A, 2000. **285**(1-2): p. 391-396.

109. Alexandrov, I.V. and Valiev, R.Z., *Developing of SPD processing and enhanced properties in bulk nanostructured metals.* Scripta Materialia, 2001. **44**(8-9): p. 1605-1608.

110. Furukawa, M., Horita, Z., and Langdon, T.G., *Developing ultrafine grain sizes using severe plastic deformation.* Advanced Engineering Materials, 2001. **3**(3): p. 121-125.

111. Lowe, T.C. and Valiev, R.Z., *Producing nanoscale microstructures through severe plastic deformation.* JOM, 2000. **52**(4): p. 27-28.

112. Valiev, R.Z. and Alexandrov, I.V., *Nanostructured materials from severe plastic deformation.* Nanostructured Materials, 1999. **12**(1): p. 35-40.

113. Valiev, R.Z., Islamgaliev, R.K., and Alexandrov, I.V., *Bulk nanostructured materials from severe plastic deformation.* Progress in Materials Science, 2000. **45**(2): p. 103-189.

114. Wang, C., et al., *Review on modified and novel techniques of severe plastic deformation.* Science China Technological Sciences, 2012. **55**(9): p. 2377-2390.

115. Lu, K. and Lu, J., *Surface nanocrystallization (SNC) of metallic materials-presentation of the concept behind a new approach.* Journal of Materials Science and Technology, 1999. **15**(3): p. 193-197.

116. Chen, B., et al., *A new approach of a gradient nanograined surface layer for Mg-3Al-1Zn alloy induced by SMRGT.* International Journal of Advanced Manufacturing Technology, 2018. **94**(5-8): p. 2659-2665.

117. Lu, K., *Making strong nanomaterials ductile with gradients: Microstructures that increase metal crystallite size from nanoscale with surface depth are both strong and ductile.* Science, 2014. **345**(6203): p. 1455-1456.

118. Sun, B.B., et al., *Artifacts induced in metallic glasses during TEM sample preparation.* Scripta Materialia, 2005. **53**(7): p. 805-809.

119. Zhong, X., et al., *Comparing Xe^+pFIB and Ga^+FIB for TEM sample preparation of Al alloys: Minimising FIB-induced artefacts.* Journal of Microscopy, 2021. **282**(2): p. 101-112.

120. Kang, J.H. and Kim, S.H., *Sample preparation for EBSD analysis: Tips for metals with delicate surfaces.* Journal of Korean Institute of Metals and Materials, 2010. **48**(8): p. 730-740.

121. Koch, C.C., et al., *Ductility of nanostructured materials.* MRS Bulletin, 1999. **24**(2): p. 54-58.

122. Zhang, X., et al., *Modulated oscillatory hardening and dynamic recrystallization in cryomilled nanocrystalline Zn.* Acta Materialia, 2002. **50**(16): p. 3995-4004.

123. Alizadeh, R., et al., *Superplasticity of a nano-grained Mg–Gd–Y–Zr alloy processed by high-pressure torsion.* Materials Science and Engineering: A, 2016. **651**: p. 786-794.

124. Wang, L., et al., *Transmission electron microscopy observations of dislocation annihilation and storage in nanograins.* Applied Physics Letters, 2011. **98**(5): p. 051905.

125. Zhang, J., et al., *On the deformation-induced grain rotations in gradient nano-grained copper based on molecular dynamics simulations.* Nanotechnology Reviews, 2021. **10**(1): p. 87-98.

126. Chen, B., et al., *Grain rotation in plastic deformation.* Quantum Beam Science, 2019. **3**(3).

127. Liu, C., et al., *A cooperative nano-grain rotation and grain-boundary migration mechanism for enhanced dislocation emission and tensile ductility in nanocrystalline materials.* Materials Science and Engineering A, 2019. **756**: p. 284-290.

128. Gutkin, M.Y., Ovid'ko, I., and Pande, C., *Theoretical models of plastic deformation processes in nanocrystalline materials.* Reviews on Advanced Materials Science, 2001. **2**(1): p. 80-102.

129. Alekseeva, S., et al., *Grain boundary mediated hydriding phase transformations in individual polycrystalline metal nanoparticles.* Nature Communications, 2017. **8**(1): p. 1084.

130. Dingley, D.J., *Orientation imaging microscopy for the transmission electron microscope.* Microchimica Acta, 2006. **155**(1): p. 19-29.

131. Wu, G. and Zaefferer, S., *Advances in TEM orientation microscopy by combination of dark-field conical scanning and improved image matching.* Ultramicroscopy, 2009. **109**(11): p. 1317-1325.

132. Liu, H., et al., *Three-dimensional orientation mapping in the transmission electron microscope.* Science, 2011. **332**(6031): p. 833-834.

133. Kumar, V., *Orientation imaging microscopy with optimized convergence angle using CBED patterns in TEMs.* IEEE transactions on image processing, 2013. **22**(7): p. 2637-2645.

134. Rauch, E., et al., *Automatic crystal orientation and phase mapping in TEM by precession diffraction*. Microscopy and Analysis, 2008. **128**: p. S5-S8.

135. Ke, M., et al., *Observation and measurement of grain rotation and plastic strain in nanostructured metal thin films.* Nanostructured Materials, 1995. **5**(6): p. 689-697.

136. Zhang, Y., G.J. Tucker, and J.R. Trelewicz, *Stress-assisted grain growth in nanocrystalline metals: Grain boundary mediated mechanisms and stabilization through alloying.* Acta Materialia, 2017. **131**: p. 39-47.

137. Wang, Y.B., et al., *Deformation-induced grain rotation and growth in nanocrystalline Ni.* Applied Physics Letters, 2008. **92**(1): p. 011903.

138. Williams, D.B. and Carterc, C.B., *Transmission electron microscopy: A textbook for materials science*. 2009: Springer Science &Business Media.

139. Yao, B., et al., *Hollow-cone dark-field transmission electron microscopy for dislocation density characterization of trimodal Al composites.* Micron, 2011. **42**(1): p. 29-35.

140. Yao, B., et al., *High contrast hollow-cone dark field transmission electron microscopy for nanocrystalline grain size quantification*. Micron, 2010. **41**(3): p. 177-182.

141. Jin, M., et al., *Direct observation of deformation-induced grain growth during the nanoindentation of ultrafine-grained Al at room temperature.* Acta Materialia, 2004. **52**(18): p. 5381-5387.

142. El-Awady, J., *Unravelling the physics of size-dependent dislocation-mediated plasticity*. Nature Communication, 2015. **6**(1): p. 1-9.

143. Niewczas, M., et al., *Dislocation distribution and patterning in 〈a〉 -axis Mg single crystals during early compression.* Acta Materialia, 2019. **164**: p. 714-727.

144. Kamikawa, N., et al., *Strengthening mechanisms in nanostructured high-purity aluminium deformed to high strain and annealed.* Acta Materialia, 209. **57** (14): p. 4198-4208.

145. Shan, Z., et al., *Mechanical annealing and source-limited deformation in submicrometre-diameter Ni crystals.* Nature Materials, 2008. **7**(2): p. 115-119.

146. Van Der Merwe, J.H., Woltersdorf, J., and Jesser, W.A., *Low energy dislocation structures in epitaxy.* Materials Science and Engineering, 1986. **81**: p. 1-33.

147. Holt, D.L., *Dislocation cell formation in metals.* Journal of Applied Physics, 1970. **41**(8): p. 3197-3201.

148. Neumann, P., *Low energy dislocation configurations: A possible key to the understanding of fatigue*. Materials Science and Engineering, 1986. **81**(C): p. 465-475.

149. Sohn, S.S., et al., *Novel ultra-high-strength (ferrite + austenite) duplex lightweight steels achieved by fine dislocation substructures (Taylor lattices), grain refinement, and partial recrystallization*. Acta Materialia, 2015. **96**: p. 301-310.

150. Su, H., et al., *Atomic-resolution investigations on formation and evolution of symmetric tilt grain boundaries near the {10$\bar{1}$2} twin orientation in a Mg alloy*. Scripta Materialia, 2020. **187**: p. 113-118.

151. Wang, R.M., Eliezer, A., and Gutman, E., *Microstructures and dislocations in the stressed AZ91D magnesium alloys.* Materials Science and Engineering A, 2003. **344**(1-2): p. 279-287.

152. Wang, F., et al., *⟨c+a⟩ dislocations in {10$\bar{1}$2} twins in Mg: A kinematic and energetic requirement.* Acta Materialia, 2020. **195**: p. 13-24.

153. Li, Y., et al., *Self-patterning Gd nano-fibers in Mg-Gd alloys.* Scientific Reports, 2016. **6**(1): p. 38537.

154. Lei, H., Chen, J., and Ruterana, P., *Role of c-screw dislocations on indium segregation in InGaN and InAlN alloys.* Applied Physics Letters, 2010. **96**(16): p. 161901.

155. Gutierrez-Urrutia, I. and Raabe, D., *Multistage strain hardening through dislocation substructure and twinning in a high strength and ductile weight-reduced Fe–Mn–Al–C steel*. Acta Materialia, 2012. **60**(16): p. 5791-5802.

156. Timofeev, V., Serebryany, V., and Zaliznyak, Y.., *Electron-microscopic study of the slip systems in an Mg-4.5% Al-1% Zn alloy*. Russian Metallurgy, 2008. **2008**(3): p. 266-269.

157. Xie, K.Y., et al., *Experimental observations of the mechanisms associated with the high hardening and low strain to failure of magnesium.* Materialia, 2019. **8**: p. 100504.

158. Nie, J.F. and Muddle, B., *Characterisation of strengthening precipitate phases in a Mg–Y–Nd alloy.* Acta Materialia, 2000. **48**(8): p. 1691-1703.

159. Ayache, J., et al., *Sample preparation handbook for transmission electron microscopy: techniques*. Vol. 2. 2010: Springer Science & Business Media.

160. Chen, J. and D.G. Ivey, *Preparation of metallized GaN/sapphire cross sections for TEM analysis using wedge polishing*. Micron, 2002. **33**(5): p. 489-492.

161. Li, H. and Salamanca-Riba, L., *The concept of high angle wedge polishing and thickness monitoring in TEM sample preparation.* Ultramicroscopy, 2001. **88**(3): p. 171-178.

162. Liu, B.Y., et al., *Large plasticity in magnesium mediated by pyramidal dislocations.* Science, 2019. **365**(6448): p. 73-75.

163. Widjaja, A., *Discrete dislocation modelling of Nano-and Micro-indentation*. 2007: University Library Groningen.

164. Pozsgai, I., *Mass thickness determination and microanalysis of thin films in the TEM—Revisite.* Ultramicroscopy, 2007. **68**(1): p. 69-75.

165. Kirkland, E.J., *Advanced computing in electron microscopy*. Vol. 12. 1998: Springer.

166. Rong, Y.H., *Introduction to Analytical Electron Microscopy* 2ed. 2014, China: Higher Education Press.

167. Roberson, M.D. and Raffel, K., *Imaging Crystals.* Microscopical Society of Canada Bulletin, 2008. **107**: p. 191-195.

168. MacArthur, K.E., et al., *Optimal ADF STEM imaging parameters for tilt-robust image quantification*. Ultramicroscopy, 2015. **156**: p. 1-8.

169. Lebeau, J.M., et al., *Standardless atom counting in scanning transmission electron microscopy.* Nano Letters, 2010. **10**(11): p. 4405-4408.

170. Rosenauer, A., et al. *Measurement of composition profiles in III-nitrides by quantitative scanning transmission electron microscopy*. *Journal of Physics: Conference Series*. 2010. **209** (012009).

171. Nord, M., et al., *Atomap: a new software tool for the automated analysis of atomic resolution images using two-dimensional Gaussian fitting.* Advanced Structural and Chemical Imaging, 2017. **3**(1).

172. Liu, X.Y., et al., *EAM potential for magnesium from quantum mechanical forces.* Modelling and Simulation in Materials Science and Engineering, 1996. **4**(3): p. 293.

173. Coleman, S.P., Sichani, M.M., and Spearot, D., *A computational algorithm to produce virtual X-ray and electron diffraction patterns from atomistic simulations.* JOM, 2014. **66**(3): p. 408-416.

174. Lee, S.B., Yoon, D.Y., and Henry, M.F., *Abnormal grain growth and grain boundary faceting in a model Ni-base superalloy.* Acta Materialia, 2000. **48**(12): p. 3071-3080.

175. Zhao, J., et al., *Influence of heat treatment on microstructure and mechanical properties of as-cast Mg–8Li–3Al–2Zn–xY alloy with duplex structure.* Materials Science and Engineering: A, 2016. **669**: p. 87-94.

176. Silva, R.P., et al., *Grain Refinement of Inconel 718 Superalloy—The Effect of Rotating Magnetic Field*. Materials, 2022. **15**(6).

177. Lu, K. and Lu, J., *Nanostructured surface layer on metallic materials induced by surface mechanical attrition treatment.* Materials Science and Engineering: A, 2004. **375-377**: p. 38-45.

178. Montross, C.S., et al., *Laser shock processing and its effects on microstructure and properties of metal alloys: a review.* International Journal of Fatigue, 2002. **24**(10): p. 1021-1036.

179. Xu, K., et al., *Surface nanocrystallization mechanism of a rare earth magnesium alloy induced by HVOF supersonic microparticles bombarding.* Applied Surface Science, 2009. **256**(3): p. 619-626.

180. Li, W.L., Tao, N.R., and Lu, K., *Fabrication of a gradient nano-micro-structured surface layer on bulk copper by means of a surface mechanical grinding treatment.* Scripta Materialia, 2008. **59**(5): p. 546-549.

181. Zhou, X., et al., *Atomistic simulations of the surface severe plastic deformation-induced grain refinement in polycrystalline magnesium: The effect of processing parameters.* Journal of Magnesium and Alloys, 2021. **10**(5): P. 1242-1255.

182. Turley, D. and Samuels, L., *The nature of mechanically polished surfaces of copper*. Metallography, 1981. **14**(4): p. 275-294.

183. Sun, H., et al., *Plastic strain-induced grain refinement in the nanometer scale in a Mg alloy.* Acta Materialia, 2007. **55**(3): p. 975-982.

184. Yoo, M., et al., *Non-basal slip systems in HCP metals and alloys: source mechanisms.* Materials Science and Engineering: A, 2001. **319**: p. 87-92.

185. Huang, J.Y., et al., *Microstructures and dislocation configurations in nanostructured Cu processed by repetitive corrugation and straightening.* Acta Materialia, 2001. **49**(9): p. 1497-1505.

186. Tao, N.R., et al., *An investigation of surface nanocrystallization mechanism in Fe induced by surface mechanical attrition treatment.* Acta Materialia, 2002. **50**(18): p. 4603-4616.

187. Wu, X., et al., *Microstructure and evolution of mechanically-induced ultrafine grain in surface layer of AL-alloy subjected to USSP.* Acta Materialia, 2002. **50**(8): p. 2075-2084.

188. Zhu, L., et al., *Dynamic precipitation in Mg–8.08 Gd–2.41 Sm–0.30 Zr alloy during hot compression*. Materials, 2018. **11**(11): p. 2147.

189. Tartaglino, U. and Tosatti, E., *Strain effects at solid surfaces near the melting point.* Surface Science, 2003. **532-535**: p. 623-627.

190. Cairns, J.H., et al., *Structure and mechanical properties of heavily deformed copper.* Journal of the Institute of Metals, 1971. **99**: p. 93-97.

191. Nutting, J., *The deformation of metals to high strains by cold working.* Proceedings of the Eighth International Conference on Electron Microscopy, 1974. **1**: p. 580-581.

192. Jo, M.C., et al., *Understanding of adiabatic shear band evolution during high-strain-rate deformation in high-strength armor steel.* Journal of Alloys and Compounds, 2020. **845**: p. 155540.

193. Yang, Y., et al., *Microstructural characterization and evolution mechanism of adiabatic shear band in a near beta-Ti alloy*. Materials Science and Engineering: A, 2011. **528**(6): p. 2787-2794.

194. Derby, B., *The dependence of grain size on stress during dynamic recrystallisation.* Acta Metallurgica et Materialia, 1991. **39**(5): p. 955-962.

195. Meyers, M.A., et al., *Microstructural evolution in adiabatic shear localization in stainless steel*. Acta Materialia, 2003. **51**(5): p. 1307-1325.

196. Rzychoń, T. and Kiełbus, A., *The influence of rare earth, strontium and calcium on the thermal diffusivity of Mg-Al alloys*. Defect and Diffusion Forum. 2011. **312-315**: P. 824-829.

197. Meyers, M.A., et al., *Shear localization in dynamic deformation of materials: microstructural evolution and self-organization*. Materials Science and Engineering: A, 2001. **317**(1): p. 204-225.

198. Upmanyu, M., et al., *Simultaneous grain boundary migration and grain rotation.* Acta Materialia, 2006. **54**(7): p. 1707-1719.

199. Wang, L., et al., *Grain rotation mediated by grain boundary dislocations in nanocrystalline platinum.* Nature Communications, 2014. **5**.

200. Wang, L., et al., *Tracking the sliding of grain boundaries at the atomic scale.* Science, 2022. **375**(6586): p. 1261-1265.

201. Shan, Z., et al., *Grain boundary-mediated plasticity in nanocrystalline nickel.* Science, 2004. **305**(5684): p. 654-657.

202. Theocaris, P.S., *Moiré Fringes in Strain Analysis: The Commonwealth and International Library: Applied Mechanics Division*. 2017: Elsevier.

203. Hasnaoui, A., Van Swygenhoven ,H., and Derlet, P., *Cooperative processes during plastic deformation in nanocrystalline fcc metals: A molecular dynamics simulation*. Physical Review B, 2002. **66**(18): p. 184112.

204. Lohmiller, J., et al., *Untangling dislocation and grain boundary mediated plasticity in nanocrystalline nickel.* Acta Materialia, 2014. **65**: p. 295-307.

205. Liu, C., et al., *A cooperative nano-grain rotation and grain-boundary migration mechanism for enhanced dislocation emission and tensile ductility in nanocrystalline materials.* Materials Science and Engineering: A, 2019. **756**: p. 284-290.

206. Haslam, A.J., et al., *Stress-enhanced grain growth in a nanocrystalline material by molecular-dynamics simulation*. Acta Materialia, 2003. **51**(7): p. 2097-2112.

207. Haslam, A.J., et al., *Mechanisms of grain growth in nanocrystalline fcc metals by molecular-dynamics simulation*. Materials Science and Engineering: A, 2001. **318**(1): p. 293-312.

208. Livingston, J.D. and Chalmers, B., *Multiple slip in bicrystal deformation*. Acta Metallurgica, 1957. **5**(6): p. 322-327.

209. Shen, Z., Wagoner, R.H., and Clark, W., *Dislocation pile-up and grain boundary interactions in 304 stainless steel*. Scripta Metallurgica, 1986. **20**(6): p. 921-926.

210. Shen, Z., Wagoner, R.H., and Clark, W., *Dislocation and grain boundary interactions in metals.* Acta Metallurgica, 1988. **36**(12): p. 3231-3242.

211. Spearot, D.E. and Sangid, M.D., *Insights on slip transmission at grain boundaries from atomistic simulations*. Current Opinion in Solid State and Materials Science, 2014. **18**(4): p. 188-195.

212. Balk, T.J. and Hemker, K.J., *High resolution transmission electron microscopy of dislocation core dissociations in gold and iridium.* Philosophical Magazine A: Physics of Condensed Matter, Structure, Defects and Mechanical Properties, 2001. **81**(6): p. 1507-1531.

213. Ge, C.Z., Wang, H.W., and Ming, N.B., *Birefringence images of screw dislocations viewed end on in cubic crystals containing a long-range stress field*. Journal of Applied Physics, 1993. **74**(1): p. 139-145.

214. Eshelby, J.D., et al., *CXL. Dislocations in thin plates.* Philosophical Magazine, 1951. **42**(335): p. 1401-1405.

215. Mendis, B.G. and Hemker, K.J., *Bloch wave analysis of the Eshelby twist contrast around end-on screw dislocations in bcc Mo.* Ultramicroscopy, 2008. **108**(9): p. 855-864.

216. Wu, W. and Schaeublin, R., *TEM diffraction contrast images simulation of dislocations.* Journal of Microscopy, 2019. **275**(1): p. 11-23.

217. Sass, S. and Balluffi, R., *On the analysis of electron diffraction patterns from twist grain boundaries*. Philosophical Magazine, 1976. **33**(4): p. 703-707.

218. Marcinkowski, M., Tseng W., and Dwarakadasa, E., *Relationship between grain boundary dislocations, Moiré patterns, and diffraction effects.* Physica Status Solidi (a), 1974. **22**(2): p. 659-669.

219. Song, C., et al., *Insight into long-period pattern by depth sectioning using aberration-corrected scanning transmission electron microscope*. Ultramicroscopy, 2020. **209**: p. 112885.

220. Guan, D.Y. and Sass, S.L., *Diffraction from periodic arrays of dislocations.* The Philosophical Magazine: A Journal of Theoretical Experimental and Applied Physics, 1973. **27**(5): p. 1211-1223.

221. Reed-Hill, R.E. and Robertson, W, *Deformation of magnesium single crystals by nonbasal slip*. JOM, 1957. **9**(4): p. 496-502.

222. Chapuis, A. and Driver, J.H., *Temperature dependency of slip and twinning in plane strain compressed magnesium single crystals.* Acta Materialia, 2011. **59**(5): p. 1986-1994.

223. Li, H., et al., *Experimental investigation on temperature-dependent uniaxial ratchetting of AZ31B magnesium alloy*. International Journal of Fatigue, 2019. **120**: p. 33-45.

224. Gu, P., Kad, B.K., and Dao, M., *A modified model for deformation via partial dislocations and stacking faults at the nanoscale.* Scripta Materialia, 2010. **62**(6): p. 361-364.

225. Van Swygenhoven, Spaczer, H., M., and Caro, A., *Microscopic description of plasticity in computer generated metallic nanophase samples: a comparison between Cu and Ni.* Acta Materialia, 1999. **47**(10): p. 3117-3126.

226. Kumar, K.S., et al., *Deformation of electrodeposited nanocrystalline nickel*. Acta Materialia, 2003. **51**(2): p. 387-405.

227. Schiøtz, J., Di Tolla, F.D. and. Jacobsen, K.W, *Softening of nanocrystalline metals at very small grain sizes.* Nature, 1998. **391**(6667): p. 561-563.

228. Hirata, A., et al., *Direct observation of local atomic order in a metallic glass.* Nature Materials, 2011. **10**(1): p. 28-33.

229. Liu, F.C. and Ma, Z.Y., *Contribution of grain boundary sliding in low-temperature superplasticity of ultrafine-grained aluminum alloys.* Scripta Materialia, 2010. **62**(3): p. 125-128.

Contributions Arising from This Thesis

1. Liu, Y.S., and Zhu G.Z., *Real-time Imaging Slip Planes in Many Grains during In-situ Nanoindentation*. (Nature Communication, under review);

2. *Real-time Orientation Monitoring Using Hollow-cone Dark Field imaging*. (Under preparation)

3. Liu, Y.S. and Zhu G.Z., *Hollow-cone Dark Field (HCDF) Imaging for Nano-grained Mg: Experimental and Simulated Contrast*. Microscopy and Microanalysis, 2022. **28**(S1): p. 340-343. doi: 10.1017/S1431927622002124.

4. Liu, Y.S., Yan, J.W., Xie, D.Y., Shen. Y., Wang, J. and Zhu, G.Z., *Self-patterning screw <c> dislocations in pure Mg*. Scripta Materialia, 2021. **191**: p. 86-89. doi: 10.1016/j.scriptamat.2020.09.014.

5. Liu, Y.S., Lin, M.H. and Zhu, G.Z., *Self-assembly of Periodical< C>-screw Dislocation Array in Hot-compressed Pure Magnesium*. Microscopy and Microanalysis, 2020. **26**(S2): p. 2044-2045. doi: 10.1017/S1431927620020255.

Publications

1. Tan, X.N., Qiu, R.S., Liu, Y.S., Bi, F.X., Zhang, J. L., Tao, B.R. and Liu, Q., *Nanoscale face-centered-cubic zirconium dispersed in omega zirconium*. Philosophical Magazine Letters, 2022. **102**(7): p. 220-228. doi: 10.1080/09500839.2022.2077999. (*co-corresponding author*)

2. Zhou, P., Liu, Y.S., and Zhu, G.Z., *Sawtooth Faceting in Rutile Nanowires*. ACS Omega, 2022. **7**(12): p. 10406-10412. doi: 10.1021/acsomega.1c07119. (*co-first author*)

3. Tao, B.R., Qiu, R.S., Liu, Y.S., Tan. X.N. and Liu, Q., *FCC phase transformation of Zr alloy during air cooling and aging*. Journal of Nuclear Materials, 2021. **551**: p. 152989. doi: 10.1016/j.jnucmat.2021.152989.

4. Liu, Y.S., Yan, J.W., Xie, D.Y., Shen. Y., Wang, J. and Zhu, G.Z., *Self-patterning screw <c> dislocations in pure Mg*. Scripta Materialia, 2021. **191**: p. 86-89. doi: 10.1016/j.scriptamat.2020.09.014.

5. Lin, M.H., Liu, Y.S., and Zhu, G.Z., *Mn-Promoted Growth of Mg-Based Spinel and Pyroxene Nanostructures*. ACS Omega, 2020. **5**(3): p. 1566-1571. doi: 10.1021/acsomega.9b03519.

6. Liu, Y.S., Qiu, R.S., Tan, X.N., Tao, B.R. and Zhao, Y.F., *A new hexagonal Zr-(Fe, Cu) precipitate in Zr-1.0 Sn-0.3 Nb-0.3 Fe-0.1 Cu alloy*. Journal of Nuclear Materials, 2019. **527**: p. 151792. doi: 10.1016/j.jnucmat.2019.151792.

7. Tao, B.R., Luan, B.F., Qiu, R.S., Fang, Q., Cao, L.F., Liu, Y.S., Zhang, X. Y., Liu, R. P. and Liu, Q., *Analysis of atomic distribution near grain boundary in Zr-Sn-Nb-Fe-(Cu) alloys by atom probe tomography*. Journal of Nuclear Materials, 2019. **515**: p. 135-139. doi: 10.1016/j.jnucmat.2018.12.033.

Conference Proceedings

1. Liu, Y.S. and Zhu G.Z., *Hollow-cone Dark Field (HCDF) Imaging for Nano-grained Mg: Experimental and Simulated Contrast*. Microscopy and Microanalysis, 2022. **28**(S1): p. 340-343. doi: 10.1017/S1431927622002124.

2. Liu, Y.S., Lin, M.H. and Zhu, G.Z., *Self-assembly of Periodical <C>-screw Dislocation Array in Hot-compressed Pure Magnesium*. Microscopy and Microanalysis, 2020. **26**(S2): p. 2044-2045. doi: 10.1017/S1431927620020255.

3. Zhu, G.Z., Lin, M.H. and Liu, Y.S., *Kinetically Favorable Growth of Oxides Nanowires and Pyramids with Gold Seeds*. Microscopy and Microanalysis, 2020. **26**(S2): p. 1430-1431.doi: 10.1017/S1431927620018085.

4. Lin, M.H, Liu, Y.S. and Zhu, G.Z., *Irrational Orientations and Atomistics at Gold-Rutile Interfaces*. 2020. Microscopy and Microanalysis, **26**(S2): p. 290-291. doi: 10.1017/S1431927620014087.

5. Lin, M.H., Liu, Y.S. and Zhu, G.Z, *Coexistence of Tetragonal Spinel Nanowires and Cubic Spinel Nanopillars during Gold-assisted Growth*. Microscopy and Microanalysis, 2019. **25**(S2): p. 1986-1987. doi: 10.1017/S1431927619010663.